A STUDY OF AVALANCHE SIGNAL INFORMATION CONTENT IN FMRI AND A PROBABILISTIC MODEL OF ITS CHANGES

By

Nazirah Mohd Khairi

Dissertation

Submitted to the Faculty of the

Graduate School of Vanderbilt University

in partial fulfillment of the requirements

for the degree of

DOCTOR OF PHILOSOPHY

in

Electrical Engineering

May 12, 2023

Nashville, Tennessee

Approved:

D. Mitchell Wilkes, Ph.D.

Zhaohua Ding, Ph.D.

Alan Peters, Ph.D.

Catherine Chang, Ph.D.

Baxter Rogers, Ph.D.

To my lovely Abang,

Aufa, Adam,

Mak & Ayah,

Ummi & Ayah,

and siblings.

ACKNOWLEDGMENTS

Throughout my studies, I have had a great, thoughtful adviser, Dr. Mitch Wilkes, since my undergraduate career. This work would not have been possible without his guidance and support to go through this long journey of a learning experience. His patience, care, and chillness have helped me tremendously to maintain my motivation mentally and emotionally. My sincere thanks to Drs. Zhaohua Ding and Catie Chang, who have been assisting me with valuable feedback and ideas, especially in their expertise in human brain imaging. I would like to also thank my other committee members, Drs. Alan Peters and Baxter Rogers for their continuous support, insights, and suggestions.

Not to forget my colleagues, Junlin Gao and Lyuan Xu, and former colleagues, Dr. Charreau Bell, Shengchao, and Yuchen, who have been sharing input and thoughts on my work in our research group.

My teaching and research experiences have also broadened from being part of the ECE department, Center for Teaching (CfT), the Institute of Software and Integrated Systems (ISIS), and Medical-image Analysis and Statistical Interpretation (MASI) labs here. Thank you for giving me the opportunities; these are all priceless experiences I might not get anywhere else.

My beloved husband, Ahmad Saifuddin, who has been extremely patient with his wife during this long journey and has been a wonderful super dad - I can't thank you enough for supporting me since the beginning of the Ph.D. application, up until now, we have gone through ups and downs in our marriage and my study. My dearest Aufa and Adam are the best children I could ever ask for. Sincere appreciation for my parents and parents-in-law; their love and care are my motivation for not giving up. I believe their prayers never stopped since I started, and here you go, Mak and Ayah, this is for you. My siblings and in-laws, too, thank you for never stopping cheering me up in messages while being all over the world. Special thanks to my youngest sister, Syahidah, for joining my daily ramblings of coding errors and random ideas. Keep on going to finish your Ph.D. too!

Lastly, I put my deepest gratitude to Allah for allowing me to go through this journey. Without His will, I will never have come to this point. Indeed, He never lets me down whenever I am at the lowest point, and He constantly reminds me to keep going when I feel there is nowhere to go through this path.

This is a piece of knowledge that I would like to present with the hope of benefiting a better world.
This is not the end,
this is the beginning of more adventures to come!

TABLE OF CONTENTS

Page

DEDICATION . . . . . **iii**

ACKNOWLEDGMENTS . . . . . **iv**

LIST OF TABLES . . . . . **viii**

LIST OF FIGURES . . . . . **ix**

1 Introduction **1**

2 Background **3**

2.1 Structure of a Human Brain and Brain Network Connectivity 3
2.1.1 Structure of a Human Brain 3
2.1.2 Resting-state Networks (RSNs) in the Resting-state fMRI (rsfMRI) 5
2.2 fMRI and Functional Connectivity (FC) 6
2.2.1 MRI Acquisition 6
2.2.2 Image Formation 8
2.2.3 Functional Connectivity in fMRI 10
2.3 Principal Component Analysis (PCA) and Independent Component Analysis (ICA) 12
2.3.1 PCA 12
2.3.2 ICA 14
2.3.3 Sliding-window Configuration in fMRI Analysis 15

3 Modified Principal Component Analysis in sliding windowed fMRI data **18**

3.1 Introduction 18
3.2 Modified PCA Algorithm 20
3.2.1 The Proposed Method 21
3.2.2 Maximization of Subsequent Components Fractions 22
3.3 fMRI Analysis Methodology 23
3.3.1 fMRI Data 23
3.3.2 Instantaneous Whole Brain Correlation (IWBC) Patterns 23
3.4 Results and Discussion 23
3.4.1 Maximum Number of Components 23
3.4.2 Size of N_{hop} and N_{win} 24
3.4.3 Orthogonality of Components 25
3.4.4 Connectivity Pattern Analysis: An Application 26
3.4.4.1 Connection Between Whole Brain Avalanche and the Windowed Coefficients 26
3.4.4.2 Window Centered on Avalanche 27
3.5 Conclusions and Future Directions 28

4 Visualization of spatio-temporal dynamics of brain activity avalanches in fMRI signals **30**

4.1 Introduction 30

4.2 Methodology . . . 33
4.2.1 Extended Modified PCA for Sliding-Windows (mPCASW) . . . 33
4.2.2 Measuring Performance of Sliding-window Algorithm . . . 37
4.2.3 fMRI Data . . . 37
4.2.3.1 Resting-state fMRI . . . 37
4.2.3.2 Sleep fMRI . . . 38
4.2.4 Preprocessing . . . 38
4.2.5 Coefficient Values and Instantaneous Whole Brain Correlation (IWBC) . . . 38
4.2.6 fMRI Analysis . . . 39
4.3 Results and Discussions . . . 40
4.3.1 Basis Vectors of the Extended mPCASW . . . 40
4.3.2 Effect of Different Window Settings . . . 40
4.3.3 Changes in rsfMRI Signal Content Detected With mPCASW . . . 42
4.3.4 Functional Content Changes in Insula Regions . . . 47
4.4 Conclusion . . . 47

5 Dynamic Temporal Propagation Patterns in Avalanches of fMRI . . . 49

5.1 Introduction . . . 49
5.2 Methodology . . . 51
5.2.1 fMRI Data . . . 51
5.2.2 mPCASW Components and Instantaneous Whole Brain Correlation (IWBC) . . . 51
5.2.3 mPCASW Component Classifications . . . 52
5.2.4 Timing Pattern Sequence . . . 54
5.2.5 Clustering of Sequential Timing Patterns . . . 55
5.2.6 Other Patterns Analysis . . . 55
5.3 Results and Discussions . . . 56
5.3.1 Temporal Ordering Across Functional Networks (FCN) in EC Component Pattern . 56
5.3.2 Clusters of Different Timing Patterns . . . 56
5.3.3 What About Other Patterns? . . . 59
5.3.3.1 Converging (CV) and Diverging (DV) Coefficient Patterns . . . 59
5.3.3.2 DC and CD Coefficient Patterns . . . 59
5.3.4 What Do These Signal Content Changes Mean? . . . 62
5.4 Conclusion . . . 65

6 Summary and Future Works . . . 66

Appendices . . . 70

A Maximum Number of Components in the Extended mPCASW . . . 70

B Clusters of Components in the Extended mPCASW . . . 72

C Impact of different covariance matrices definition in fMRI data . . . 75

C.1 Analysis . . . 75
C.1.1 Covariance Matrix Based on Standard PCA Definition . . . 76
C.1.2 Covariance Matrix Based on WSS Definition . . . 76
C.1.3 mPCASW Application on fMRI Data . . . 76
C.2 Results . . . 77
C.3 Summary . . . 80

References **81**

LIST OF TABLES

Table		Page
3.1	Average windowed Dot products of a subject with different N_{win} and $N_{hop} = 4$	25
3.2	Average windowed Dot products of a subject with different N_{win} and $N_{hop} = 4$ using classical PCA on windowed data	26
3.3	Dot products of a subject with $N_{win} = 20$ and $N_{hop} = 4$ using classical PCA and fastICA on windowed data	27
3.4	Average Standard deviation of the components' values for $N_{win} = 20$ and $N_{hop} = 4$ using Modified and Classical PCA methods on 60 IWBC peaks	28
3.5	Average Standard deviation of the components' values for $N_{win} = 20$ and $N_{hop} = 4$ using Modified and Classical PCA methods on 800 time points	29
3.6	Average Standard deviation of the components' values for $N_{win} = 20$ and $N_{hop} = 4$ using Modified and Classical PCA methods on 1000 time points	29

LIST OF FIGURES

Figure Page

2.1 Human brain anatomy and the brain parcellation in various lobes (Blausen Medical, 2014; Staff, 2014). Both images were obtained under Creative Commons license (CC BY-SA 4.0). 3

2.2 Human brain tissues can be categorized as the gray matter and white matter as depicted in gray and almost-white colors respectively. The cerebrospinal fluid (CSF) is the dark area that circles around the brain between the brain tissues and the skull. This T_1 image was obtained from an MRI from dataset in (Glasser et al., 2013). 4

2.3 The Consensual Atlas of REsting-state Networks (CAREN), a resting-state network atlas computed based on four different atlases described in (Doucet et al., 2019). Five major networks are identified as the sensorimotor-auditory network (SMN-AUD), salience network (SAL), central executive network (CEN), default mode network (DMN) and visual network (VIS). This image is obtained from the article under Creative Commons license (CC BY-NC-ND 4.0). 5

2.4 A 1.5T MRI scanner (Park et al., 2014). The images acquired are under creative common license. 7

2.5 Comparison between T_2 (left) and T_1 (right) images obtained from an MRI from dataset in (Glasser et al., 2013). The main difference in these two images can be seen in the color intensities between the gray and white matters. 8

2.6 An example of a T_2^*-weighted (or BOLD contrast) image obtained from an MRI from dataset in (Glasser et al., 2013) 9

2.7 A hemodynamic response function model (Scheef and Boecker, 2012). 10

2.8 An fMRI image configuration with BOLD signal at voxel location $[30, 45, 45]$ for 150 time points. This fMRI BOLD image was obtained from an MRI from dataset in (Glasser et al., 2013). 11

2.9 Main approaches in fMRI FC analysis. 12

2.10 An illustration of cocktail party problem 13

2.11 One of the sliding-window approaches is where the windows are applied on the fMRI scans before each window is decomposed using PCA or ICA separately as described in (Kiviniemi et al., 2011). 16

2.12 GIFT data arrangement for its group ICA (Sakoglu et al., 2010). The data is stacked temporally producing the spatial components. The sliding-window approach is applied onto its resulting ICA components (matrix A). 16

3.1 Maximum number of components for different N_{hop} and N_{win}. 24

3.2 Average dot products for different N_{hop} and N_{win} across 16 subjects. 25

3.3 Standard Deviation Volume for a single subject. Calculations were based on $N_{win} = 20$ and $N_{hop} = 4$. Two sets of peak transitions were shown in the red boxes. As the highest peaks joined in the window, the standard deviation volume starts to drop and begin to increase again after the peak has reached the center of a window. 28

4.1 The IWBC and global means plots of a single subject. The IWBC is scaled to 10^2 to show the patterns and peaks clearly. 39

4.2 The dot products of all the basis vectors decomposed from a single subject derived from the (a) mPCASW approach, (b) ICA approach, and (c) ICA approach on sliding-windowed data. For results that use sliding-window data ((a) and (c)), the windows are set to have $N_{win} = 20$ and $N_{hop} = 4$. (a) Using mPCASW, the orthogonality maintains within a subspace with tiny dot products (bottom left) but can go up to 10^{-2} when the basis vectors are from different subspaces (bottom right). (b) When fastICA was applied to the data without windowing, the maximum dot products are closer to mPCASW with up to 10^{-1}. However, in a small subspace of the ICA, mPCASW shows higher orthogonalities between the basis vectors. (c) As sliding window setting was applied to the fastICA components, the overall dot product range stays close to the regular data setting (without windowing) with slightly lower values. Similar to (b), the subspace's dot products show higher values than the mPCASW method in the first subspace. 41
4.3 Dot product variations using different window length and number of overlapping timepoints. 41
4.4 Changes in the signal content on the global means of a set of data. We can see more compact changes separated in various components using mPCASW whereas spectrogram and the wavelet transform show distributed changes based on the frequency and time-scale that cannot be seen in a specific timepoint. 42
4.5 Statistics results for an HCP resting-state fMRI subject. Following the IWBC avalanches (blue), the SDV (red) dropped after most of high peaks of the avalanches occurred. 43
4.6 Average SDVs across 9 windows in 159 peaks occurred in 53 subjects' IWBC. On average, the lowest point appears at windows 3 and 4, where the peaks started to enter the windows. The SDV increased and dropped back after the peaks left the windows. 43
4.7 Changes in the signal content in the whole brain across the time windows around the tallest peak of the IWBC of a single subject using (a) extended mPCASW and (b) ICA. Window 193 is the window where the highest point of the avalanche (timepoint 777 at 559.44 seconds of IWBC in Figure 4.1) occurs in the middle of the time window. 44
4.8 Changes in the signal content in the whole brain across the time windows that do not have high peaks (around timepoint 256 at 184.32 seconds) in the IWBC of a single subject using extended mPCASW. In these windows, no peaks or neighboring avalanches were happening. 45
4.9 Clusters in each component across 9 windows in a single subject at (A) the highest IWBC peak (timepoint 777 at 559.44 seconds) and (B) a timepoint with no peak (timepoint 256 at 184.32 seconds). Results for all clusters in both timepoints can be retrieved in Appendix B. **(A)** At the highest IWBC peak (timepoint 777), cluster 12 and 11 show the highest coefficient centers, particularly in component 6 and 16. Clusters 1 and 10 show low-coefficient component centers, particularly in component 6 and 16. **(B)** For timepoint 256, where there is no huge IWBC avalanche, there are clusters that show significant changes in component coefficient centers, especially in components 1 in both high and low coefficient clusters. 46
4.10 The transform coefficients of a sleep fMRI from component 1 at the highest peak of its IWBC. 47
4.11 Total sleep transform coefficients, β in insula region voxels from component 1,2, and 3 for sleep fMRI that have slept after (a) 10 minutes, (b) 15 minutes, and (c) not sleeping at all during the scanning session. 48

5.1 The IWBC plot of a single subject. 52
5.2 20 component coefficients extracted using modified Principal Component Analysis for Sliding Window (mPCASW) for 9 windows across an IWBC peak in the 7-network regions from Yeo's atlas (Yeo et al., 2011). Five different major patterns can be categorized: (1) extremal curve (EC), (2) diverging (DV), (3) converging (CV), (4) diverging-converging (DC), and (5) converging-diverging (CD) patterns. In this β set, we can classify components 1, 6, 11, and 16 as EC; 2, 3, 7, 12, 13, 17, and 19 as DV; 5 as CV; 10, 14 and 15 as DC; and 20 as CD. 53
5.3 An example of a 9-window set around an IWBC peak. Windows 3-7 contain the tip of the IWBC peak, with the tip at the center of window 5. 54

5.4 Examples of components coefficients that are excluded from the analysis are the components that (a) do not have any distinct pattern, i.e, minimal changes in the coefficient values, (b) have more than one local minimum or maximum, and (c) have multiple CD or DC patterns, within the 9-window range around its IWBC peak. 55
5.5 The region timing sequence in EC peaks. (top) In all three cases (positive, negative, and combined EC components), the curves for all regions generally follow the IWBC avalanches curves. Several distinguished regions can be seen to have a clear sequence, such as the dorsal attention network (DAN), which shows a high probability of having an EC component peak at the same window as the IWBC peaks. (bottom) In a regional sequence manner, 60% of the EC components show that SMN and SVN reach their peak early compared to other regions, while the limbic network tends to reach its peak later 30% of the time. 57
5.6 The timing sequence of each FCN based on the EC components. The somatomotor network typically strikes up first compared to other networks. The high β flows from the top of the brain to the visual network region and ends at the frontal lobe, where the dorsal attention and limbic networks are. 57
5.7 The Extremal curves (EC) components clustered into six clusters according to the distance pattern from the central window 5 for (a) positive EC, (b) negative EC, and (c) combined positive and negative EC components. In all cases, the largest clusters appear to be the components that have EC peaks close to where the IWBC peaks are at the center, i.e., zero distance from window 5 (light green and light blue shades). The next large clusters are the groups of components where all regions reach the highest point a few windows earlier or later than the IWBC peak (dark blue and bright yellow shades). In a small number of cases, a small set of components show a distinct separation between the regions. For example, Visual, DAN, and SVN networks of the second cluster in (c) tend to reach the EC peaks later than the other four networks. 58
5.8 The changes of β standard deviation in diverging (DV) and converging (CV) components across 9 windows around large IWBC peaks. The first plot of each pattern shows the individual component's percent change from the previous window, while the second and third plot the mean and median of the components' change with the error bars of the standard error (SE) and interquartile range (IQR), respectively. Some components show huge changes in several windows to more than 100%. However, the mean and median present the overall distribution across 738 and 648 DV and CV components, respectively. 60
5.9 The changes (in percentage) of the average β in each network region categorized as (a and c) diverging (DV) and (b and d) converging (CV) component patterns. In (a) and (c), SMN and DAN networks show the most noticeable change in DV as the IWBC peaks leave the sliding windows, while other networks show smaller changes earlier. In (b) and (d), the limbic network shows the largest change as the IWBC peaks leave the sliding windows. The other networks converge earlier, with some networks, including DAN, having two major timing changes in the CV components. 61
5.10 The changes (in percentage) of the average β in each network region are categorized as (a and c) DC and (b and d) CD component patterns. In (a) and (c), most DC components have large changes as they diverge, but smaller changes happened during the convergence at the end of the 9-window set. The divergence is likely to happen before the IWBC peaks reach the center of the window, i.e., at window 5. In (b) and (d), the CD components are more spread out, with DAN making the most significant change while transitioning from windows 4 to 5. While diverging back after the IWBC peaks leave the windows, the control network dominates the changes among all other networks. 63
5.11 Sequence summary of each converging and diverging pattern in percent changes order from large to small. Dorsal attention (DAN) and somatomotor (SMN) networks present large changes in all patterns in the β values around the large IWBC peaks. Interestingly, the Default Mode Network (DMN) does not show large changes in resting-state networks fMRI through our mPCASW β values. 64

5.12 Histogram counts for each pattern with the number of components included in the count for each pattern stated in the parentheses. The EC patterns are dominated by components 1, 6, 11, and 16. There is no clear relationship between the component number with the other β patterns; however, the CD pattern appears less than other patterns as the maximum count of components in CD is less than 40. 64

B.1 Clusters in each component across 9 windows in a single subject. The highest IWBC timepoint (timepoint 777 at 559.44 seconds) in Figure 1 is in the middle of fifth window, and therefore this timepoint is sledded in window 3-7. As mentioned in Section 4.3.3, clusters 12 and 11 showed the components with highest coefficients, while clusters 1 and 10 contains the components with lowest coefficients. 73

B.2 Clusters in each component across 9 windows in a single subject. The timepoint 256 at 184.32 seconds in Figure 1 is in the middle of fifth window, and therefore this timepoint is sledded in window 3-7. As mentioned in Section 4.3.3, clusters 6 and 17 showed the components with highest coefficients, while clusters 20 and 11 contains the components with lowest coefficients. 74

C.1 The dot products of the mPCASW basis vectors from a single subject with the window setting of $N_{win} = 20$ and $N_{hop} = 4$. The covariance matrices were calculated (a) with removing global means and (b) with global means before mPCASW algorithm is applied. In both cases, the dot products remain low especially in the first subspace (middle squares). It is notable that the removing global means in the covariance produce higher dot products as it could reach 10^{-1}, but it remains at the lower values. 78

C.2 The average dot products in a subject to represent the orthogonality of the mPCASW basis vectors across different N_{win} and N_{hop} with removing global means (solid lines) and with global means (dotted lines) in the covariance matrix before mPCASW algorithm is applied. There are huge variances in the dot products around smaller N_{win} across different N_{hop} especially when the window size reaches 8 and 10 timepoints. As the window size N_{win} becomes larger, the size of both N_{win} and N_{hop} do not affect much on the dot products, and thus, the mPCASW basis vectors reaches close to orthogonality as the average dot products converges to zero. 79

C.3 β of a subject calculated (a) with removing global means and (b) with global means in the covariance matrix before the mPCASW algorithm is applied. The observed pattern of β from the whole brain remain similar as the are groups of voxels that become deactivated or activated during the IWBC avalanches in each component. 79

CHAPTER 1

Introduction

Before 1990, medical imaging studies focused on studying brain structures and applications to detect physical brain impairments, as well as learning its regions' functionalities using other brain measurements such as electroencephalography (EEG), which evaluates electrical activity in the brain from EEG electrodes placed on the scalp. Since the early 1900s, brain scans have used multiple modalities, including x-ray, computed tomography (CT), and magnetic resonance imaging (MRI) (Bercovich and Javitt, 2018). Later in the 1990s, functional magnetic resonance imaging (fMRI) was developed that detects the oxygen level in the blood vessels inside the brain. It has since become a valuable instrument for learning the dynamics of brain activations.

As fMRI technology advanced, more studies in various fields using this type of imaging, including neuroscience and signal processing methodologies, to ensure the accuracy of the interpretations. Brain region extractions have been found based on functional activation during the scan. Researchers also discovered the brain network from the scans. Resting-state scans also revealed that there are resting-state networks (RSNs), which are usually active when the subject is not assigned any task and only lying down inside the MRI scanner. These findings have helped in many disease detection and diagnoses such as epilepsy and schizophrenia (Sakoglu et al., 2010; Vergun et al., 2016) and other mental disorders based on the difference in the functional network activations between ill patients and healthy control subjects.

With the continuous findings using the fMRI data, many researchers began to develop better tools to improve the current findings and extract more valuable information from this vast collection of signals from the brain. Data-driven algorithms such as general linear modeling (GLM), seed-based correlation analyses, principal component analysis (PCA), independent component analysis (ICA), and graph theory have been used extensively in the fMRI studies to investigate the connectivity across the different brain regions and its functionalities (Zhan and Yu, 2015).

On the contrary, the issue of a gigabyte (GB) database brought another line of exploration in fMRI research. An original 5-minute fMRI dataset from a single subject can cost multiple GBs of storage capacity (Glasser et al., 2013), not including the intermediate processing. This issue has also led to the development of various compression methods and more optimized analysis methods that can lower the processing time but still maintain excellent performance in terms of resulting outcomes for further analyses. For example, a traditional PCA is regularly used to remove noisy components of a dataset, thus smaller size and 'cleaner' data is processed into the main processing algorithm (Sakoglu et al., 2010; Allen et al., 2014; Kiviniemi et al., 2011; Kucyi and Davis, 2014). Another approach, called the sliding-window, was introduced to allow

the data division into smaller time windows to observe the flow of the activities and the behavior of a human brain more dynamically. (Andersen et al., 1999; Karvanen and Theis, 2004; Allen et al., 2014) have used the sliding-window approach in different configurations with significant results showing the benefit of using this approach.

As developing novel tools in the signal processing field, particularly in neuroimaging studies, has become one focus, this work provides several proposals to analyze the fMRI data in novel ways. This manuscript is organized into several chapters surrounding the introduced method and the applications of these methods. Chapter 2 provides essential background on brain structures and the fMRI that are to be used in this study. Several signal processing methods, including the Principal Component Analysis (PCA) and Independent Component Analysis (ICA), are described briefly to understand their similarities and differences. We also explained the sliding-window approaches in datasets and examples of how they are applied in various signal types studies. In chapter 3, we describe an algorithm called the modified PCA for Sliding-Window (mPCASW) designed to extract the basis vectors and components from a set of data based on the sliding-window approach. Basic results on the characteristics of the resulting basis vectors are described as well as a small application in the fMRI context. Chapter 4 extends the mPCASW algorithm to extract extra components and dives into the fMRI signal content from the mPCASW results when applied to the fMRI data from different subjects in multiple unique visualizations. We explore patterns observed in the basis vectors around the brain avalanches, where large parts of the brain are active. We could further extract more information if we look at the results from the different approaches described in this chapter.

In chapter 5, we focus on the timing propagation patterns in the fMRI signal coefficients obtained from the mPCASW components described in the previous chapters. Five types of patterns are introduced to observed behaviors of the signal propagation in fMRI data and understand these behaviors in neurological interpretations. Lastly, a short chapter 6 compares two covariance matrices that use different definitions to calculate the mean of a dataset. We describe the assumptions made in both methods and compare the effect in the mPCASW basis vector components. This manuscript ends with a summary of the key results described in this work. We also provide suggestions for future works that can benefit future research in signal processing and fMRI studies.

CHAPTER 2

Background

2.1 Structure of a Human Brain and Brain Network Connectivity

The human brain is one of the most complex objects in the universe that researchers are still exploring. A theoretical physicist Michio Kaku said, 'The human brain has 100 billion neurons, each neuron connected to 10,000 other neurons. Sitting on your shoulders is the most complicated object in the known universe.' (Kaku, 2014). Imagine how humans have invented computing devices in the past decades, but the complexity of current computers and smartphones is still incomparable to their own brain computing capability. In order to explore brain functionality, it requires the knowledge of its structure and neurological definitions between the brain regions.

2.1.1 Structure of a Human Brain

Structurally, the human brain consists of three main parts - cerebrum, cerebellum, and the brainstem (Figure 2.1). The cerebrum is the largest area in the human brain and plays a vital role in daily human activities related to motor skills and memory functioning. It consists of left and right cerebral hemispheres, basal ganglia and diencephalon. The brain stem and cerebellum mainly function to control internal human body functions, such as muscle activity, consciousness, respiration, and cardiac processes (Murphy et al., 2016).

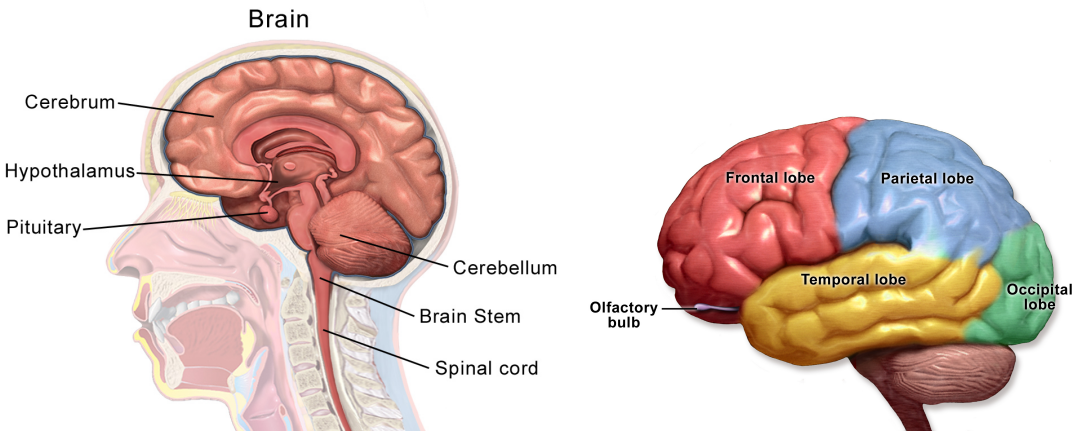

Figure 2.1: Human brain anatomy and the brain parcellation in various lobes (Blausen Medical, 2014; Staff, 2014). Both images were obtained under Creative Commons license (CC BY-SA 4.0).

On the brain tissue perspective, a human brain consists of gray matter, white matter, and cerebrospinal fluid (CSF) (Figure 2.2). The gray and white matter are the main substances in the two cerebral hemispheres

where white matter lies underneath the gray matter, and they work together to perform higher-order functions such as memory, cognition, and motor control (Murphy et al., 2016). The CSF, a clear and colorless fluid produced inside the ventricles of the brain, covers the entire brain to provide protection to the brain inside the skull (Holtz, 2010).

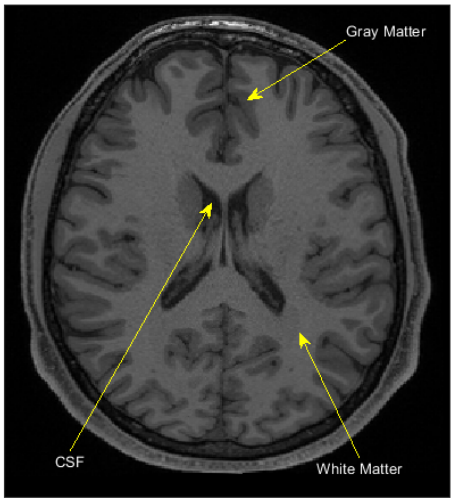

Figure 2.2: Human brain tissues can be categorized as the gray matter and white matter as depicted in gray and almost-white colors respectively. The cerebrospinal fluid (CSF) is the dark area that circles around the brain between the brain tissues and the skull. This T_1 image was obtained from an MRI from dataset in (Glasser et al., 2013).

The cerebrum or mainly the two cerebral hemispheres can be divided into distinct fissures of lobes, namely the frontal, occipital, parietal, and temporal lobes, as shown in Figure 2.1. These lobes do not function by themselves and heavily rely on each other to perform specific tasks. The frontal lobe focuses more on making judgments, modulates the emotions and personality traits, and transforms thoughts into words. The parietal lobe then makes the interpretations of the sensory perception and understanding of language and words received. It also associates the audio and visual inputs with memory to provide meanings to them. Visual processing is mostly done in the occipital lobe, while the temporal lobe handles the memory and hearing systems. Another two areas that usually raise the researchers' attention are Wernicke's area and Broca's area located in the posterior of the left temporal lobe and frontal lobe, respectively. Wernicke's area is involved in understanding the spoken and written words while Broca's area functions as understanding the language syntaxes and speech formation (Dubuc, 2012).

While structural regions of the brain can be observed using x-ray, CT scan, and magnetic resonance imaging (MRI), we can observe the brain activities using functional MRI (fMRI), which will be described

further in Section 2.2. From this information, many studies have created or defined the brain networks categorized by their functions. Each functional network is associated with specific physical regions of the brain. Here, a group of brain networks called resting-state networks (RSNs) is discussed further for this particular study.

2.1.2 Resting-state Networks (RSNs) in the Resting-state fMRI (rsfMRI)

A resting-state of a brain is defined as a brain state where the brain is not assigned to any particular task. In early studies of brain activity, medical studies focused only on learning brain activities when a human is assigned to a specific task during the brain scan such as reading, watching an image, or listening tasks (Niazy et al., 2011). Years after, researchers have found interesting findings that a human brain can be very active even when the human is not doing anything specific activity. One example of an RSN atlas was computed based on multiple previous atlases called the Consensual Atlas of REsting-state Networks (CAREN) (Doucet et al., 2019) shown in Figure 2.3. The four atlases (Yeo et al., 2011; Gordon et al., 2016; Doucet et al., 2011, 2018) have different numbers of identified networks. However, most of them agree that the five major functional networks throughout the whole brain related to the resting-state configuration are the default mode network, central executive network, salience network, visual network, and sensorimotor network.

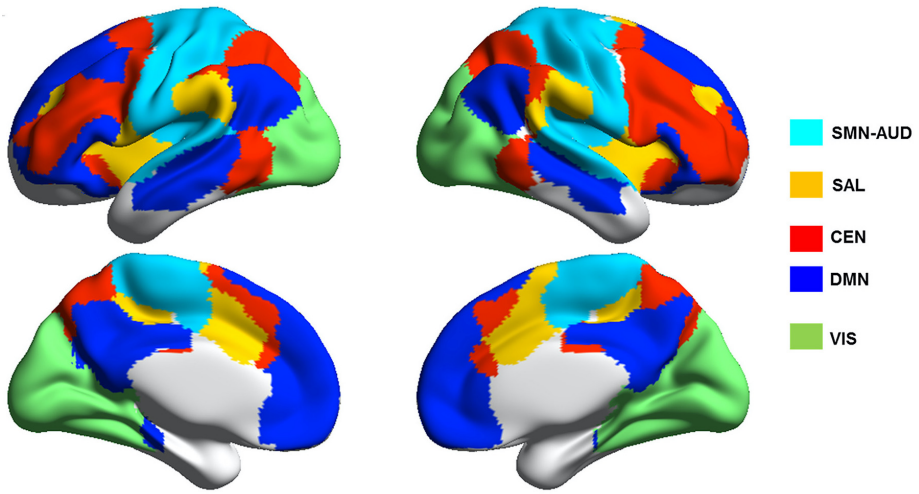

Figure 2.3: The Consensual Atlas of REsting-state Networks (CAREN), a resting-state network atlas computed based on four different atlases described in (Doucet et al., 2019). Five major networks are identified as the sensorimotor-auditory network (SMN-AUD), salience network (SAL), central executive network (CEN), default mode network (DMN) and visual network (VIS). This image is obtained from the article under Creative Commons license (CC BY-NC-ND 4.0).

One of the most important RSNs that is worth describing here is the Default Mode Network (DMN). To date, the exact functional role of this network is not conclusive, but the brain regions classified in the DMN have shown to be active throughout the scans of a brain. In (Greicius et al., 2003), they reported that

several regions, including the posterior cingulate cortex (PCC) and ventral anterior cingulate cortex (vACC), have demonstrated being undisrupted during visual processing and maintained active during resting state. This finding has provided evidence of the existence of the DMN in the human brain. (Buckner et al., 2008) explored two possibilities of the DMN functions; (1) the DMN is possibly supporting the dynamic mental processing concerning the past and present experiences which connect the DMN to the memory and sensory systems mostly, and (2) the DMN could function to monitor the exploration of the external environment when focused attention is not in use.

The central executive network, which connects the dorsolateral prefrontal cortex and the posterior parietal cortex, functions to support the behavior, emotion and cognitive thought regulation (Heine et al., 2012). The salience network has connections to subcortical and limbic structures, and it is linked to the internal attention states, conflict monitoring and pain-related processing.

2.2 fMRI and Functional Connectivity (FC)

Originating from noninvasive Magnetic Resonance Imaging (MRI), fMRI was discovered almost 30 years ago by small changes made in the MR signal that can show neural activity happening in the brain. The BOLD contrast was found by Dr. Ogawa in 1990, and his findings in (Ogawa and Lee, 1990) have shown that BOLD signals can be used to capture the activations in the brain. Due to its high-spatial-resolution and safe scanning method, fMRI is preferred over older scans such as PET and CT scans for studying the FC from the BOLD signals.

2.2.1 MRI Acquisition

An fMRI signal is obtained from the same scanner used for MRI. Figure 2.4 shows the configuration of an MRI scanner. In a scanner, a huge static magnetic field is generated by superconducting electromagnets that have wires cooled down to near absolute zero temperature to allow a coherent and long-lasting current passing through the coils. This method requires less power and cost, thus, makes it more favorable in the recent MRI scanner industry. Currently, MRI scanners can have field strengths ranging from 1.5 to 11 Tesla (T) for human imaging and up to 24T for animals, but the common strengths that are used are 1.5, 3, 4, and 7T (Huettel et al., 2014). Several recent studies have also begin analyzing 10.5T scans in humans and animals to ensure a safe scan in high field strength (Sadeghi-Tarakameh et al., 2020; Yacoub et al., 2020).

The radiofrequency coils play an important role in producing the MR signals, where they are the electromagnetic coils that produce and use electromagnetic fields at the resonant frequencies inside the static magnetic field (thus the term ‘resonance’ in MRI). The coils will send the electromagnetic waves that resonate at the resonant frequency determined by magnetic field strength into the scanned body that has reached

Figure 2.4: A 1.5T MRI scanner (Park et al., 2014). The images acquired are under creative common license.

equilibrium state (where the magnetic moments of atomic nuclei within the body are aligned with the magnetic field). The perturbation of the equilibrium state causes the atomic nuclei to excite and absorb the radiofrequency pulse's energy. The raw MR signal is defined as the electromagnetic energy released by the atomic nuclei after they return to the equilibrium state.

In image formation, the gradient coils that are used to form the MR signal is controlled spatially along x, y, and z axes. The shimming coils are also added to compensate for the inhomogeneities in the static magnetic field caused by the main electromagnet and the gradient coils.

MRI uses atomic nuclei that possess the nuclear magnetic resonance (NMR) property, which requires a magnetic moment and angular momentum to show nuclear magnetic resonance effects when both are present. Because of the high concentration of water molecules in the human body that consists of hydrogen and oxygen, hydrogen atoms are the most common nuclei imaged in the MRI. These atomic nuclei have an intrinsic feature called *spin*.

When a human body is placed into the scanner that has the strong magnetic field, the atomic nuclei will precess aligning to the magnetic field, $\mathbf{B_0}$ causing the net magnetization, $\mathbf{M}$, parallel to the $\mathbf{B_0}$. If the precession is happening at a particular frequency known as Larmor frequency, resonance will occur. Low-energy nuclei will absorb energy and convert the longitudinal magnetization into the transverse magnetization, where this process is called 'excitation.' After the energy is removed, the nuclei will release back the energy absorbed and move back to the low-energy state, restoring the longitudinal magnetization. This energy release provides the signal data that go into the MR image, which we call 'reception.' The MR signal changes over time are commonly known as 'relaxation.'

Depending on the types of relaxation parameters, such as the recovery of the longitudinal magnetization, T_1, and transverse magnetization decay, T_2, we can capture images that have different intensities on different underlying tissues. Figure 2.5 shows the differences between T_1 and T_2 images, for example, the white matter is the brightest in T_1 compared to T_2 image. There is also another decay, a T_2^*, that measures the decay of magnetic field inhomogeneity and the transverse magnetization caused by the relaxation (Chavhan et al., 2009). Thus, the faster T_2^* decays, the more signal intensities in the image are lost.

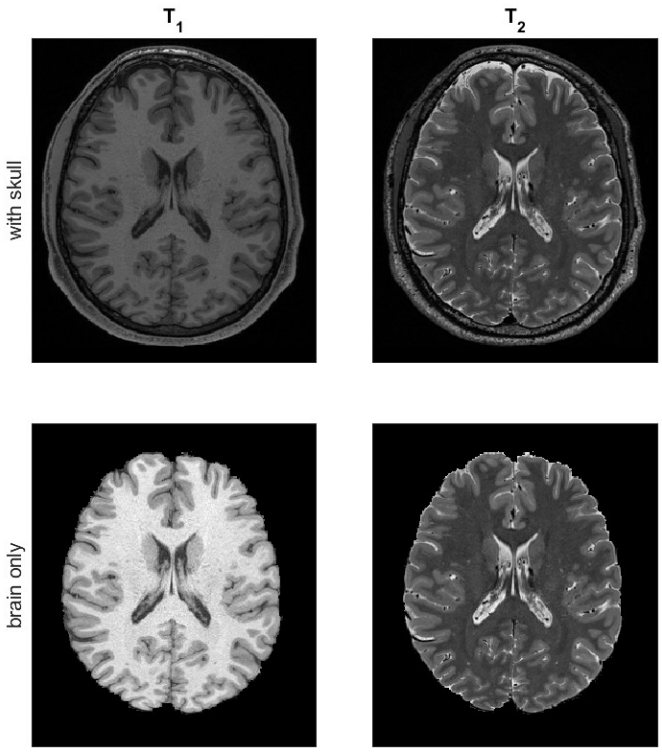

Figure 2.5: Comparison between T_2 (left) and T_1 (right) images obtained from an MRI from dataset in (Glasser et al., 2013). The main difference in these two images can be seen in the color intensities between the gray and white matters.

2.2.2 Image Formation

In an fMRI experiment, instead of capturing the brain tissues into the image, the scanner records the blood-oxygenation-level-dependent (BOLD) signal, which relates to the oxygenated and deoxygenated hemoglobin in the blood that has diamagnetic and paramagnetic properties respectively. (Ogawa and Lee, 1990) described that the differences in the blood oxygenation level could be measured by the T_2^*-weighted contrast studied on rats that breathed air with various levels of oxygenation and using ex-vivo testing using blood vials. These

experiments showed that the MR signal using T_2^* images decreased with the presence of the deoxygenated blood.

Figure 2.6 shows an example of a T_2^*-weighted image which reflects the BOLD contrast of a brain slice. The dark regions which resemble low MR signal correspond to the deoxygenation of the blood, and the bright regions represent the opposite description. One of the acceptable and reasonable hypotheses of these behaviors would be because of the increase in the T_2^* decay done by the oxygenated hemoglobin. High brain activity is expected at this period since the brain is using more energy to perform some activity and thus, needs more oxygen. On the other hand, low brain activity is likely to happen due to the decrease in T_2^* when the deoxygenated blood is in the brain regions.

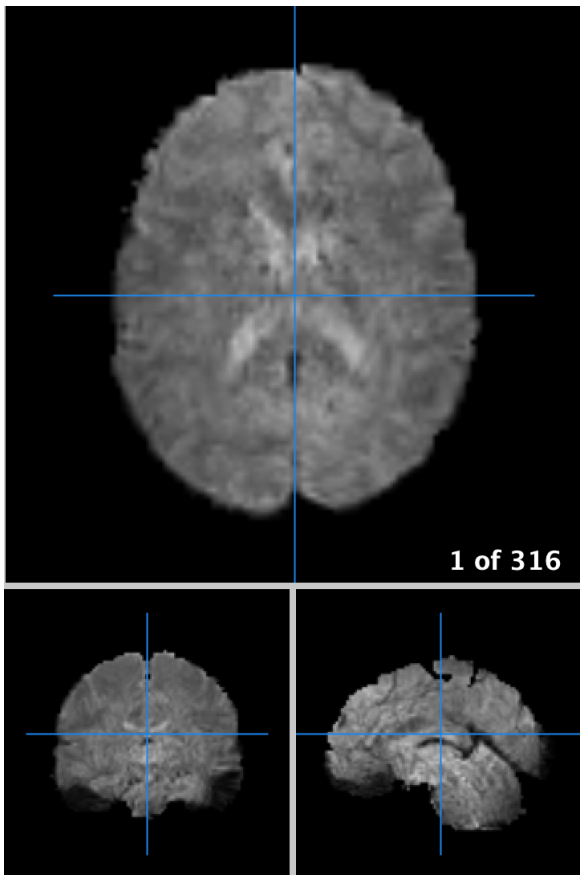

Figure 2.6: An example of a T_2^*-weighted (or BOLD contrast) image obtained from an MRI from dataset in (Glasser et al., 2013)

Each pulse in a brain activity corresponds to the blood flow's time profile called the hemodynamic response (HDR) function, where higher blood oxygenation will produce a higher BOLD signal. One example of an HDR model is shown in Figure 2.7. The HDR is a result of the decrease of the deoxygenated blood in an fMRI voxel (Huettel et al., 2014). As mentioned earlier, research suggests that an increase in the BOLD

signal is due to neuronal activity. However, there is a small negative signal, the 'initial dip', that appears a lot in many fMRI studies for about 1-2 seconds after a stimulus, but this is still a debatable issue as some studies did not report the same behaviors. (Ances, 2004) suggested that this 'initial dip' is caused by an increase of neuronal activity that results in the decrease of oxygenation in the neighborhood capillaries in the early stage before the oxygenated blood is delivered into the veins. Despite the controversy, the MR signal will reach a maximum amplitude and remain until the stimulus is removed. The signal is then decreased to another dip, commonly called an 'undershoot' for underlying causes that are not currently agreed upon (Huettel et al., 2014).

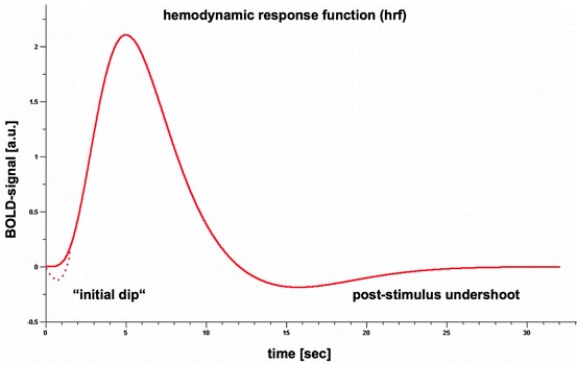

Figure 2.7: A hemodynamic response function model (Scheef and Boecker, 2012).

After getting all the MR signals, the final fMRI data can be visualized as small volumetric regions or voxels v at a time-series t_n, where n = 1,2, ..., N is the number of scans (time) captured in a scanning session (Daubechies et al., 2009). An example to show a 4-D fMRI image is shown in Figure 2.8. Each voxel v_i contains the MR signal value to represent the intensity of the signal across the scanning time. Typically a scanning process lasts for at least 5 minutes, and each scan may have a repetition time (TR), the cycle time between two successive RF signals, usually between 2 to 3 seconds depending on the type of the MRI scanner. In our study here, our primary data have a TR of 0.72 seconds that will result in a single brain image volume every 720 milliseconds.

2.2.3 Functional Connectivity in fMRI

Functional connectivity (FC) is usually represented as the basis of correlations between measurements of human brain activity (Friston, 2011). Friston et. al defined the term as the "statistical dependencies temporal correlations between remote neurophysiological events" (Friston, 2011; Friston et al., 1993). Anatomical connectivity (AC) shows the connections physically between two brain regions (Lee et al., 2003), while effective connectivity (EF) refers to the "influence that one neural system exerts over another" (Friston, 2011). Comparing FC to these two connectivities, FC tends to analyze the regional interactions in the human brain

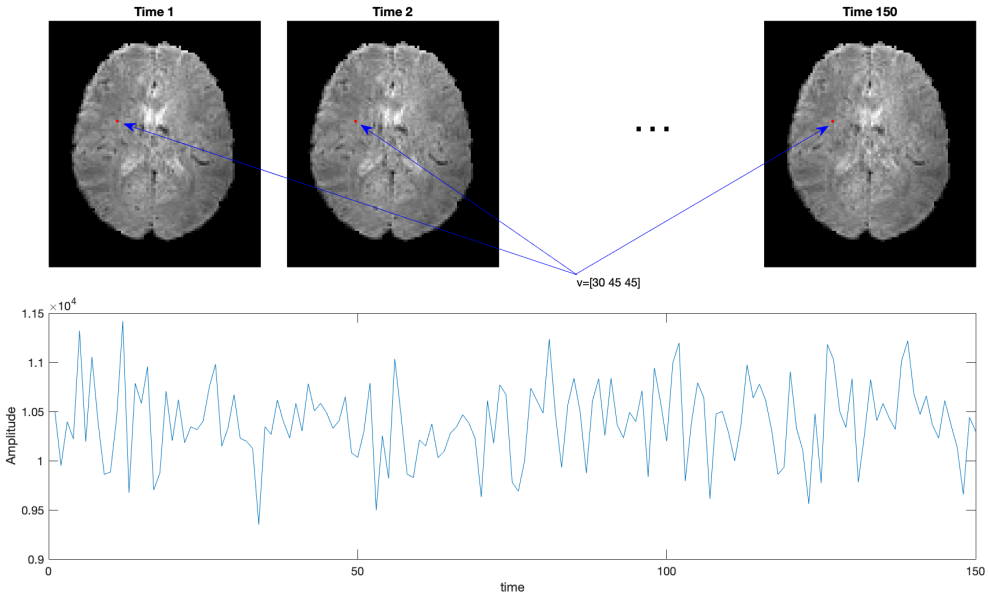

Figure 2.8: An fMRI image configuration with BOLD signal at voxel location $[30,45,45]$ for 150 time points. This fMRI BOLD image was obtained from an MRI from dataset in (Glasser et al., 2013).

at a macro level from different kinds of imaging modalities, including fMRI (Li, Kaiming; Guo, Lei; Nie, Jingxin; Gang, Li; Liu, 2009). We will use the terms connectivity and correlation interchangeably.

In the context of fMRI, Figure 2.9 shows the two most common approaches to study the FC. The first approach calculates the correlation coefficient temporally on the fMRI time-series data before applying the decomposition method to extract the networks as implemented in (Smith et al., 2012). The latter decomposes the fMRI data first into several seeds or regions and networks before the correlation coefficient was calculated based on the components obtained. This method is the most common way to extract the FC matrix, which was applied in (Mayer et al., 2014; Jones et al., 2012; Chang and Glover, 2010; Newton et al., 2007; Beckmann et al., 2005; Allen et al., 2014). A correlation coefficient is defined as the connectivity between all pair voxels or regions that were priorly defined using a manual or a computational method. A commonly used correlation coefficient formula in fMRI analysis is Pearson's correlation coefficient, ρ, that can be written mathematically in Equation 2.1 where X and Y are the two sets of data and the σ_x and σ_y are the standard deviations of X and Y respectively.

$$\rho = \frac{\text{cov}(X,Y)}{\sigma_X \sigma_Y} \tag{2.1}$$

Using FC has helped many researchers to understand the connections between different brain regions.

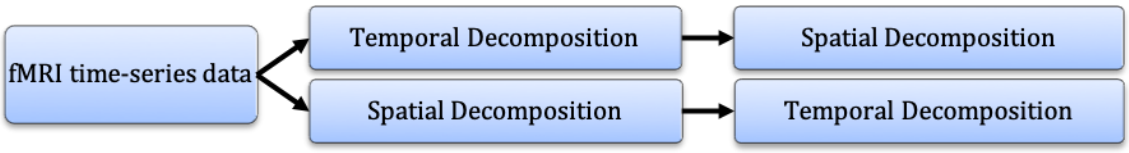

Figure 2.9: Main approaches in fMRI FC analysis.

Convincing results have been established in using fMRI to reveal the interregional correlations between different brain functionalities during resting states (Rogers et al., 2007). Studies have shown evidence of high functional connectivity in specific anatomical regions such as in insula (Cauda et al., 2011; Liu et al., 2018), raphe nuclei (Beliveau et al., 2015), and internal capsule (Gawryluk et al., 2011). These regions are explicitly chosen due to their activations that are believed to be connected with some brain functionalities. Other studies focused on specific brain networks, such as in the DMN (Kiviniemi et al., 2011; Wu et al., 2014; Kucyi and Davis, 2014), which is usually highlighted in the resting-state fMRI.

In recent years, more research has been done on brain-related disease images to investigate the differences between healthy and non-healthy brain functionalities. Abnormalities have been found in the functional networks in patients with Parkinson's disease (Mijalkov et al., 2022), schizophrenia (Sakoglu et al., 2010; Ma et al., 2014; Rolls et al., 2021), and Alzheimer's disease (Jones et al., 2011; Liu et al., 2018). These results have been made available to help assist in the medical diagnosis and treatment of the patients in addition to the current healthcare procedures.

2.3 Principal Component Analysis (PCA) and Independent Component Analysis (ICA)

PCA and ICA have been widely used in medical image analysis, particularly in MRI and fMRI studies. Researchers have shown that various information can be extracted from the brain data using these two methods and their extensions (or modified versions).

The basic idea of using these two methods is to separate a mixed signal coming from multiple sources into individual signals. For example, an audio recording such as from microphones containing voices from different people can be extracted to each individual voice recording (Figure 2.10).

2.3.1 PCA

Among the widely used method for separating multiple signal sources, the most basic method used is the PCA method. PCA has been implemented in many fields, not just in medical image analysis, for decades as it was first formulated in the early 1900s by Pearson (Wold et al., 1987).

As its name suggests, PCA finds the principal components of a set of data, in which the associated

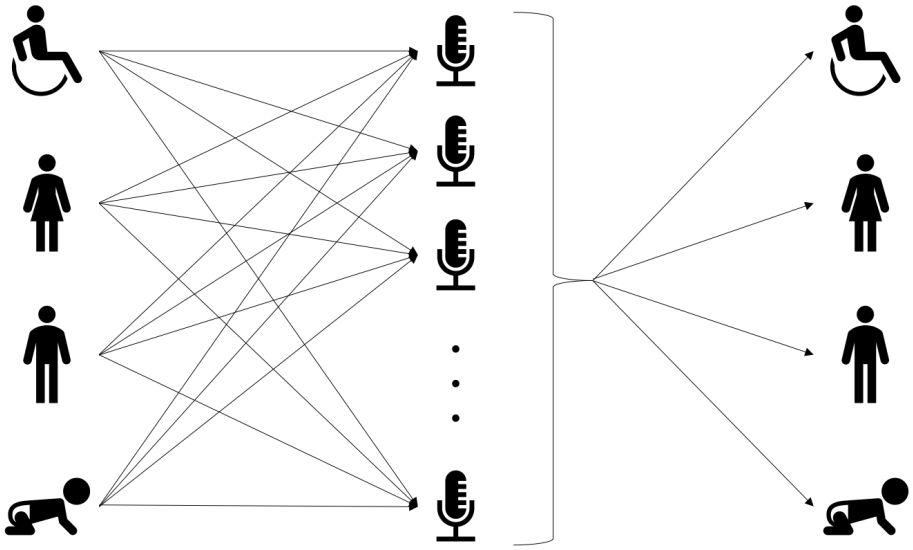

Figure 2.10: An illustration of cocktail party problem

basis vectors are the directions where there is most variance and most spread out. The directions of the data that spread out by different levels of variances are called the eigenvectors with the variances that are normally called eigenvalues. The eigenvector that is associated with the highest eigenvalue is the basis vector associated with the first principal component; hence this method is named PCA. Based on these terms, data can be deconstructed into this mathematical expression,

$$X = AS \tag{2.2}$$

where X is the mixed data that we have, A is a mixing matrix, and S is the original independent data. We want to find an 'unmixing' matrix, W or an approximate of the inverse of A, which would give the best possible approximation of S as in Equation 2.3. Thus, W can be calculated through a PCA algorithm so that we can recover the source data as accurately as possible.

$$S_{approximate} = WX \tag{2.3}$$

PCA can be categorized as a technique for statistical data analysis that can do feature extraction and complex data reduction into a lower dimension. The basic idea of PCA is to find a set of bases that are orthogonal and uncorrelated to each other (Zhan and Yu, 2015). It considers the redundancy between two data elements to separate them into the principal components (Bugli and Lambert, 2007). Singular Value Decomposition (SVD) is a common method used where it decomposes the image into eigenvalues that represents the compo-

nent values and their corresponding eigenvectors. Then, to lower the dimensions of the original image, lower eigenvalues and their corresponding eigenvectors are removed from the decomposed matrices to reconstruct the mixed data in a new representation. PCA is often used on Gaussian data, as the decorrelation of the Gaussian data results in the components being independent of each other.

One of the key properties of PCA is the basis vectors must be orthogonal, and therefore uncorrelated to each other, i.e., the dot product of a two basis vectors pair has to be zero. Independence of the resulting components is not required in general, unlike the Independent Component Analysis (ICA), to be described in the next section. Some of the successful applications in fMRI that use PCA are:

1. Andersen et al. (Andersen et al., 1999) presented a generalized framework for PCA using SVD that was applied to the fMRI data spatially on each time window. Dynamic mapping of activation was then measured by calculating the difference between the mean value of the relaxation rate, R_2*, and the window's R_2* mean.

2. Zhou et al. (Zhou et al., 2014) used PCA in their analysis to determine regions from the fMRI images before they employed the graph theory and machine learning to improve characterization in Autism Spectrum Disorders (ASD).

3. Viviani et al. (Viviani et al., 2005) showed that the PCA is effective to separate the mixed data into the desired signals even with limited or no prior information of the HDR functions as a complement to other component extraction like ICA.

2.3.2 ICA

In contrast with PCA, ICA allows the components to be as independent as possible without forcing them to be strictly orthogonal. The independence property suggests that the output components should be statistically independent. Therefore, each component does not give any information or correlate to other components. Due to its independence, the basis vectors are usually close to orthogonal to each other, although this is not a main focus in ICA, unlike PCA. The dot products of the basis vectors are small, but they are not necessarily zero like PCA component vectors.

Several ways to achieve independent components are by maximizing the nongaussianity of the resulting components and minimizing the mutual information between the data. The Kurtosis method (Hyvärinen et al., 2002) is one popular way to minimize the gaussianity of the resulting vectors by measuring the peak of the data distribution. Entropy minimization from information theory can be used to minimize the mutual information. Because there are many ways to achieve these two goals, several ICA algorithms have been designed, such as:

1. Joint Approximate Diagonalization of Eigenmatrices (JADE) (Cardoso and Souloumiac, 1993) uses the eigenvalue decomposition and then the second and fourth-order cumulant of the matrices diagonalization via the Jacobi method to determine the independent sources.

2. Infomax (Bell and Sejnowski, 1995; Cardoso, 1997) is used to estimate supergaussian independent sources by using the principle of information maximization. Its extension was done by Lee et al. (Lee et al., 1999) to overcome the limitation by adding the subgaussian estimation.

3. fastICA (Hyvärinen and Oja, 2000; Hyvärinen et al., 2002; Hyvärinen, 1999) finds the independent components through minimizing the vectors' gaussianity as opposed to the Infomax. This method is currently more popular as it is fast, less computationally expensive and produces better separation results compared to other ICA methods. MELODIC ICA in the FSL platform uses this probabilistic ICA introduced in (Beckmann et al., 2005) and is one of the popular software used for fMRI studies.

4. Full Blind Source Separation (FBSS) (Li and Adali, 2010; Soldati et al., 2013) exploits the temporal structures of the data by minimizing the entropy rate of the sources.

Because most ICA methods have high computational cost, in medical image processing, PCA, which is known to run faster due to its simplicity, is sometimes integrated with ICA by applying the algorithm to reduce the dimensionality of the data during preprocessing and then apply the ICA for the complete analysis. In many cases, this helps to remove insignificant information to be included in the analysis, such as noise recorded in the images during the scan. As implemented in (Sakoglu et al., 2010) and (Allen et al., 2014), after PCA is applied, they analyzed the 'reduced' fMRI data using Group ICA Of fMRI Toolbox (GIFT) (Rachakonda et al., 2007).

2.3.3 Sliding-window Configuration in fMRI Analysis

As the fMRI research expands, researchers found a variety of approaches to analyze dynamic brain activities using sliding windows. Many studies have recently used the sliding-window approach, such as in (Kiviniemi et al., 2011; Sakoglu et al., 2010; Allen et al., 2014; Karvanen and Theis, 2004; Andersen et al., 1999; Leonardi et al., 2013; Hutchison et al., 2013b; Kucyi and Davis, 2014; Mayer et al., 2014). Some of them believe that windowed data have significant importance in the diagnosis of several illnesses by examining the functional connectivity changes across time. For example, (Mayer et al., 2014) and (Jones et al., 2012) used the sliding-windowed data analysis for better treatment of brain injuries and Alzheimer's disease, respectively.

One way to describe a window in the fMRI dataset is a set of multiple scans within a time range. In a sliding-window study, we then shift the window by several time samples (typically in seconds or number of

scans) with the same window length that allows some overlap of data points from one window to another. In (Kiviniemi et al., 2011), for example, they selected a window, w consisting of 60 scans from the total of L scans and shifted the window by one scan (or 1 TR) (Figure 2.11) before applying any analysis method to each window. Although some researchers have slightly different ways of defining a sliding window, they usually have the same idea of using the sliding windows by transitioning a set of scans from one time window to another. Another study used sliding windows onto the resulting components after the GIFT algorithm was applied to decompose a stack of subjects' fMRI scans (Figure 2.12), which is a slightly different approach than mentioned previously.

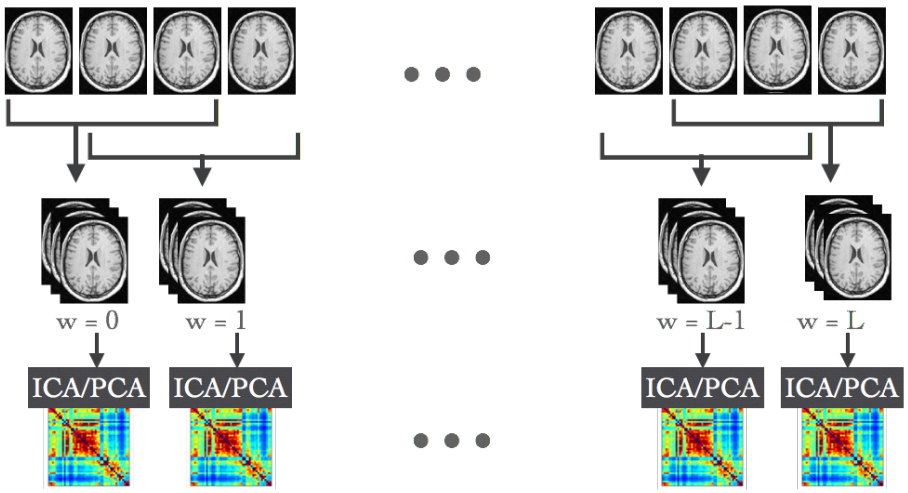

Figure 2.11: One of the sliding-window approaches is where the windows are applied on the fMRI scans before each window is decomposed using PCA or ICA separately as described in (Kiviniemi et al., 2011).

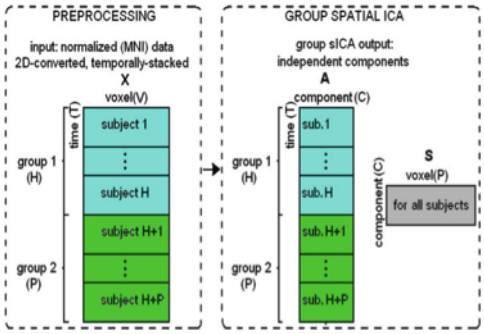

Figure 2.12: GIFT data arrangement for its group ICA (Sakoglu et al., 2010). The data is stacked temporally producing the spatial components. The sliding-window approach is applied onto its resulting ICA components (matrix A).

Determining the size of the window and the number of overlapping scans can also be tricky as it could result in different component values of the windows. (Shakil et al., 2016) evaluated their comparison within 25 to 200 TRs (17 to 129 seconds). Others reported having used the window length ranging from 8 to 240s

(Kiviniemi et al., 2011; Allen et al., 2014; Chang and Glover, 2010). Concerning the number of overlapping scans, most choose to hop only one scan from one window to the next, which means that only the first and last scans are different from the two windows.

In real implementations, many studies that use sliding-window configurations analyze the data using ICA, although few used PCA in their sliding-window fMRI data such as in (Andersen et al., 1999). For example, the basic concept of sliding-window implementation for fMRI analysis was introduced in (Karvanen and Theis, 2004), and they processed the windowed data using ICA to obtain the components to observe the changes. The result showed that small temporal changes could be tracked across the scan between the time windows, proving the advantage of using this approach.

In terms of the FC analysis perspective, several studies use MELODIC ICA and integrate the sliding-window approach in different types of datasets. A study used the sliding-window approach and ICA to confirm the associations between the DMN core regions and subsystems from the daydreaming frequency (DDF) differences in each individual across the time-windows (Kucyi and Davis, 2014). Smith et al. (Smith et al., 2012), on the other hand, ran the MELODIC for spatial decomposition and later applied temporal ICA to identify different networks before the correlation between seeds in each network were computed. Another method proposed was named Sliding Time-Window ICA (SliTICA) that detect spatial maps of the resting-state networks across the scan time (Kiviniemi et al., 2011). They were able to show that there are spatial variabilities in the brain networks, specifically in DMN, even in the absence of a task.

Apart from the typical PCA usage in the data preprocessing before applying ICA into the data, Leonardi et al. (Leonardi et al., 2013) applied a combination of PCA, ICA, and a sliding-window approach, a slightly different approach from the others. The spatial regions from all subjects were first identified using an automated anatomical labeling (AAL) atlas and Pearson's correlation, which later was called FC, were calculated for each time-window. The FCs were concatenated and applied to PCA and then group-ICA, yielding the time-dependent weights across the subjects.

CHAPTER 3

Modified Principal Component Analysis in sliding windowed fMRI data

Adapted from: Nazirah et al., "Modified Principal Component Analysis in sliding windowed fMRI data"

The current available methods for fMRI data decomposition are mostly done as a whole ignoring the possibility of important information variability over time. While some studies applied sliding windows to the data, the independence and continuity of the data decomposition is not being taken into account. Our proposed method, the modified Principal Component Analysis (PCA) tries to force the basis vectors to be as orthogonal and independent as possible. We showed that the proposed method maintains low dot products regardless how big is the window size and overlapping window. In comparison to the classical PCA and Independent Component Analysis (ICA) methods, the method yielded the lowest dot products among them. Using this method also provided some insights on the changes in the fMRI data where there could be possibility of brain synchronizing when most of the brain regions are highly correlated.

3.1 Introduction

fMRI technology has emerged in brain connectivity studies since it was introduced in early 1990s (Ogawa and Lee, 1990). As the fMRI research expanded, researchers found a variety of approaches to analyze the dynamic brain activities using sliding windows. A lot of studies have been done recently using sliding window approach such as in (Kiviniemi et al., 2011; Sakoglu et al., 2010; Allen et al., 2014; Karvanen and Theis, 2004; Andersen et al., 1999; Leonardi et al., 2013; Hutchison et al., 2013b; Kucyi and Davis, 2014; Mayer et al., 2014). Some of them believe that the windowed data have a significant importance in diagnosis of certain illness by examining the functional connectivity changes across time. For example, (Mayer et al., 2014) and (Jones et al., 2012) used the sliding windowed data analysis for better treatment of brain injuries and Alzheimer's disease respectively.

One way to describe a window in fMRI dataset is a set of multiple scans within a certain range of time. In a sliding window study, we then shift the window by a number of time samples (typically in seconds or number of scans) with the same window length that will allow some overlap of data points from a window to another. In (Kiviniemi et al., 2011) for example, they selected a window, w consisting of 60 scans from the total of L scans and shifted the window by one scan as illustrated in Figure 2.11 before applying any analysis method to each window. Although some researches have slightly different ways to define a sliding

window, normally they have the same idea of using sliding window by transitioning a set of scans from one time window to another.

Determining the size window and number of overlapping scans can also be tricky as it will result in different component values of the windows. A study have (Shakil et al., 2016) evaluated their comparison within 25 to 200 TRs (17 to 129 seconds) while the others reported to have used the window length ranging from 8 to 240 seconds (Kiviniemi et al., 2011; Allen et al., 2014; Chang and Glover, 2010). Concerning the number of overlapping scans, most choose to hop only one scan from one window to the next, which means that only the first and last scans are different from the two windows.

Most studies that applied windowed data applied Independent Component Analysis (ICA) or its derivatives to extract the spatial information across time. There are several studies that use Principal Component Analysis (PCA) with sliding window configuration, but a lot of research groups use combination of both PCA and ICA with PCA is typically used in data preprocessing to reduce the number of components to be decomposed by ICA.

Andersen et al. (Andersen et al., 1999) began to learn the dynamics of human brain connectivity by extracting the the windowed data using PCA. presented a generalized framework for PCA using SVD that was applied on the fMRI data spatially on each window. Each window was selected as 10 images per window and sledded across the time-series.

ICA approaches are more popular in this sliding window studies due to the ease of using the available softwares and produced better desired results. Makeig et al. (Makeig et al., 2000) used a 'moving-window' ICA approach on 3-s electroencephalographic (EEG) data. They defined the window data by windowing each epoch within overlapping 500-ms (128-point) windows successively offset by 5 samples (20 ms). Multiple fMRI studies have used GIFT (Sakoglu et al., 2010; Allen et al., 2014; Mayer et al., 2014), a software that group multiple subjects and slide the window across the subjects as shown in Figure 2.12. Some of these procedures include PCA methods as well as part of the data preprocessing to reduce the amount of components to be analyzed using ICA.

In the sliding-window point of view, several studies believe that the sliding-window approach for functional connectivity is a promising way to create better representation for human brain functional connectivity across time-series. (Zilverstand et al., 2014) demonstrated that using windowed FC could provide unique information on task difficulty from the task connectivity which is important to further understand ongoing brain processes. They found that even in a very short time-window could provide valid information about certain aspects in a task. (Sakoglu et al., 2010) also suggested that there may be a clinical relevance in measuring the dynamic FC after discovering group differences in healthy and schizophrenia patients on sliding-windowed ICA derived time series during an auditory oddball task. Interpreting the variation in the FC correlation is not

usually straightforward as mentioned in (Hutchison et al., 2013a), thus, sliding-window analysis is an option to ease the process in understanding the dynamic FC of the brain.

In this paper, we will introduce a modified PCA method for sliding window data purposes. This technique enforces the basis vectors to be very close to orthogonal by taking the 'information'from the previous window when computing the current window's components. The proposed method has the following advantages, but not limited to, over the classical PCA in fMRI analysis:

1. PCA forces all the basis vectors to be orthogonal to each other, thus, making the result a bit inaccurate for a dynamic data like fMRI. While in ICA, it is unclear how independent the data are between the components within specific windows. Thus, designing a method that could force the components to be close to orthogonality would result the components to be as orthogonal and independent as possible from one to another.

2. Sliding window configuration gives us more understanding when looking a functional data like fMRI that changes through time. Our results shows there is information on how signal changes through-out the scanning process.

3. The proposed method ensures the continuity of the window frames across the whole data. While traditional PCA or many other methods are normally applied into windowed data separately from each window, this modified PCA involves the previous window into the current window coefficient calculation.

4. In comparison to Sliding Window Adaptive SVD (SWASVD) (Badeau et al., 2004) and Sliding Window Proper Orthogonal Decomposition (SWPOD) (Clement et al., 2014), for example, the proposed methods provide only a single set of components for each timepoint. The other methods produce a set of components for each window that will result in multiple components in a timepoint.

The paper is organized as follows. In section 3.2, we introduce the Modified PCA algorithm and its restrictions on the components' output. The results of using this method on an fMRI data are presented in Section 3.3 and 3.4. Finally, Section 3.5 summarizes the main conclusions and suggestions for future directions.

3.2 Modified PCA Algorithm

In this method, a window is defined as a set of fMRI data of N_{vox} brain voxels within a range of time, N_{win}. A sliding window is defined to be the window shifted by N_{hop} timepoints from the beginning of the previous window. This is similar to what has been done in (Kiviniemi et al., 2011), but with bigger size N_{hop}. We

believe that bigger N_{hop} would give more reliable data and more realistic to see the functional movement inside the brain from one window to another.

3.2.1 The Proposed Method

Let X be the whole-brain fMRI data with T timepoints and N voxels. The cross-correlation of all the voxels with size of $T \times T$ can be calculated as

$$R = XX^T \tag{3.1}$$

Let I be a diagonal matrix with ones on the diagonal with size of $N_{win} \times N_{win}$. Then, let $\widetilde{I}_t$ be an $T \times T$ matrix with zeros except at row t to $t + (N_{win} - 1)$ and column t to $t + (N_{win} - 1)$ which is replaced with matrix I as shown in Equation 3.3 and 3.4.

$$I = \begin{bmatrix} 1 & 0 & 0 \\ 0 & \ddots & 0 \\ 0 & 0 & 1 \end{bmatrix} \tag{3.2}$$

$$\widetilde{I}_t = \begin{bmatrix} 0 & 0 & 0 & 0 \\ 0 & I & 0 & 0 \\ 0 & 0 & 0 & 0 \\ 0 & 0 & 0 & 0 \end{bmatrix} \tag{3.3}$$

$$= \begin{array}{c} \\ N_{win}*t+1 \\ \\ \\ \\ N_{win}*t \end{array} \begin{array}{c} \begin{array}{cccccc} & & N_{win}*t+1 & & & N_{win}*t \end{array} \\ \begin{bmatrix} 0 & 0 & 0 & 0 & 0 & 0 \\ 0 & 1 & 0 & 0 & 0 & 0 \\ 0 & 0 & 1 & 0 & 0 & 0 \\ 0 & 0 & 0 & \ddots & 0 & 0 \\ 0 & 0 & 0 & 0 & 1 & 0 \\ 0 & 0 & 0 & 0 & 0 & 0 \end{bmatrix} \end{array} \tag{3.4}$$

If we use PCA strictly, the orthogonality rules require that $c_i^T c_{i+1}$ has to be equal to 1 and thus forcing $c_i I_t c_{i+1}$ to be zero. Our method is designed to loosen the constraint to at least a minimum instead of strictly orthogonal as in PCA.

For the first component values for each timepoint, c_1 is obtained from first column of the left singular vectors of the normal SVD method. This will result in c_1 as a vector size of $T \times 1$. For the subsequent

component values, we want to choose the $c_i I_t c_{i+1}$ to be as minimum as possible to ensure the components to be as orthogonal as possible.

3.2.2 Maximization of Subsequent Components Fractions

To obtain the subsequent components, we need to maximize

$$\frac{c_i^T R c_i}{c_i^T (D^T D) c_i} \tag{3.5}$$

where

$$D = \begin{bmatrix} c_{i-1}^T \widetilde{I}_1 \\ c_{i-1}^T \widetilde{I}_2 \\ c_{i-1}^T \widetilde{I}_3 \\ \vdots \\ c_{i-1}^T \widetilde{I}_n \end{bmatrix} \tag{3.6}$$

and n is the total number of windows.

One way to maximize the ratio in Equation 3.5 is by minimizing the denominator through restricting the component i.

Algorithm 1 Ratio Maximization

1: $R = XX^T$
2: $c_1 \leftarrow$ First component from PCA(R)
3: **for** each subsequent component i, c_i **do**
4: **for** each window j **do**
5: Create I_j
6: **end for**
7: Create D
8: Find c_i that minimizes $c_i^T (D^T D) c_i$
9: **end for**

The whole algorithm from Section 3.2.1 and 3.2.2 is summarized in Algorithm 1. As the final outcome, each window will have a set of basis vectors. For example, a set of data containing 1200 timepoints and processed with sliding-window configuration of N_{win} and N_{hop} of 20 and 4 respectively will have five basis vectors of length 1200.

3.3 fMRI Analysis Methodology

3.3.1 fMRI Data

The dataset used in the preparation of this work was obtained from the Human Connectome Project (HCP) database, a publicly available resource with high-resolution brain structural and functional MRI scans.

The HCP subjects were drawn from a population of 1200 healthy adults between 22 to 35 years old. A set of 16 resting-state fMRI data were randomly selected from the HCP database. All HCP subjects were scanned using a customized Siemens Skyra 3T MRI scanner system using a 32-channel head coil. BOLD signals were acquired using a gradient-echo EPI sequence with a repetition time (TR) of 720 ms, echo time (TE) of 33 ms, and isotropic voxel size of $2 \times 2 \times 2$ mm acquired in 72 slices. The size of each image matrix is $104 \times 91 \times 91$ voxels. All other details for these data can be referred in (Glasser et al., 2013).

Before applying the methods described in previous sections into fMRI data, the data was first preprocessed to remove noises and realigned. The modified PCA was then applied to the corrected data with different combinations of N_{win} and N_{hop} to observe the differences and how they affect the component values. Each subject was processed independently, therefore, providing 16 different sets of components.

3.3.2 Instantaneous Whole Brain Correlation (IWBC) Patterns

In order to analyze the pattern of the component values, we compare the components' pattern flows with the pattern of the IWBC, the sum of correlation value of the whole brain voxels at each timepoint. In reference from the (Bell, 2018) and (Tagliazucchi et al., 2012a), this will allow us to observe whether there is a connection between the time where the whole brain has high correlation value and the value in the components obtained from the modified PCA method. If we have $x[i]$ is the signal from the ith voxel in X, for each timepoint n, we can calculate the IWBC generalized from (Bell, 2018) as in Equation 3.7:

$$IWBC[n] = \sum_{i=1}^{N_{vox}} \sum_{j=1}^{N_{vox}} x[i]x[j] \tag{3.7}$$

3.4 Results and Discussion

3.4.1 Maximum Number of Components

As a result of the modified PCA suggested in this paper, there are some restrictions to the number of components that can be extracted through this method.

Figure 3.1 shows that as the window hops further from one window to another (i.e smaller number of N_{hop}), the maximum number of components will be limited. As N_{hop} lowers down, the size of D will decreases and thus, c_i exists until $N_{hop} + 1$. In conclusion, regardless of the size of the window, the maximum number of components using our method is limited to

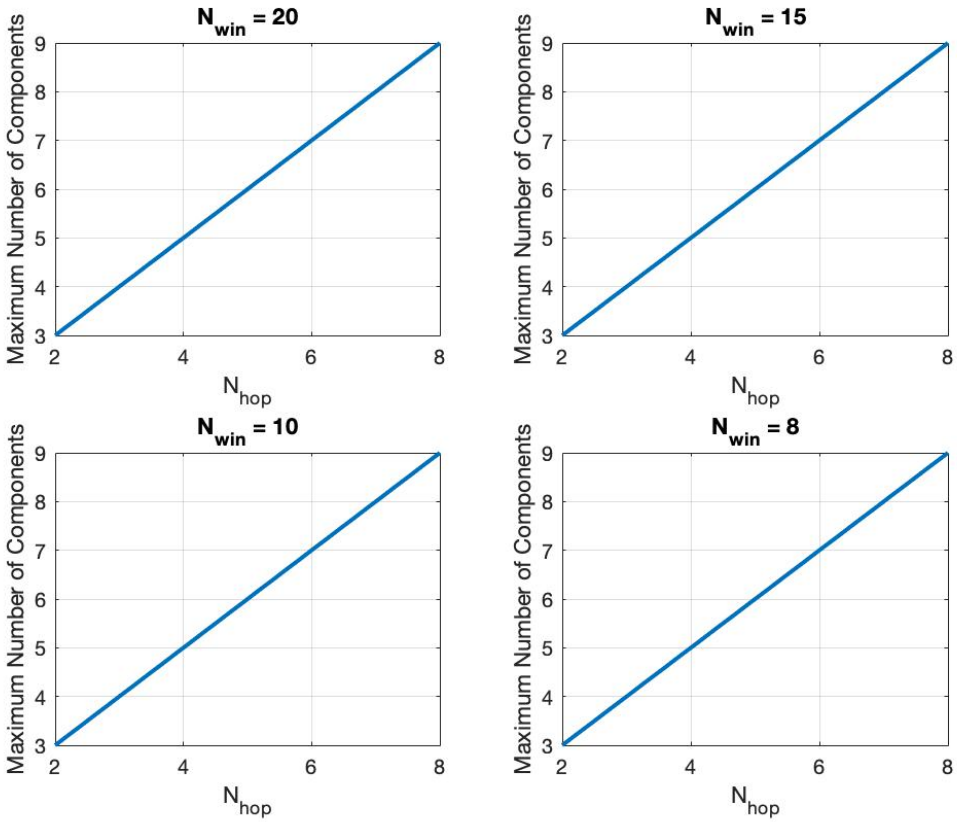

Figure 3.1: Maximum number of components for different N_{hop} and N_{win}.

$$max_c = N_{hop} + 1 \tag{3.8}$$

Having a limited number of components will limit the number of features that can be extracted from the data, but this will also allow us to reduce the unnecessary data that have very low component values.

3.4.2 Size of N_{hop} and N_{win}

We analyzed several configurations of different N_{hop} and N_{win} as the result shown in Figure 3.2. We plotted the average dot products of each two components across 16 subjects. On average, the sizes of N_{hop} and N_{win} do not affect much the orthogonality of the basis vectors. All configurations with N_{win} = 20 and four different N_{hop} result in dot products close to zero. We choose N_{hop} to be 4 due to the stability of the dot products that do not change a lot across N_{win} and the jump from one window to another is not very small nor big to analyze the change from one window to another. Although $N_{win} = 60$ shows the lowest average dot products across N_{hop}, we would like to see more changes across the data that we have, therefore, we choose a moderate number of N_{win} to continue our analysis.

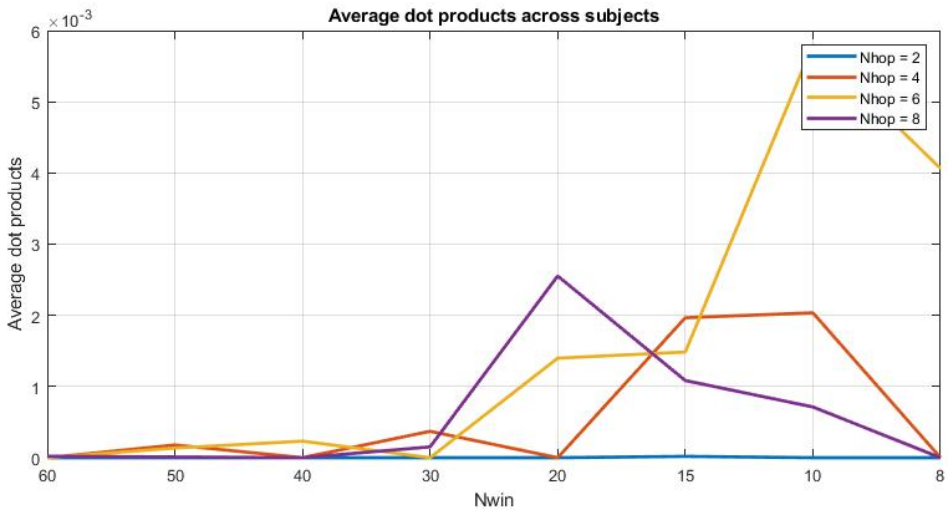

Figure 3.2: Average dot products for different N_{hop} and N_{win} across 16 subjects.

3.4.3 Orthogonality of Components

Table 3.1: Average windowed Dot products of a subject with different N_{win} and $N_{hop} = 4$

$\mathbf{C_i \cdot C_j}$	$\mathbf{N_{win} = 20}$	$\mathbf{N_{win} = 15}$	$\mathbf{N_{win} = 10}$	$\mathbf{N_{win} = 8}$
$C_1 \cdot C_2$	-3.48e^{-20}	8.22e^{-20}	-2.75e^{-20}	2.56e^{-20}
$C_1 \cdot C_3$	4.59e^{-20}	6.22e^{-20}	-1.07e^{-19}	9.09e^{-20}
$C_1 \cdot C_4$	-2.14e^{-19}	8.22e^{-20}	3.12e^{-20}	-1.06e^{-20}
$C_1 \cdot C_5$	1.92e^{-19}	3.49e^{-19}	1.45e^{-18}	-7.51e^{-20}
$C_2 \cdot C_3$	1.08e^{-19}	-2.84e^{-20}	1.12e^{-19}	3.14e^{-20}
$C_2 \cdot C_4$	-3.47e^{-19}	2.64e^{-19}	1.27e^{-19}	-4.20e^{-20}
$C_2 \cdot C_5$	-1.39e^{-19}	3.93e^{-19}	2.77e^{-20}	5.02e^{-21}
$C_3 \cdot C_4$	3.65e^{-19}	-1.06e^{-19}	-2.31e^{-19}	1.13e^{-19}
$C_3 \cdot C_5$	-1.45e^{-19}	3.07e^{-19}	-6.50e^{-20}	5.97e^{-21}
$C_4 \cdot C_5$	7.32e^{-20}	-8.57e^{-19}	-6.64e^{-20}	5.33e^{-20}

To assess the effectiveness of this method, we measured the dot products on each window for each subject with four different N_{win} and average the windows' dot products for all components' dot products. We also measured the dot products given that all the windowed component values are combined into one single set of data. All these data are measured with $N_{hop} = 4$.

Table 3.1 shows the result of the average of the dot products of each windowed two components in a single subject. The very small dot products show that basis vectors are essentially orthogonal to each other, thus, we can say we are close to non-windowed PCA that will force the components to be orthogonal but will have lighter restrictions when computing the components' values. In contrast, if we use the traditional PCA on windowed data, we cannot guarantee the dot products to be near zero. Since the traditional PCA

only guarantees the basis vectors to be orthogonal on the currently analyzed windowed data, it cannot expand the orthogonality to a combination of multiple windows or when we extract a window of data from resulting basis vectors. In fact, we might get sometimes a very high dot products that are close to 1 as shown in Table 3.2. Thus, the vectors are not guaranteed to be orthogonal to each other.

Table 3.2: Average windowed Dot products of a subject with different N_{win} and N_{hop} = 4 using classical PCA on windowed data

$\mathbf{C_i \cdot C_j}$	$\mathbf{N_{win} = 20}$	$\mathbf{N_{win} = 15}$	$\mathbf{N_{win} = 10}$	$\mathbf{N_{win} = 8}$
$C_1 \cdot C_2$	0.8635	0.9044	0.8969	0.8527
$C_1 \cdot C_3$	-0.5858	-0.5808	-0.4267	0.0024
$C_1 \cdot C_4$	-0.0736	-0.1601	0.1514	0.3518
$C_1 \cdot C_5$	0.1277	0.2182	-0.2277	$8.2382e^{-4}$
$C_2 \cdot C_3$	-0.7573	-0.6629	-0.6850	-0.4851
$C_2 \cdot C_4$	-0.3480	-0.3259	-0.1446	-0.0043
$C_2 \cdot C_5$	-0.0371	0.0666	-0.0991	-0.1001
$C_3 \cdot C_4$	0.7948	0.5437	0.7577	0.7483
$C_3 \cdot C_5$	0.2812	0.2178	-0.3110	$7.0743e^{-5}$
$C_4 \cdot C_5$	0.4743	0.7393	-0.7562	-0.5402

In another comparison, we tried comparing with other methods such as Independent Component Analysis (ICA) using FastICA (Hyvärinen and Oja, 2000) and Sliding Window Proper Orthogonal Decomposition (SWPOD) (Clement et al., 2014). SWPOD and classical ICA have localized component values for each window just like how we compare the classical PCA on windowed data which is different than our method that creates a whole series of components for each timepoint. If we combine the components for a timepoint from different windows, these will not guarantee the orthogonality of the full time series components as presented in Table 3.3. Although the fastICA method yields low dot products, the proposed modified PCA method gives better orthogonality.

3.4.4 Connectivity Pattern Analysis: An Application

As a lot of previous studies has shown the importances of looking at fMRI data in sliding window way, we extracted more interesting findings using our proposed method.

3.4.4.1 Connection Between Whole Brain Avalanche and the Windowed Coefficients

Measuring the standard deviation of the voxel coefficients from our proposed method gave us some insights on their relationship with the instantaneous WBC pattern calculated in Section 3.3.2. We compare the IWBC pattern with the windowed voxel coefficients, β for each time window w and coefficient i, where

$$\beta_i[w] = c_i[w]^{-1} X[w] \tag{3.9}$$

Table 3.3: Dot products of a subject with N_{win} = 20 and N_{hop} = 4 using classical PCA and fastICA on windowed data

$\mathbf{C_i} \cdot \mathbf{C_j}$	Modified PCA	Classical PCA/SWPOD	fastICA
$C_1 \cdot C_2$	-3.48e^{-20}	0.8635	6.6132e^{-4}
$C_1 \cdot C_3$	4.59e^{-20}	-0.5858	0.0439
$C_1 \cdot C_4$	-2.14e^{-19}	-0.0736	0.0359
$C_1 \cdot C_5$	1.92e^{-19}	0.1277	0.0329
$C_2 \cdot C_3$	1.08e^{-19}	-0.7573	0.0018
$C_2 \cdot C_4$	-3.47e^{-19}	-0.3480	-0.0232
$C_2 \cdot C_5$	-1.39e^{-19}	-0.0371	0.0029
$C_3 \cdot C_4$	3.65e^{-19}	0.7948	-0.0068
$C_3 \cdot C_5$	-1.45e^{-19}	0.2812	0.0053
$C_4 \cdot C_5$	7.32e^{-20}	0.4743	0.0077

A small standard deviation for each coefficient number (in this example, since we use N_{hop} and N_{win} to be 4 and 20 respectively, there will be 5 sets of coefficient numbers for each window) means all coefficients have very small variation from one another. If we multiply each standard deviation (Equation 3.10), and call it as a *'standard deviation volume'* (SDV) for each window w as in Equation 3.11,

$$\sigma_i[w] = std(\beta_i[w]) \tag{3.10}$$

$$SDV[w] = \prod_{i}^{max_c} \sigma_i[w] \tag{3.11}$$

we can see the patterns connected closely with the instantaneous WBC plot. The SDV values maintains to one of the lowest values at the high peaks of the IWBC as shown in Figure 3.3. As the highest peak of the IWBC joins a window, the SDV begins to drop and then reach to the local minimum. Three highest IWBC point and their respective SDV values (i.e for a single IWBC point, there will be SDV values representing each window). There are other windows that have SDV values to collapse to the local minimum that are possible due to the other brain voxels' activations at the timepoint.

3.4.4.2 Window Centered on Avalanche

We analyzed the coefficients of our modified PCA when the IWBC peaks are at the center of the windows. The standard deviations between component values can be up to 10 times smaller compared to standard deviations of component values using classical PCA. This is true in either in windows that have high IWBC peaks or using 800 and 1000 voxels as shown in Table 3.4, 3.5, and 3.6.

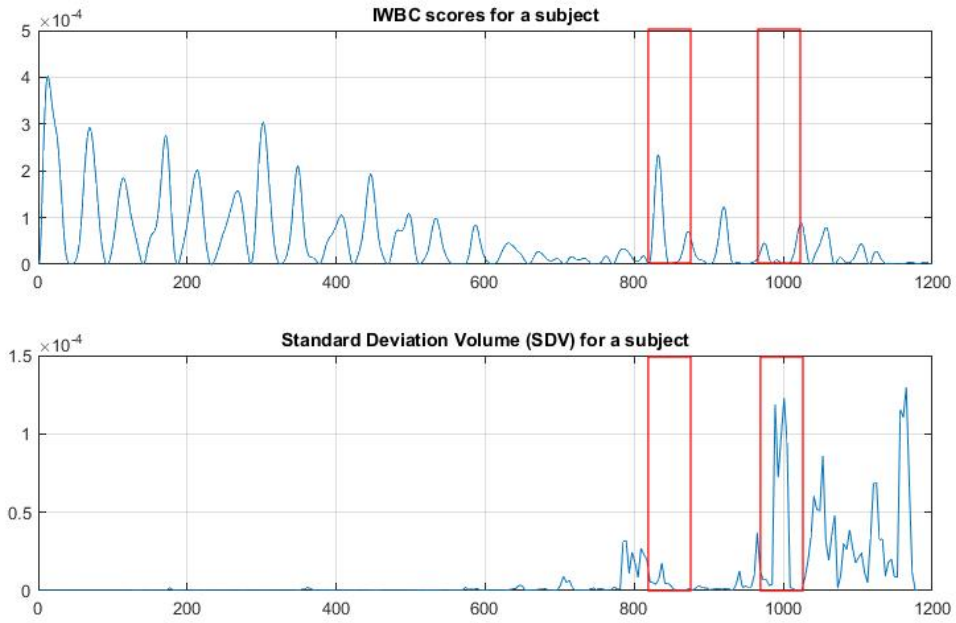

Figure 3.3: Standard Deviation Volume for a single subject. Calculations were based on N_{win} = 20 and N_{hop} = 4. Two sets of peak transitions were shown in the red boxes. As the highest peaks joined in the window, the standard deviation volume starts to drop and begin to increase again after the peak has reached the center of a window.

3.5 Conclusions and Future Directions

We have presented a new method to extract new information sliding window data especially in fMRI studies. The modified PCA method successfully ensure the components to be as orthogonal as possible despite the data to be windowed or not. This method provides continuity of the windows' components by taking the information from the preivous window into computing the next component values, unlike classical PCA that does the decomposition independently.

We successfully showed that using modified PCA, information like human brain synchronization can be

Table 3.4: Average Standard deviation of the components' values for N_{win} = 20 and N_{hop} = 4 using Modified and Classical PCA methods on 60 IWBC peaks

Component Number	Modified PCA	PCA
1	$6.0784e^{-06}$	0.057101
2	0.022206	0.246110
3	0.017152	0.159650
4	0.012728	0.282829
5	0.003951	0.337059

Table 3.5: Average Standard deviation of the components' values for N_{win} = 20 and N_{hop} = 4 using Modified and Classical PCA methods on 800 time points

Component Number	Modified PCA	PCA
1	$3.095e^{-06}$	0.074584
2	0.0189140	0.268950
3	0.0169386	0.150519
4	0.0130408	0.287674
5	0.0073624	0.336862

Table 3.6: Average Standard deviation of the components' values for N_{win} = 20 and N_{hop} = 4 using Modified and Classical PCA methods on 1000 time points

Component Number	Modified PCA	PCA
1	$3.10344e^{-06}$	0.07466
2	0.01768	0.26862
3	0.01637	0.15070
4	0.01404	0.28772
5	0.01056	0.33652

seen. When most of the brain parts are highly activated, most of the brain voxel coefficients are very close to each other. While on other time where not many brain parts are activated, the brain voxel coefficients are random, possibly due to only small partition of the brains are highly activated.

For future considerations, an expansion for this method can be considered to have more components than what is available from this current method. There are also possibilities that more information can be extracted and noises from small components can be removed from the data. Such information and denoising configurations will help in fMRI studies to provide more accurate analysis of human brains.

CHAPTER 4

Visualization of spatio-temporal dynamics of brain activity avalanches in fMRI signals

Adapted from: Nazirah et al., "Visualization of spatio-temporal dynamics of brain activity avalanches in fMRI signals" [submitted for publication]

Sliding-window analysis approaches are often used to analyze the changes in signal properties over time. However, in its original form, Principal Components Analysis (PCA) is not designed for sliding windows. The proposed modified sliding-window PCA (mPCASW) algorithm provides a simple and fast way to explore changes in signal properties over time. Using the fundamental energy compaction aspect of PCA, a set of components can be decomposed into a meaningful representation of the signal, which could uncover transient changes in the dataset. The resulting components show significant patterns in the data compared to conventional methods like Independent Component Analysis (ICA) or regular PCA, showing high-value changes only in several components. We also found that there are possible 'synchronizations' happening around the avalanches of the data, which would allow us to see the connection between each point in the dataset. We also illustrated the mPCASW performance, advantages, and limitations by its application to the resting-state and sleeping-state functional Magnetic Resonance Images (fMRI) studies. This study reveals the differences in signal changes in different components from fMRI signals, either using the whole brain dataset or a specific brain region.

4.1 Introduction

Principal component analysis (PCA), as applied to time series, is a compact and powerful signal decomposition and representation technique that has been in use for a considerable time. PCA produces an orthonormal set of basis vectors which are the eigenvectors of a covariance matrix. Suppose you have a set of M time series, $x_i[n]$, where $i = 1,\ldots,M$ and $n = 0,1,\ldots,N-1$. These series can be represented as vectors where the elements of the $N \times 1$ vector $\underline{\mathbf{x}}_i$ are simply the elements of $x_i[n]$,$n = 0,\ldots,N-1$, and the average of the M time series is a vector given by

$$\underline{\mu} = \frac{1}{M}\sum_{i=1}^{M}\underline{\mathbf{x}}_i \tag{4.1}$$

The covariance matrix associated with this set of time series may be estimated as follows:

$$K_{xx} \;=\; \frac{1}{M-1}\sum_{i=1}^{M}\left(\underline{x}_i - \underline{\mu}\right)\left(\underline{x}_i - \underline{\mu}\right)^T \tag{4.2}$$

As for this covariance matrix, these basis vectors maximally concentrate the signal energy, as shown by the associated eigenvalues. That is to say, the eigenvector associated with the largest eigenvalue will represent the largest amount of signal energy, as expressed in the covariance matrix. The signal energy can also be shown to be maximally concentrated on each of the remaining eigenvectors in the order of decreasing sizes of the eigenvalues. This concentration of signal energy is one reason PCA has been used widely for dimensionality reduction.

However, PCA is typically used to analyze the time series in its entirety and thus does not reveal changes in the signal's decomposition over time. In other words, it has no local temporal focus, as can be found in sliding window techniques or time-frequency representations such as wavelets or spectrograms. Wavelets and spectrograms do indeed reveal time-varying characteristics of signals but typically do so in a time-frequency (spectrograms) or time-scale (wavelets) representation form and do not particularly try to concentrate signal energy on a set of basis vectors as PCA does. We desire to analyze changes in signal decomposition or representation using an approach like a sliding window approach while retaining at least some of PCA's signal energy concentration behavior. We hypothesize that energy concentration may more clearly demonstrate changes in signal decomposition compared to other time-frequency and time-scale types of representations and a different type of time-varying signal decomposition.

We could simply apply PCA independently to each window in a sliding window analysis method; however, this yields some problems. For example, the decomposition for each window, being independently computed, would have different sets of basis vectors from all other windows. This output would make it difficult to make a clear comparison between the representations of different windows. It would be desirable to find a set of basis vectors, where each set extends over the entire length of the signal yet still exhibits orthogonality and energy concentration over the corresponding windowed portions of the signal and the basis vectors. We present a way of finding a set of basis vectors that exhibits such a "PCA-like" behavior over sliding windows.

A popular alternative to PCA is Independent Component Analysis (ICA), which decomposes the signal by maximizing independence between the basis vectors. Independence causes weaker connections between the basis vectors where not all cases result in uncorrelatedness, only in certain data types. On the other hand, orthogonality is the primary key to the PCA method, which secures the independence and uncorrelatedness of two sets of basis vectors.

In multiple signal processing applications, the sliding-window correlations approach maintains to be popular over other statistical methods to evaluate time-varying time series connectivity, such as time-frequency analyses or data-driven modelings. It could also reduce the abruptness of signal changes as each signal window contains a portion of the previous and the following windows data. Algorithms such as (Badeau et al.,

2004; Wang et al., 2018; Clement et al., 2014) have used the sliding-window approach in their signal processing to provide more robust signal changes analysis either in time or frequency domain. In brain connectivity studies, the sliding-window approach has been incorporated in many ways as applied in (Allen et al., 2014; Hutchison et al., 2013b; Mokhtari et al., 2019; Kiviniemi et al., 2011).

Several studies have summarized the factors included in designing a sliding window for a set of signals. (Mokhtari et al., 2019) showed the effects of different window settings on dynamic connectivity estimation like in the human brain signals and introduced a modulated rectangular window called mRect to overcome the unwanted spectral modulations in the frequency domain. Many studies use typical windows such as rectangular and tapered windows to window the data signal before processing is done. Another factor that is usually needed to be taken into consideration is the window size selection. The window size should be a minimum to have a good analysis result without eliminating the information that we can get from the signal (Shakil et al., 2015; Leonardi et al., 2013).

In some other studies, investigations of the brain fMRI using avalanches have become more attractive after Tagliazucchi et al. introduced the idea of spatio-temporal avalanche of spontaneous brain activity, which used point process analysis (PPA) technique (Tagliazucchi et al., 2012b, 2016). Earlier, another "neuronal avalanches" term was introduced that represents the number of continuous activities recorded between time-spaces of no activity at all (Beggs and Plenz, 2003). We defined another type of avalanche called Instantaneous Whole Brain Correlation (IWBC), which calculates the magnitude of whole-brain correlation at each increment of time, which can be done using seed-based regions (Bell, 2018) or all of the brain voxels. These brain avalanches rely on temporally local brain signals; therefore, they could benefit from the results of our improved method for sliding-window signal decomposition.

In this paper, we will describe and expand the technique from modified PCA for sliding-window (mPCASW) in (Mohd Khairi et al., 2019). Since the original algorithm only produces a limited number of components, we extend it by running the same procedure multiple times to obtain more basis vectors up to the same maximum number of components we can get from the traditional PCA and ICA methods. These produced individual subspaces for each run, and these projections are removed first before running the subsequent mPCASW procedure. Our results show how the orthogonality is maintained in the same data subspace but slightly higher dot products on average across different subspaces. Regardless of the window and overlap size, the orthogonality of the basis vectors maintains low, indicating that they are uncorrelated and independent from each other. Thus, this shows the robustness of this method on this key factor in the sliding-window approach. We also present exciting results compared to other methods, including wavelet transform, spectrogram, and ICA. We then applied this extended mPCASW method into our study on fMRI and compared the resulting signal coefficients in the brain voxels, especially in the avalanches of the IWBC, with the output ob-

tained from ICA that is widely being used in fMRI analysis. Based on these results, we demonstrate that our method can uncover transient changes in brain-wide activation patterns that may be a key feature of neural communication. Such results were not as pronounced when using ICA.

This paper will also show comparison analysis results from two brain regions implicated in a wide range of neurological disorders and brain states. For example, the insula region, which is part of the functional salience network, has shown some abnormalities in Alzheimer's Disease (AD) patients (Liu et al., 2018; Philippi et al., 2020). While in the thalamus area, studies have shown the importance of the thalamic activity during the slow-wave sleep state (non-REM or NREM) (de Andrés et al., 2011; Mak-Mccully et al., 2017). In (Gonzalez-Castillo et al., 2022), they found that the ultra-slow fluctuations in the fourth ventricle explained the increase in the global signals during the sleep duration. We are still investigating the meanings of these changes in terms of brain information movements across the brain during fMRI scanning; however, we believe these methods will help further understand how to correlate the high correlations in brain regions with the changes in the brain signal content. In addition, these visualization methods might also help identify timepoints at which avalanches occur.

4.2 Methodology

4.2.1 Extended Modified PCA for Sliding-Windows (mPCASW)

We applied the mPCASW method as described in (Mohd Khairi et al., 2019), also summarized in Algorithm 2. Generally, the mPCASW decomposition finds the basis vectors from a sliding-windowed dataset. First, we need to define the sliding windows we will use. The windows are defined according to the vector indices of the $N \times 1$ vectors, $\underline{\mathbf{x}}_i$; thus, the first window starts at index 1 and is N_{win} points long. The next window starts at index $N_{hop}+1$ and is also is N_{win} points long. This step proceeds until we have N_{total} windows. Each window, w starts at the index

$$N_{start,w} = 1 + (w-1)N_{hop} \quad w = 1, \ \ldots \ , N_{total} \tag{4.3}$$

and is N_{win} points long. Therefore, each window will end the index of

$$N_{end,w} = N_{start,w} + N_{win} - 1 \quad w = 1, \ \ldots \ , N_{total} \tag{4.4}$$

We define the $N \times N$ windowing matrix, $\widetilde{I}_w$, which contains an $N_{win} \times N_{win}$ identity matrix corresponding to window w as in the Equation 4.5 below. The upper left corner of the identity matrix is at row $N_{start,w}$ and column $N_{start,w}$.

$$\widetilde{I}_w = \begin{bmatrix} 0 & 0 & 0 & 0 \\ 0 & I & 0 & 0 \\ 0 & 0 & 0 & 0 \\ 0 & 0 & 0 & 0 \end{bmatrix} \tag{4.5}$$

$$= \begin{array}{c} \\ N_{start,w} \\ \\ \\ \\ N_{end,w} \\ \\ \end{array} \begin{array}{c} \begin{array}{ccccccc} N_{start,w} & & & & N_{end,w} & & 0 \end{array} \\ \begin{bmatrix} 0 & 0 & 0 & 0 & 0 & 0 & 0 \\ 0 & 1 & 0 & 0 & 0 & 0 & 0 \\ 0 & 0 & 1 & 0 & 0 & 0 & 0 \\ 0 & 0 & 0 & \ddots & 0 & 0 & 0 \\ 0 & 0 & 0 & 0 & 1 & 0 & 0 \\ 0 & 0 & 0 & 0 & 0 & 0 & 0 \\ 0 & 0 & 0 & 0 & 0 & 0 & 0 \end{bmatrix} \end{array} \tag{4.6}$$

Multiplying $\widetilde{I}_w$ on the right by $\underline{\mathbf{x}}_i$ results in an $N \times 1$ vector that is all zeroes except for the portion of $\underline{\mathbf{x}}_i$ that is in window w.

We want to find the $N \times 1$ basis vectors that will be orthogonal to each other over the windowed sets of data. The first component, $\underline{c}_1$, has no constraint, so it is the same as in the regular PCA approach. That is to say that $\underline{c}_1$ is the eigenvector of K_{xx} associated with the largest eigenvalue. To find the next basis vector, $\underline{c}_2$, we must constrain the windowed portions of $\underline{c}_2$ to be orthogonal to the same windowed portions of $\underline{c}_1$.

Now, We define a matrix of all the windows from the $(i-1)^{th}$ basis vector:

$$W_{i-1} = \begin{bmatrix} c_{i-1}^T \widetilde{I}_1 \\ c_{i-1}^T \widetilde{I}_2 \\ c_{i-1}^T \widetilde{I}_3 \\ \vdots \\ c_{i-1}^T \widetilde{I}_{N_{total}} \end{bmatrix}. \tag{4.7}$$

From this we can form a matrix of all the windows from all the previous basis vectors, D_{i-1},

$$D_{i-1} = \begin{bmatrix} W_1 \\ W_2 \\ W_3 \\ \vdots \\ W_{i-1} \end{bmatrix}. \tag{4.8}$$

We now require $\underline{c}_2$ to satisfy the requirement that $D_1\underline{c}_2$ is a column vector of all zeroes, or we can use the equivalent equation below, which we generalize to the constraint on the i^{th} basis vector.

$$\underline{c}_i^T \left({D_{i-1}}^T D_{i-1} \right) \underline{c}_i = 0 \tag{4.9}$$

Starting with $\underline{c}_2$, we find $\underline{c}_i$ that maximizes $\underline{c}_i^T K_{xx} \underline{c}_i$ subject to the constraint above. One way to enforce this constrain is to find the eigenvalues and eigenvectors of $D_{i-1}^T D_{i-1}$. Some of the eigenvalues must be zero for the constraint to be satisfied, and we define the matrix V_i to be the $N \times L$ matrix whose column vectors are the L eigenvectors of $D_{i-1}^T D_{i-1}$ that correspond to the zero eigenvalues. Now we define

$$\underline{c}_i = \ V_i \ \underline{v}_i \tag{4.10}$$

which results in solving for $\underline{v}_i$ that maximizes $\underline{v}_i^T V_i^T K_{xx} V_i \underline{v}_i$ subject to the new constraint

$$\underline{v}_i^T V_i^T \left({D_{i-1}}^T D_{i-1} \right) V_i \ \underline{v}_i = 0 \tag{4.11}$$

and we find $\underline{c}_i$ from the defining equation above. It is possible to continue on this way until we reach $i = N_{hop} + 1$which results in $N_{hop} + 1$ basis vectors that maximize energy in a way related to that of PCA and are subject to the constraint that the windowed portions are orthogonal. The Appendix A shows the proof that the maximum number of basis vectors is $N_{hop} + 1$.

For most of our study (window variations analysis will be described in the next part), we used a window size of N_{win} = 20 timepoints and slid the window by N_{hop} = 4 timepoints. Therefore, from this method, 5 basis vectors can be obtained, and at each timepoint n, each signal set $x_i[n]$ would have 5 component values.

Because the method presented in (Mohd Khairi et al., 2019) only produced $N_{hop} + 1$ sets of components, we extended this method to obtain up to N_{win} components, which is equal to the maximum number of basis vectors that the original PCA or ICA would produce. The first $N_{hop} + 1$ components projection calculated from the mPCASW method were removed to create a new subspace of the signal, and the same mPCASW process was rerun using the new subspace to produce another $N_{hop} + 1$ components. We repeated this flow

until we reached a set of N_{win} components or basis vectors. These steps are summarized in Algorithm 3.

Algorithm 2 The mPCASW

$X \leftarrow$ original processed data
$i \leftarrow 1$ {Begin with first component}
$R \leftarrow XX^T$
$\underline{c}_i \leftarrow$ first basis vector of PCA(R)
for $i \leftarrow 2$ to $N_{hop}+1$ **do**
  for each window j **do**
    Create $\widetilde{I}_j$
  end for
  Create D_{i-1}
  $\underline{c}_i \leftarrow \underset{\underline{c}_i}{\operatorname{argmin}}\, \underline{c}_i^T \left({D_{i-1}}^T D_{i-1}\right) \underline{c}_i$
end for
$C \leftarrow [\underline{c}_1 \ldots \underline{c}_{N_{hop}+1}]$

Algorithm 3 The mPCASW with Extension

$s \leftarrow 1$ {Begin with first subspace }
$N_C \leftarrow 0$ {Total number of components}
$X_1 \leftarrow X$ {Original data to be processed}
while $N_C < N_{win}$ **do**
  $c_s \leftarrow mPCASW(X_s)$
  $\mathbf{C} \leftarrow [\mathbf{C}\ c_s]$ {Append new components into C}
  $P_s \leftarrow C(C^TC)C^T$ {Projection matrix for X_s}
  $s \leftarrow s+1$
  $X_s \leftarrow (I-P_s)X_1$
  $N_C \leftarrow N_C + N_{hop} + 1$ {Total components updated}
end while

In our case, we finally obtained 20 coefficient values for each timepoint. Using mPCASW for each subspace of data, each subspace's first component would typically produce the highest values due to Singular Value Decomposition (SVD) procedures that cause the basis vector with the highest eigenvalue to be the first component. Therefore, we rearranged our results to have the first components from each subspace to be the first five components in order, the second components from each subspace be the second five components, and so on.

Why is this a better way to represent the fMRI signal content changes? First, because of its orthogonality and uncorrelatedness between the basis vectors, each window of signals is uncorrelated, and therefore we can compare the similarity(ies) between two consecutive windows with better measurements.

Decomposing the signal in a sliding window approach provides a continuity of the resulting components from the window frames across the whole data. While traditional PCA and many other techniques are typically applied to windowed data separately from each window, the mPCASW method involves a portion of the previous window into the current window decomposition calculation.

Another advantage of this method is that each timepoint has its own set of components that can also be separated into sliding windows without jeopardizing the basis vectors' orthogonality. As implemented in (Badeau et al., 2004) and (Clement et al., 2014), these other methods produced a set of basis vectors for each window, thus resulting in multiple component values in the same timepoint. In other words, each timepoint has its component values from different sets of sliding windows.

4.2.2 Measuring Performance of Sliding-window Algorithm

Hindriks et al. (Hindriks et al., 2016) presented an analysis on the performance of sliding-window correlations in the functional connectivity in the brain fMRI. They observed the effect in detection probability when the window length and overlap time are varied. Drawing upon these variabilities in the paper, we showed the robustness of our sliding-window algorithm on two different settings of the data:

1. *window size,* N_{win}*:* We varied the size of the windowed data from 5 timepoints to 60 timepoints per window to measure the dependence of the window size in the orthogonality of the basis vectors.

2. *overlapping timepoints,* N_{hop}*:* For each window size, we hopped to the next window by N_{hop} = 2, 4, 6, and 8 timepoints. In each case, each two pair of windows shared the same signal from N_{hop} timepoints.

To compare the resulting output with other methods, we processed the same dataset using the wavelet transform function (MATLAB function, *cwt()*) and spectrogram (MATLAB function, *spectrogram()*). As a one-to-one comparison, we run two other methods - the regular PCA and ICA with the data being windowed like in the mPCASW. The data was sliding-windowed in the same N_{win} and N_{hop} like used for running the mPCASW algorithm, and each window was run through the regular PCA and ICA methods separately, producing an individual set of basis vectors for each window. The regular PCA used the *svd()* function in MATLAB, while the ICA decomposition is done using the widely available ICA program for fMRI analysis, the Multivariate Exploratory Linear Optimized Decomposition into Independent Components (MELODIC), in the FSL library (https://fsl.fmrib.ox.ac.uk/fsl/fslwiki/MELODIC).

4.2.3 fMRI Data

4.2.3.1 Resting-state fMRI

For algorithm development and analysis, we used the preprocessed resting-state fMRI in HCP S1200 release (Glasser et al., 2013) for our study analysis. The subjects in this release were drawn from a population of adults between 22 to 35 years old. Each preprocessed fMRI was aligned to the MNI152 standard space scan and has the size of 109 $\times$ 91 $\times$ 91 voxels with an isotropic voxel size of 2 mm $\times$ 2 mm $\times$ 2 mm acquired in 72 slices. The repetition time (TR) and echo time (TE) for the scans are 720 ms and 33 ms. A more detailed

description of the subjects can be found in (Glasser et al., 2013). In our study, we analyzed 53 subjects randomly drawn from the group.

4.2.3.2 Sleep fMRI

As a clinical application of this approach, we applied the mPCASW method to a set of sleep BOLD fMRI data. Long (about 24.5 minutes) fMRI scans were collected while subjects were rested with their eyes closed and naturally fell asleep. EEG was acquired simultaneously to verify sleep onset using a 32-channel MR-compatible system (BrainAmps MR, Brain Products GmbH), sampled at 5 kHz. Each scan was acquired with an isotropic voxel size of 3 mm $\times$ 3 mm $\times$ 3 mm, with a TR of 2100 ms, slice gap = 1 mm, and 30 axial slices. The images were aligned to MNI152 standard space into a resolution of 91 $\times$ 109 $\times$ 91 voxels. Further details about the acquisition and preprocessing of this dataset can be found in (Goodale et al., 2021).

4.2.4 Preprocessing

The HCP preprocessed data from 53 subjects were further preprocessed using FSL (https://fsl.fmrib.ox.ac.uk/fsl/) (Jenkinson et al., 2012). They were first spatially filtered using the Full Width Half Maximum (FWHM) kernel size of 6mm and then temporally smoothed with a bandpass filter (0.01–0.1 Hz) and linearly detrended. Due to the bandpass filtering used in the temporal smoothing, we removed the first and last 100 timepoints data instead of the original 1200 timepoints from the whole scan set, resulting in 1000 timepoints.

The sleep fMRI data from 3 subjects were also spatially and temporally smoothed with the same method applied to the HCP data.

4.2.5 Coefficient Values and Instantaneous Whole Brain Correlation (IWBC)

To study the changes in the signal content across the time windows, each window's coefficient values for each voxel were calculated by multiplying the basis vectors with the original signal data as shown in Equation 4.12. As a result, every voxel would have a set of coefficient values based on the number of basis vectors at each window. For N_{win} = 20 and N_{hop} = 4, each voxel in each time window frame will consist of 20 coefficient values. These computations were done using components obtained by mPCASW as well as the ICA.

$$\beta_i[w] = c_i[w]^T X[w] \tag{4.12}$$

To analyze the changes of β throughout the windows, we used the standard deviation volume, SDV, as described in (Mohd Khairi et al., 2019). An SDV is a measure of variability of the coefficients which finds the 'energy' of the standard deviations, that can be represented by the formula below,

$$SDV[w] = \prod_{i}^{max_c} std(\beta_i[w]) \tag{4.13}$$

The avalanche type used in our analysis, IWBC, is described in (Mohd Khairi et al., 2019) that will represent "the sum of positive correlation value of the dataset." The peaks in the IWBC plot will be used to analyze the changes in the signal content of a dataset. An example of an IWBC plot for a single subject is shown in Figure 4.1. Our analysis focuses on the IWBC avalanches, where the peaks are in the figure. The peak at time 559.44 seconds (timepoint 777 in the dataset), in this example, has the highest point in the plot, which corresponds to the highest total positive correlation values across the data.

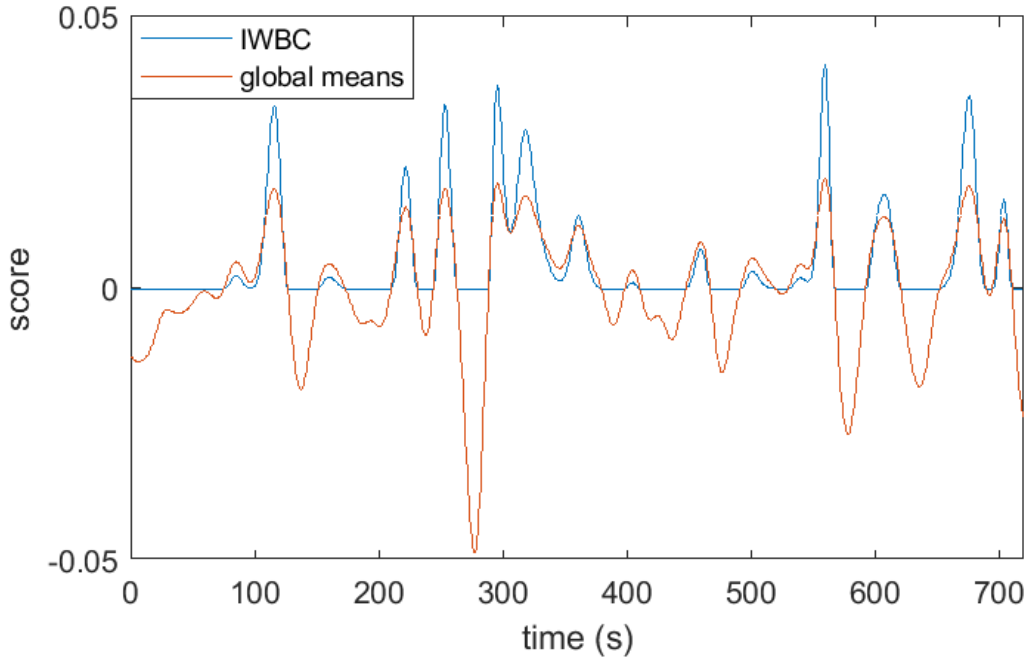

Figure 4.1: The IWBC and global means plots of a single subject. The IWBC is scaled to 10^2 to show the patterns and peaks clearly.

4.2.6 fMRI Analysis

We divided our analysis into two parts. The first part explored the changes in fMRI data coefficients in a human brain as a whole, where we explored the changes in all brain voxels in both resting-state and the sleep data. The second part of the analysis is based on the brain's structural regions, particularly in the thalamus and the insula regions. There are several interesting findings related to these regions during the resting-state and sleeping state (Cauda et al., 2011). Therefore, we would like to examine the signal changes in the same regions using the mPCASW algorithm and observe any exciting observations that can be extracted. For both regions, we extracted the voxels from the MNI probabilistic atlas from the McConnell Brain Imaging Centre

(Collins et al., 1995).

4.3 Results and Discussions

4.3.1 Basis Vectors of the Extended mPCASW

In the standard PCA, the resulting basis vectors are all orthogonal to each other. In the proposed mPCASW, the windowed portions within the same subspace are orthogonal to each other, but what about the full-length basis vectors? Orthogonality of the windows' basis vectors suggests the overall vectors may be close to orthogonal. The results in (Mohd Khairi et al., 2019) shows that in both cases – whether the basis vectors are cut into windows or they are taken as a whole, the orthogonality maintains across time.

As presented in (Mohd Khairi et al., 2019), the first subspace of mPCASW produced a closely orthogonal set of basis vectors where all the dot products between the basis vectors are very close to zero. However, by extending the mPCASW process to obtain more components, using more subspaces, the produced basis vectors do not maintain their orthogonality to each other across the different subspaces as the dot product between a pair of basis vectors from different subspaces can be as high as 10^{-1}. The dot product results in Figure 4.2(a) show that the near orthogonality of the basis vectors (the green regions in the diagonal) is maintained within a subspace, but not so much across subspaces.

Comparing the dot products between the basis vectors yielded by our method and the regular fastICA, we observed that the orthogonality is slightly close to mPCASW but still higher than what we observed in mMPCASW results. In Figure 4.2(b), the 5×5 small figure shows that the dot products are generally to the power of 10^{-1} compared to 10^{-8} in mPCASW in the first subspace. If we include the 20 components (Figure 4.2(b) top), the maximum dot products using fastICA maintain in the range of 10^{-1}. However, we cannot guarantee the orthogonality of the basis vectors in ICA, unlike PCA as we see in mPCASW within one subspace. Additionally, ICA has no guarantee of orthogonality over the windows, as shown in Figure 4.2(c), where the range of the dot products is far from the mPCASW dot products in the first subspace.

4.3.2 Effect of Different Window Settings

As explained in (Mohd Khairi et al., 2019), different window sizes and numbers of overlapping timepoint settings produce different results in terms of orthogonality and the mean of the component values. These settings also reflect how the data from previous windows is different from the current window, depending on how many timepoints are incorporated into a single window. We obtained similar results as we extend the original mPCASW to include more components as shown in Figure 4.3. Our robust method can be applied in most window sizes and the number of overlapping timepoints. Although we would like to have the window be as small as possible in many cases, the transitions from one window to another can be observed. However,

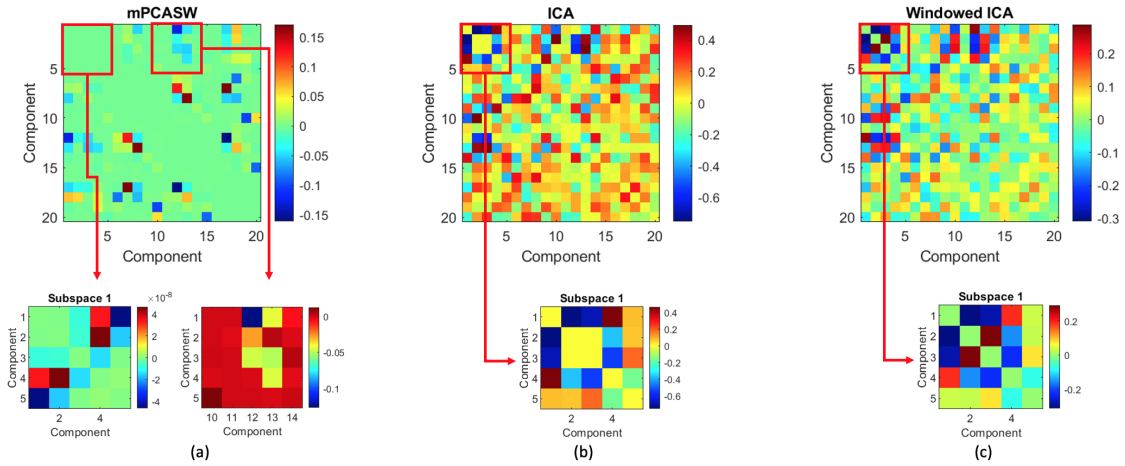

Figure 4.2: The dot products of all the basis vectors decomposed from a single subject derived from the (a) mPCASW approach, (b) ICA approach, and (c) ICA approach on sliding-windowed data. For results that use sliding-window data ((a) and (c)), the windows are set to have $N_{win} = 20$ and $N_{hop} = 4$. (a) Using mPCASW, the orthogonality maintains within a subspace with tiny dot products (bottom left) but can go up to 10^{-2} when the basis vectors are from different subspaces (bottom right). (b) When fastICA was applied to the data without windowing, the maximum dot products are closer to mPCASW with up to 10^{-1}. However, in a small subspace of the ICA, mPCASW shows higher orthogonalities between the basis vectors. (c) As sliding window setting was applied to the fastICA components, the overall dot product range stays close to the regular data setting (without windowing) with slightly lower values. Similar to (b), the subspace's dot products show higher values than the mPCASW method in the first subspace.

at the same time, we want to preserve the 'connectedness' characteristic of our results. Therefore, we choose the settings mentioned in the previous section to use $N_{win} = 20$ (14.4 seconds window) and $N_{hop} = 4$ (2.88 seconds jump to the next window) would be reasonable to observe important changes in a human brain.

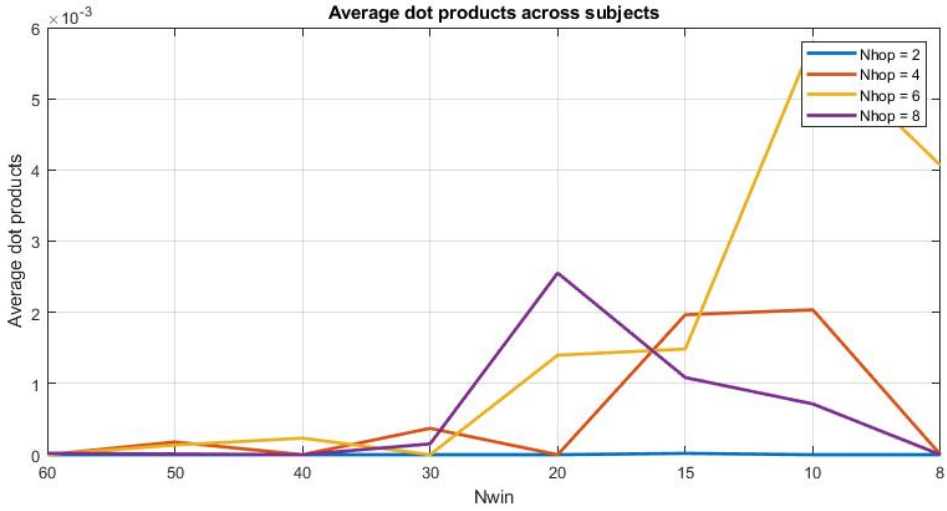

Figure 4.3: Dot product variations using different window length and number of overlapping timepoints.

4.3.3 Changes in rsfMRI Signal Content Detected With mPCASW

We observed comparisons between the resulting coefficients with the results from data processed using spectrogram, wavelet transform, and the ICA. In Figure 4.4, the continuous wavelet transform (CWT) scalogram (second plot) shows some changes in multiple frequency levels as the global means, μ reach most of the tall peaks. However, it is hard to determine the specific time or window where the frequency changes occur, especially when multiple peaks are close to each other. Similar to the spectrogram graph (third plot), the changes are observable at the global mean peaks, particularly close to the 300 seconds. However, some of the large peaks are not captured clearly, and the frequencies are not changed in any case. On the contrary, if we observe the mPCASW signal coefficients in the same manner, we can see changes clearly in windows around the peaks even when they are divided into different components at the same window.

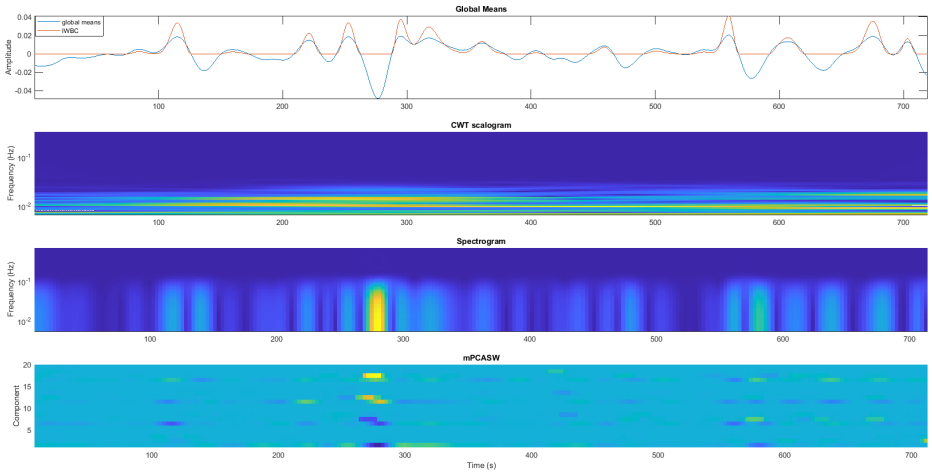

Figure 4.4: Changes in the signal content on the global means of a set of data. We can see more compact changes separated in various components using mPCASW whereas spectrogram and the wavelet transform show distributed changes based on the frequency and time-scale that cannot be seen in a specific timepoint.

Another way to analyze the changes of the signal coefficients is that we calculated the standard deviation volume (SDV) as shown in Figure 4.5 for a single subject. We also show the average of SDVs across 9 windows that contain the top three of IWBC peaks from all subjects in Figure 4.6. Window 3-7 contain the IWBC peaks, and window 5 is where the peaks' timepoints are in the middle of the window. Most of the SDV went to the minimum along the IWBC tall peaks, reflecting the possible 'synchronization' of the voxels' coefficients to be high at the particular time. We can observe individual voxels' coefficients in Figure 4.7(a), where components 6 and 16, for instance, show most voxels went into the lowest and highest values when the global means reach the peak at window 193.

In terms of the coefficient values, the subsequent subspaces interestingly showed significant changes

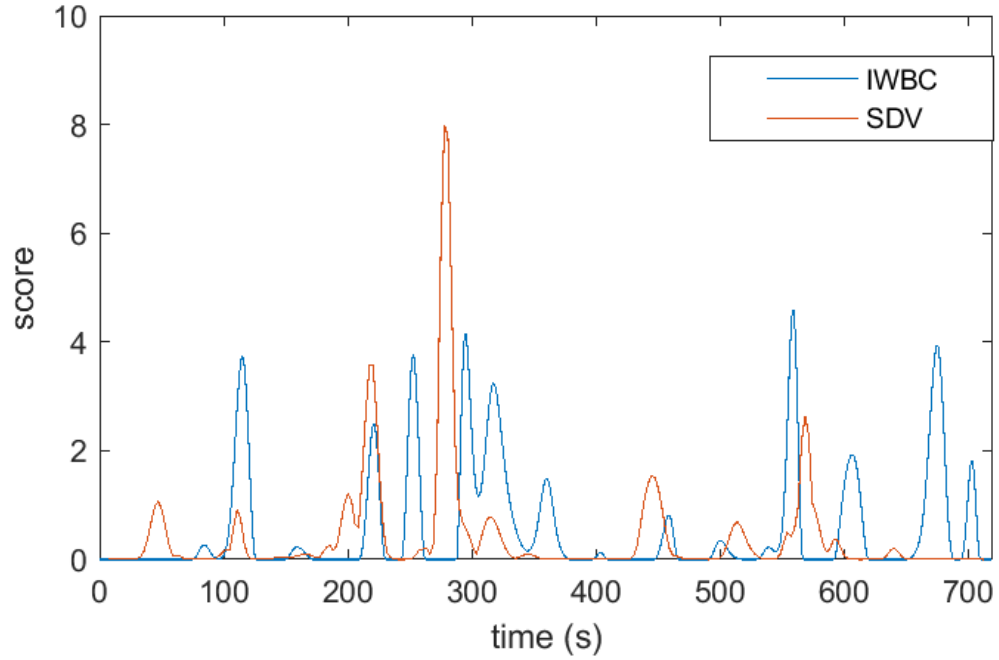

Figure 4.5: Statistics results for an HCP resting-state fMRI subject. Following the IWBC avalanches (blue), the SDV (red) dropped after most of high peaks of the avalanches occurred.

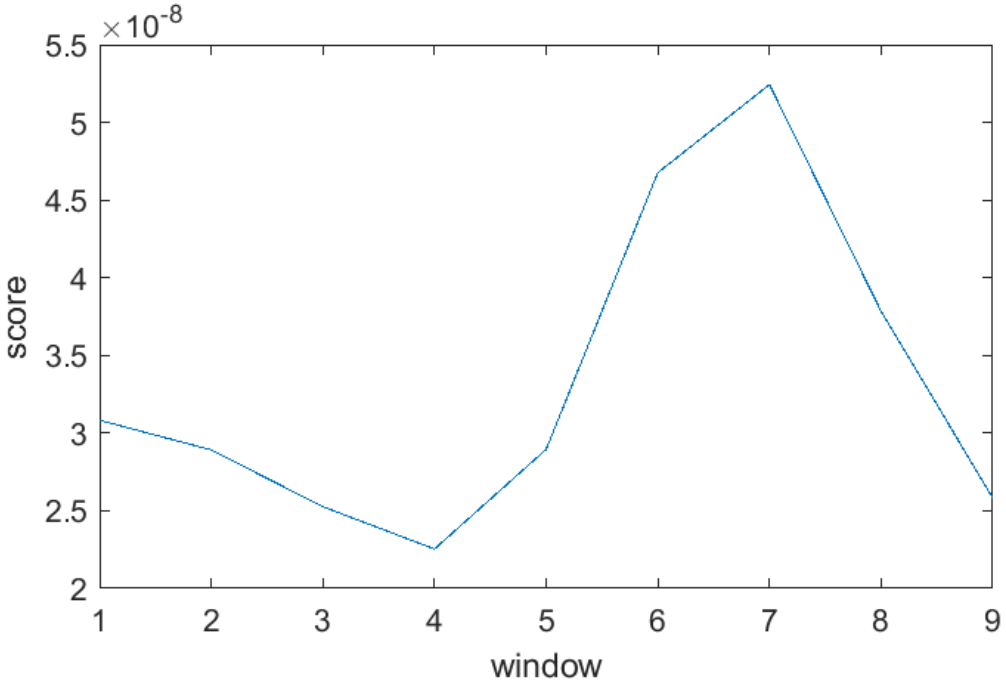

Figure 4.6: Average SDVs across 9 windows in 159 peaks occurred in 53 subjects' IWBC. On average, the lowest point appears at windows 3 and 4, where the peaks started to enter the windows. The SDV increased and dropped back after the peaks left the windows.

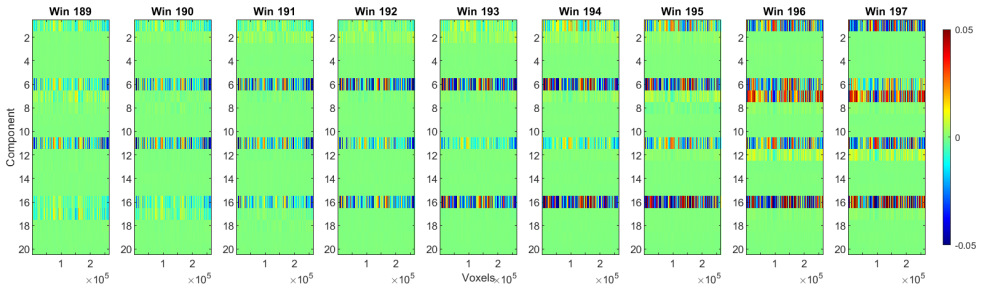

(a) mPCASW

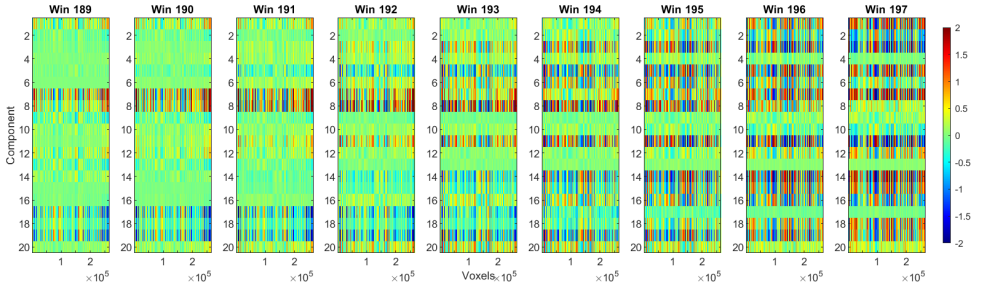

(b) ICA

Figure 4.7: Changes in the signal content in the whole brain across the time windows around the tallest peak of the IWBC of a single subject using (a) extended mPCASW and (b) ICA. Window 193 is the window where the highest point of the avalanche (timepoint 777 at 559.44 seconds of IWBC in Figure 4.1) occurs in the middle of the time window.

even after the first data subspace, which contains the data's highest eigenvalues, had been regressed out. For example, figure 4.7 shows changes for the highest point in the IWBC avalanche (Figure 4.1) occurred at timepoint 777 that appeared in windows 191 to 195 using mPCASW and ICA. As we can see in the result using mPCASW in Figure 4.7(a), as the tallest point of IWBC entered a window, most of the values of the coefficients began to change depending on the basis vector using both methods. The mPCASW results (Figure 4.7(a)) show that the sixth basis vector (sixth row in the figure) has the strongest coefficient changes than other earlier components. Most of the voxels' coefficient values increased in window 191 significantly and then slightly decreased back when the highest point in the avalanche was about to leave the time windows. In addition, the eleventh basis vector shows an evident change when most of the voxels' coefficient values decrease in windows 192 to 194 and increase again afterward. On the other hand, in the seventeenth basis vector, which comes from the fourth subspace of the data, we can still see small changes where most voxels' coefficient values approach zero as the timepoint 777 enters the windows. These observations provide us with some insight that even when after the biggest (earliest) subspace has been removed, more information can be extracted from the data.

ICA results also showed the same observations. However, the basis vectors' arrangement is different since

ICA components in MELODIC are ordered in their variance explained. The distribution is more dispersed and distributed than the mPCASW method that 'compresses' the data according to their importance (importance in PCA means the basis vectors are arranged based on their eigenvalues). In Figure 4.7(b), we can see significant changes when timepoint 777 began to enter and leave the windows in mutiple basis vectors. On the seventh component (seventh row of each window), the coefficient values on most of the voxels began to decrease until the peak reached the middle of the window at window 193, and they increased again when the peak began to leave a window. The eighth component behaved the same pattern but in the opposite direction when all the voxels went to the negative values when the same timepoint 777 entered the windows and increased after window 193.

As a comparison, we also plotted the β in Figure 4.8 when the correlation is at the very minimum level, meaning that the global means are close to zero. Components 1, 6, 11, 13, and 16 present some changes; however, in most of the components, there are no significant signal changes that can be seen. These four component changes are also changing with smaller values (except in component 1) than the value changes at the large peaks, which could happen in several locations in the data.

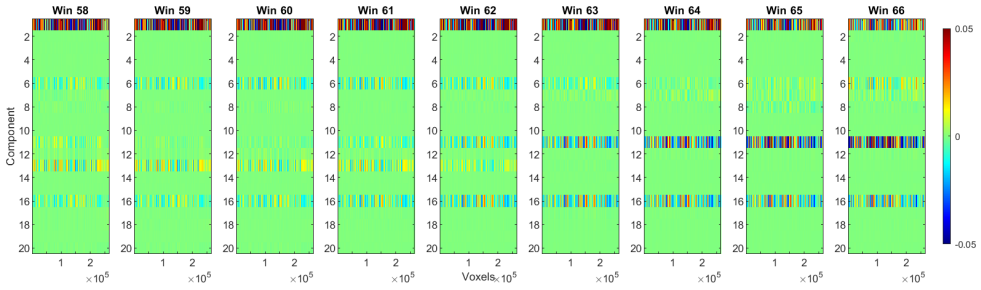

Figure 4.8: Changes in the signal content in the whole brain across the time windows that do not have high peaks (around timepoint 256 at 184.32 seconds) in the IWBC of a single subject using extended mPCASW. In these windows, no peaks or neighboring avalanches were happening.

We examined the coefficients by clustering the mPCASW output of a subject into several clusters using the k-means clustering method (MATLAB function used: *kmeans()*) with the settings of 20 clusters output. The observations were the voxels across the brain, while the features to be analyzed were the coefficients, β, concatenated across nine windows captured around a desired timepoint that we would like to observe. The clustering process was done separately for the peak around timepoint 777 (the highest IWBC point in Figure 4.4) and 256 (a zero IWBC point). As a result, the windows used for timepoint 777 and 256 in this clustering analysis are the same windows captured in Figure 4.7 and 4.8 respectively. We chose 20 clusters for our case to observe if there is a connection between the total number of components and clusters.

In Figure 4.9, we found clusters that contain similar behavior in the same component numbers. For example, in Figure 4.9(A), clusters 12 and 11 show high coefficient value changes across the window at

components 6 and 16. However, a slight difference can be seen between these components. Component 6 shows a high increase as the peak enters the window set, while component 11 shows a negative drop since the beginning of peak entrance to the windows before it went up after the peak left the windows. The low-coefficient clusters show the same but opposite behavior for component 6 and 16 in clusters 1 and 10. As the peak enters the window, we can see a sharp drop in the coefficient values in both components. Looking at the other components in all clusters, we can observe similar behaviors but lower change rates. The results for all clusters can be retrieved in the Appendix B.

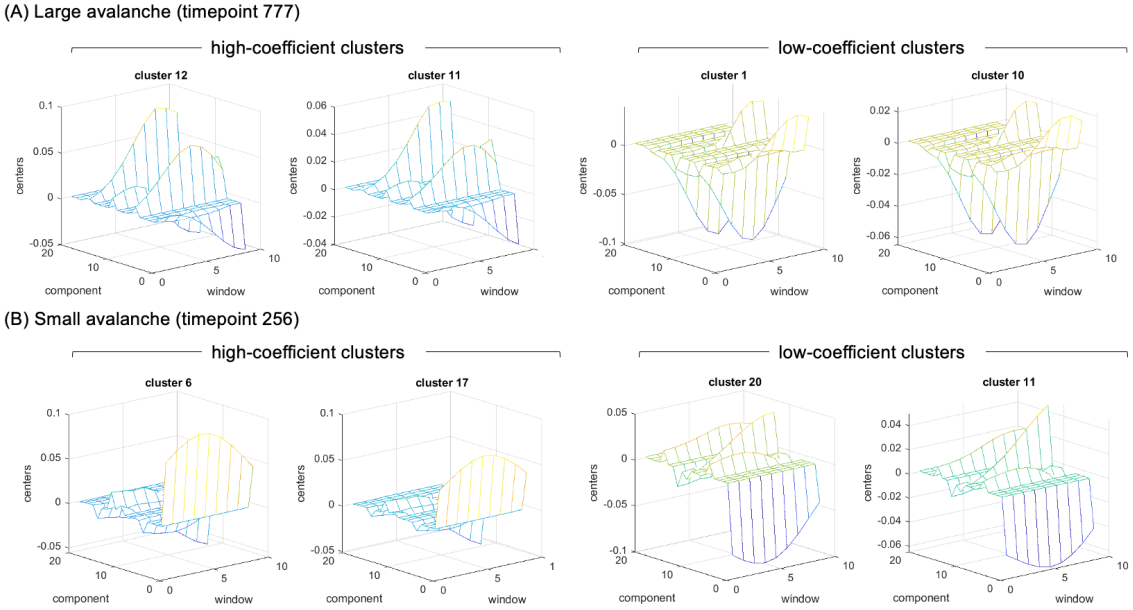

Figure 4.9: Clusters in each component across 9 windows in a single subject at (A) the highest IWBC peak (timepoint 777 at 559.44 seconds) and (B) a timepoint with no peak (timepoint 256 at 184.32 seconds). Results for all clusters in both timepoints can be retrieved in Appendix B. **(A)** At the highest IWBC peak (timepoint 777), cluster 12 and 11 show the highest coefficient centers, particularly in component 6 and 16. Clusters 1 and 10 show low-coefficient component centers, particularly in component 6 and 16. **(B)** For timepoint 256, where there is no huge IWBC avalanche, there are clusters that show significant changes in component coefficient centers, especially in components 1 in both high and low coefficient clusters.

Interestingly, using a tiny avalanche in the IWBC, we could still see the similar pattern changes around the peaks even the values are smaller than the big avalanches as shown in various clusters in Figure 4.9(B). As we have seen in various neuroimaging studies, brain activities are dynamic and change rapidly throughout the scan. Therefore, it is crucial not to exclude even small signals as there is a high chance that they might provide important information on what was happening inside a human brain. These observations prove that even a small change cannot be ignored during a signal analysis, especially in very dynamic brain activity.

4.3.4 Functional Content Changes in Insula Regions

We also observed the signal changes specifically in the insula and ventricles regions. Insula regions have shown some interesting changes when participants fell asleep and in Alzheimer's Disease (AD) patients as have been captured in (Liu et al., 2018; Philippi et al., 2020). Signals in the ventricles have been found to have significant changes during sleep as presented in (Gonzalez-Castillo et al., 2022) where they found that the ultra-slow fluctuations in the fourth ventricle could explained the increase in the global mean signals.

Looking at the results extracted from several sleeping subjects' fMRI, we observed some known regions, including the insula and ventricles regions. For example, in Figure 4.10, coefficients from component 1 showed up in a C-shaped region (box 1), covering mainly in the subject's insula area. A similar observation is captured in the ventricles region (box 2), which contains high coefficient values in most of its voxels. We can differentiate the sum of the transform coefficients between before and after a subject falls asleep as captured in multiple mPCASW components in the insula (Figure 4.11 (a)-(c)). In the subject that slept after 15 minutes during the scan (4.11 (b)), there are a few big avalanches in the insula before the subject fell asleep, giving us an indication that there could be an event happening in the insula compared to other regions.

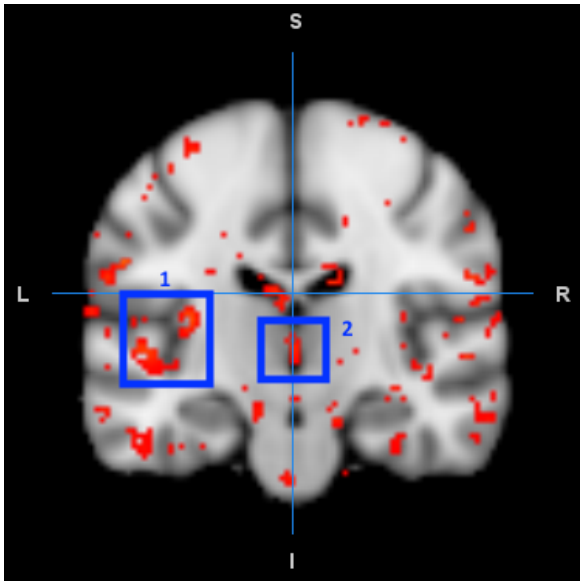

Figure 4.10: The transform coefficients of a sleep fMRI from component 1 at the highest peak of its IWBC.

4.4 Conclusion

We have proposed an extension of mPCASW method to obtain more components and basis vectors from the original algorithm in (Mohd Khairi et al., 2019). mPCASW results have shown that the resulting basis vectors have more independence and uncorrelatedness than ICA and other decomposition methods regardless of the window size and the overlapping time between windows. The resulting components have shown that

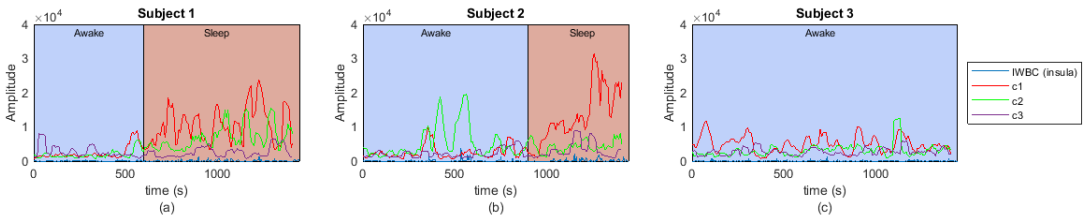

Figure 4.11: Total sleep transform coefficients, β in insula region voxels from component 1,2, and 3 for sleep fMRI that have slept after (a) 10 minutes, (b) 15 minutes, and (c) not sleeping at all during the scanning session.

the signal changes can be observed in a much more compact and connected way from one window to another instead of ICA, spectrogram, and scalogram. Thus, this helps us perhaps examine better what is happening in a dataset across time. We demonstrated how the decomposed signal changes in different sets of fMRI data, where we can see the changes in several components in either using the whole brain dataset or a region of a brain. Our method is not only to be utilized specific to neuroimaging data, but it can be useful to many other sets of dynamic and time-varying data containing multiple signals where decomposition methods are already widely used.

CHAPTER 5

Dynamic Temporal Propagation Patterns in Avalanches of fMRI

Spatial patterns across different brain regions have been identified widely during the resting state as well as task-related fluctuations of the brain. Recent findings have stated that these activities are not stationary but show temporal dynamic activities. We were interested in the various spatiotemporal dynamics across the resting-state functional magnetic resonance imaging (fMRI) blood oxygen level-dependent (BOLD) signals that are decomposed into a set of components showing different temporal patterns of signal transitions. As we observed the changes around the brain avalanches, defined as the magnitude of the whole-brain correlation across time, we found five major patterns that can be observed around the fMRI avalanches using the modified Principal Component Analysis for Sliding-Window (mPCASW) components. Sequential patterns across components' extremal curves of the functional network (FCN) show that several regions have clear time delays as avalanches reach the maximum point. The other components were found to diverge, converge, or both across the regions around the avalanches, reflecting possible synchronization of information happening during the avalanches. Within patterns, we found that several network regions, mainly the somatomotor (SMN) and dorsal attention (DAN) networks, exhibit the most evident pattern changes during signal transitions. These crucial findings reveal that BOLD signals could reveal more interpretations of the dynamics in the human brain, not just timing patterns of brain regions but also the possible synchronization and desynchronization happening during fMRI avalanches.

5.1 Introduction

For almost three decades, resting-state functional magnetic resonance imaging (rsfMRI) has become an important modality for learning dynamic brain activities, particularly in human brains. Different ways and types of studies have been done extensively to observe the changes in blood oxygen level-dependent (BOLD) signals temporally and spatially. One topic that has become of great interest is the evidence of temporal delays among regional fMRI signals. Earlier fMRI studies have shown that zero-lag temporal correlation functional connectivity (FC) can provide neurological interpretations for mapping the structural organization of brain function (Power et al., 2011; Yeo et al., 2011). However, many recent studies found that more interpretations can be made beyond zero-lag temporal correlation FC analysis.

As many have demonstrated that the correlation between brain regions evolves over time (de Pasquale et al., 2012; Chang and Glover, 2010; Kiviniemi et al., 2011; Allen et al., 2014; Hutchison et al., 2013b; Kucyi and Davis, 2014; Ponce-Alvarez et al., 2015), multiple studies have revealed that timing propagation in the

rsfMRI can be extracted into different sequential patterns within time-series scans of an individual. The infra-slow activity (<0.1 Hz) exhibits distinguished propagation patterns across the brain, revealing time delays between the regions on the order of 1 s (Matsui et al., 2016; Mitra et al., 2018; Raut et al., 2019). Furthermore, even with minor changes in FC, the propagation sequences are reproducible and consistent across the brain states (Mitra et al., 2015b,a, 2017, 2018). Similar results can also be produced when the rsfMRI dataset is combined with magnetoencephalography (MEG) and electroencephalography (EEG) datasets (Takeda et al., 2021).

Signal propagations in other than human brains also have shown similar observations. For example, studies have observed slow propagations of spontaneous brain activities in awake (Liu and Zhang, 2019) and dexmedetomidine-anesthetized mice (Majeed et al., 2011; Matsui et al., 2016; Mitra et al., 2018) from the low-frequency fMRI signals.

Going further into organizing these propagation findings, studies such as (Mitra et al., 2015b,a; Mitra and Raichle, 2016; Shine et al., 2017; Raut et al., 2020) provided reproducible organization of brain temporal propagation patterns. Several had organized the patterns in terms of fast and late response across intrinsic brain regions and suggested there exists internetwork after intranetwork communication processing within seconds (Veit et al., 2021).

Though not many have explored these sequential brain propagations as other discoveries until recently, we believe this is important in learning how information flows across brain regions through different networks for future learning and improvement. Moreover, these new discoveries in animal and human brains convey an important message: we can observe the neurological process from the blood oxygen level change in fMRI through static and dynamic signals analysis.

The primary goal of this study is to investigate the timing patterns across the brain's functional network, which are closely similar to what have been reported in (Mitra and Raichle, 2016; Shine et al., 2017; Bolt et al., 2022) as we decomposed into several components. Using the modified Principal Component Analysis for Sliding-Windows (mPCASW) (Mohd Khairi et al., 2019), each resulting component can be categorized into several common patterns that can be analyzed separately. In strictly connected sliding windows, we observe similar behavior across different subjects in the early and late regions through a subset of mPCASW component coefficients. In addition, we also found some synchronization and desynchronization behavior around the avalanche fMRI peaks as another subset of mPCASW component coefficients in separate brain regions converged and diverged around the brain avalanches. While the early and late patterns have been described in mentioned papers, the synchronized and desynchronized patterns have yet to be explored in more detail as in (Ponce-Alvarez et al., 2015). We believe that our findings here will provide an excellent, if not an essential, tool to analyze further the behavior of regions during the information transfer throughout the

brain.

5.2 Methodology

5.2.1 fMRI Data

For algorithm development and analysis, we used the preprocessed resting-state fMRI in HCP S1200 release (Glasser et al., 2013) for our study analysis. The subjects in this release were drawn from a population of adults between 22 to 35 years old. Each preprocessed fMRI was aligned to the MNI152 standard space scan and has the size of 109 $\times$ 91 $\times$ 91 voxels with an isotropic voxel size of 2 mm $\times$ 2 mm $\times$ 2 mm acquired in 72 slices. The scans are recorded with a repetition time (TR) and echo time (TE) of 720 ms and 33 ms. A more detailed description of the subjects can be found in (Glasser et al., 2013). In our study, we analyzed 53 subjects randomly drawn from the group.

The HCP preprocessed data were further preprocessed using FSL (https://fsl.fmrib.ox.ac.uk/fsl/) (Jenkinson et al., 2012). They were first spatially filtered using the Full-Width Half Maximum (FWHM) kernel size of 6mm and then temporally smoothed with a bandpass filter (0.01–0.1 Hz) and linearly detrended. Due to the bandpass filtering used in the temporal smoothing, we removed the first and last 100 timepoints data instead of the original 1200 timepoints from the whole scan set, resulting in 1000 timepoints.

5.2.2 mPCASW Components and Instantaneous Whole Brain Correlation (IWBC)

To study the changes in the signal content across the time windows, we set the preprocessed individual fMRI data, X, in time $\times$ voxel 2D space. We then applied the extended mPCASW method described in Chapter 4 with the setting of window size N_{win} = 20 and sliding point N_{hop} = 4 to the the data X. The resulting components' basis vectors stored in C, where each column represents a component's basis vector in each time, are then projected into the original data X, by each sliding window, to obtain the transform coefficient values, β (Equation 5.1). As a result, every voxel would have a set of coefficient values based on the number of basis vectors obtained from the mPCASW at each window. In our study, each voxel at each time-window frame consists of 20 β values.

$$\beta_i[w] = c_i[w]^T X[w] \tag{5.1}$$

The avalanche type used in our analysis, IWBC, is described in (Mohd Khairi et al., 2019) that will represent "the sum of positive correlation value of the dataset." The peaks in the IWBC plot will be used to analyze the changes in the signal content of a dataset. An example of an IWBC plot for a single subject is shown in Figure 5.1. Our analysis focuses on the IWBC avalanches, where the peaks are in the figure. In

this example, the peak at time 559.44 seconds (timepoint 777 in the dataset) has the highest point in the plot, which corresponds to the highest total positive correlation values across the data.

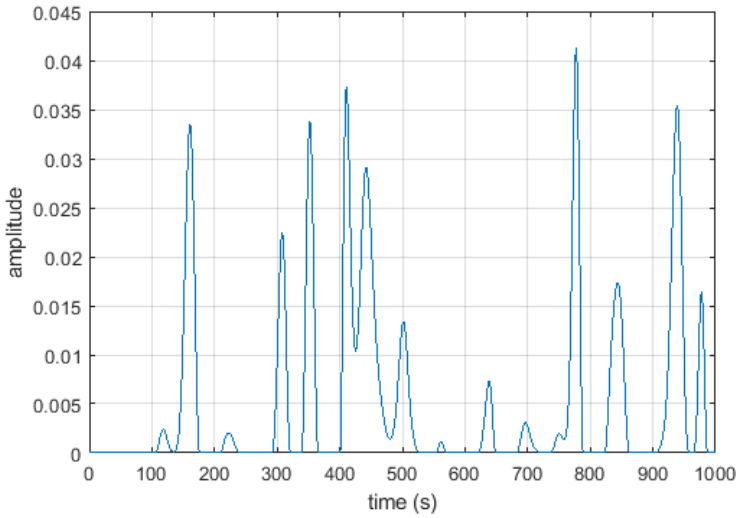

Figure 5.1: The IWBC plot of a single subject.

5.2.3 mPCASW Component Classifications

The β values were then extracted into network regions using the 7-Network regions (Yeo et al., 2011) producing separate β for each region in every mPCASW component (Figure 5.2). The transform coefficient β from the voxels in each region were averaged at each window, resulting in a vector of time-series β for an individual network region specified.

We selected the top three secluded IWBC peaks from each subject and analyzed the components coefficients within 9 windows around these IWBC peaks. The secluded peaks are defined as the IWBC avalanches that do not have any neighboring local maxima in the distance of 15 timepoints (10.8 seconds), large enough to cover sliding 20-timepoint window. We used the MATLAB (http://mathworks.com) function *findpeaks()* with the option *'MinPeakDistance'* to select the peaks automatically. 9-time windows here include 5 windows containing the tip of the selected peaks, plus two windows before and two after the main windows (Figure 5.3). Since we have 53 subjects, 159 IWBC peaks were analyzed in each of their set of components and network regions in our study.

As we have 20 components in our analysis setting, the 9-window component coefficients are categorized into five distinct patterns where the examples of each pattern can be referred in Figure 5.2 and listed in the parentheses:

1. extremal curve (EC): This β curve contains either a local maximum or minimum value within the

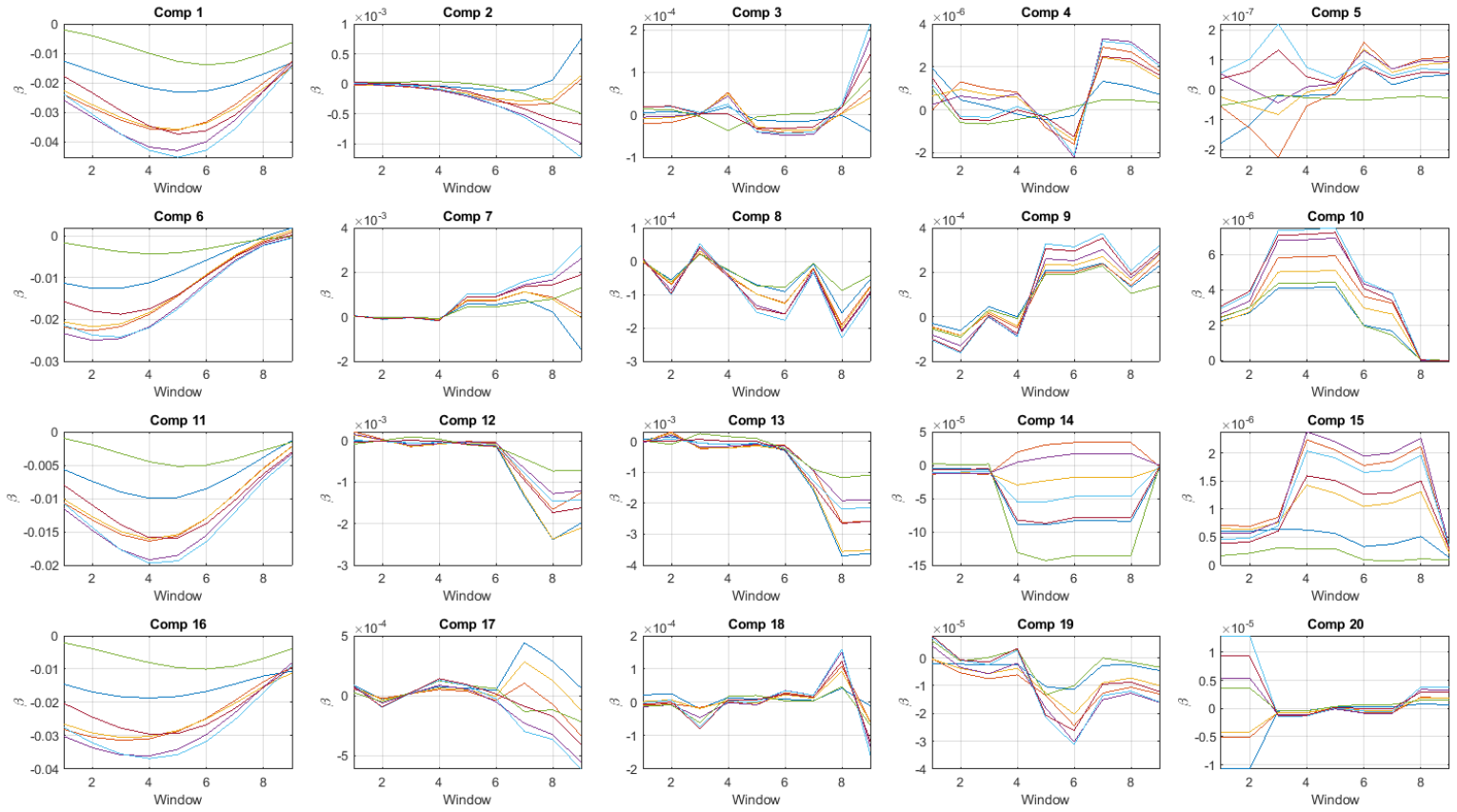

Figure 5.2: 20 component coefficients extracted using modified Principal Component Analysis for Sliding Window (mPCASW) for 9 windows across an IWBC peak in the 7-network regions from Yeo's atlas (Yeo et al., 2011). Five different major patterns can be categorized: (1) extremal curve (EC), (2) diverging (DV), (3) converging (CV), (4) diverging-converging (DC), and (5) converging-diverging (CD) patterns. In this β set, we can classify components 1, 6, 11, and 16 as EC; 2, 3, 7, 12, 13, 17, and 19 as DV; 5 as CV; 10, 14 and 15 as DC; and 20 as CD.

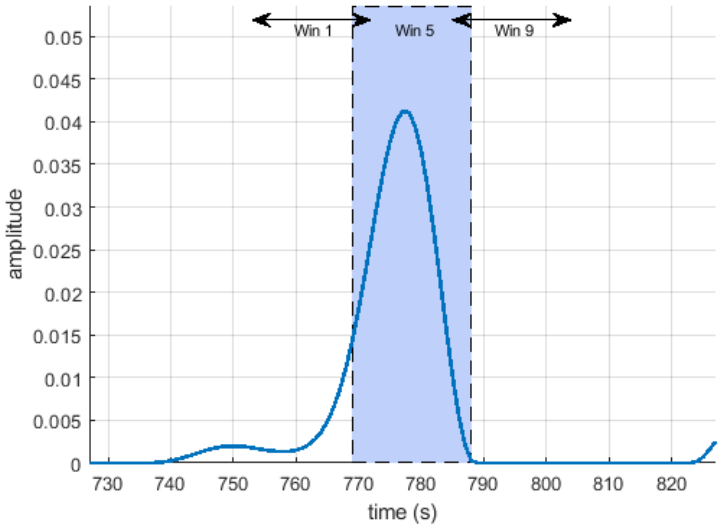

Figure 5.3: An example of a 9-window set around an IWBC peak. Windows 3-7 contain the tip of the IWBC peak, with the tip at the center of window 5.

9-window frame (components 1, 6, 11, and 16),

2. diverging (DV): the β values from the networks begin very close before, and they begin to deviate from each other at a later window (components 2, 3, 7, 12, 13, 17, and 19),

3. converging (CV): this β set has the opposite pattern than DV, where they a large standard deviation at the beginning and becomes smaller at a later window (component 5),

4. diverging-converging (DC): the β in this set has large standard deviations in the center windows and tiny in other windows (components 10, 14, and 15), and

5. converging-diverging (CD): the β in this set has small standard deviations in the center windows and large in other windows (component 20).

A small subset of components that cannot be categorized in any of these pattern clusters are excluded in this analysis to focus on the timing propagation observations in the majority of the components. From a total of 3180 components (53 subjects $\times$ 3 tallest IWBC peaks $\times$ 20 components), only about 10% of the components are removed from this analysis, which include the component β that do not show any distinct pattern, have multiple extremas, and multiple CD and DC pattern within the 9-window range (Figure 5.4).

5.2.4 Timing Pattern Sequence

In order to find the timing pattern sequence, the EC β sets are used. Components that contain multiple extrema are removed to ensure clarity of analysis. The time ordering for each selected component is measured when

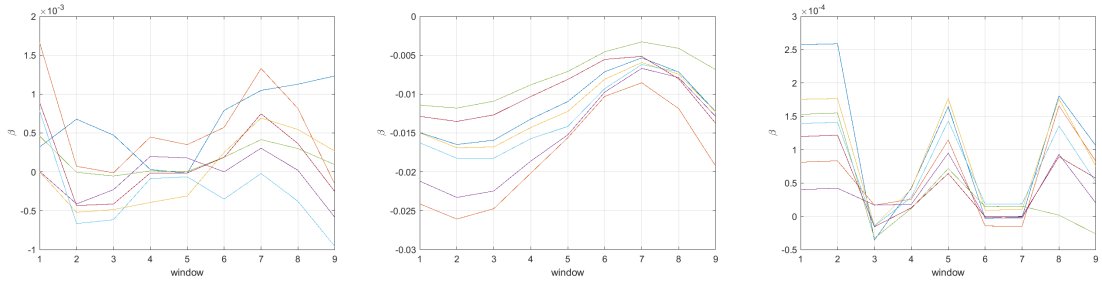

(a) No pattern (b) Multiple extremas (c) Multiple CD/DC

Figure 5.4: Examples of components coefficients that are excluded from the analysis are the components that (a) do not have any distinct pattern, i.e, minimal changes in the coefficient values, (b) have more than one local minimum or maximum, and (c) have multiple CD or DC patterns, within the 9-window range around its IWBC peak.

each network curve reaches the local minimum or maximum. Regions that reach their EC peaks' extreme at the same time would be counted as the same time sequence numbering. For example, in Figure 5.2, 3 regions (highlighted in yellow, red, and purple) reached the local minimum first at the same window, followed the other three regions in window 3, and one region at window 4. Therefore there are only 3 sequence numbers in this component. Because of this counting method, the maximum sequence number in our dataset reached to only 6, and not 9 like the total number of windows that we are analyzing.

5.2.5 Clustering of Sequential Timing Patterns

We clustered the EC patterns obtained in Section 5.2.4 into clusters of similar time-lag patterns using *kmeans()* in MATLAB with the setting of $k = 6$. Several cluster settings have been tested, and we found that six clusters provide the best separation of different sequence patterns.

5.2.6 Other Patterns Analysis

For DV, CV, DC, and CD patterns, we looked into the time when the divergence and convergence happen in each component based on the standard deviation of β between M network regions in each window, σ. The divergence and convergence can be defined when there is a significant change in the standard deviation of one window j with the previous window i (Equation 5.2):

$$\delta_{\sigma}(i,j) = \frac{\sigma_{\underline{\beta}_j} - \sigma_{\underline{\beta}_i}}{\sigma_{\underline{\beta}_j}} \times 100 \tag{5.2}$$

We also looked into which network region has large changes compared to the other network by computing the changes in β from one window to another in each region r:

$$\delta_{\beta}(r,i,j) = \frac{\beta_{r,j} - \beta_{r,i}}{\beta_{r,i}} \times 100,$$
$$i,j = 1,\ldots,9, \textit{ and } r = 1,\ldots,M \tag{5.3}$$

5.3 Results and Discussions

5.3.1 Temporal Ordering Across Functional Networks (FCN) in EC Component Pattern

To show the reproducibility of this type of pattern, we analyzed the EC components separately in positive and negative EC, as well as a combination of all EC components. In general, most somatomotor (SMN), dorsal attention (DAN), and salience ventral attention (SVN) networks reach the highest point of the components earlier compared to other four regions as they reach the highest point around the mid-window at window 5 (Figure 5.5 top). However, while DAN mainly reaches peaks at the same window as the IWBC avalanches, the other regions are largely distributed around three central windows with an almost equal number of occurrences. The curves roughly follow the avalanche peaks where the highest points are in the center at window 5 (0 window distance), where only a few components have EC peaks very early or late than the IWBC avalanches.

Looking into the sequence on which region goes to the peak first (Figure 5.5 bottom), SMN tends to reach the peak first 60% of the time, while SVN also has a high count to reach its peak early. Limbic network shows up high later most of the time compared to other networks, as about 30% of the EC components reach the highest point after two or three networks reach their peaks. On the contrary, visual networks tend to spread out in the timing sequence, indicating no apparent timing preference in this network. Overall, we observed that the SMN will lead the β change in the EC components followed by the visual network and ends around the areas that include the limbic and DAN regions (Figure 5.6).

5.3.2 Clusters of Different Timing Patterns

Clustering the EC components into several clusters, we can observe several groups of different time-lag sequences. With window 5 as the central window where an IWBC peak is at the center, these EC peaks are measured by how many windows are present ahead or later than the IWBC peaks. In all cases, whether positive or negative EC components, we can categorize the clusters from 'very early' to 'very late' depending on when the EC peaks from most regions reach their extreme points. Big clusters of components tend to have all network regions be very close to the central window (blue and green shades), which means the EC peaks in these clusters are either on or earlier than their respective IWBC peaks (Figure 5.7). Although in a smaller cluster, we also observed some components change differently in the 7 networks. A clear observation can be seen on the second cluster in Figure 5.7c, where three networks - Visual, DAN, and SVN networks tend to

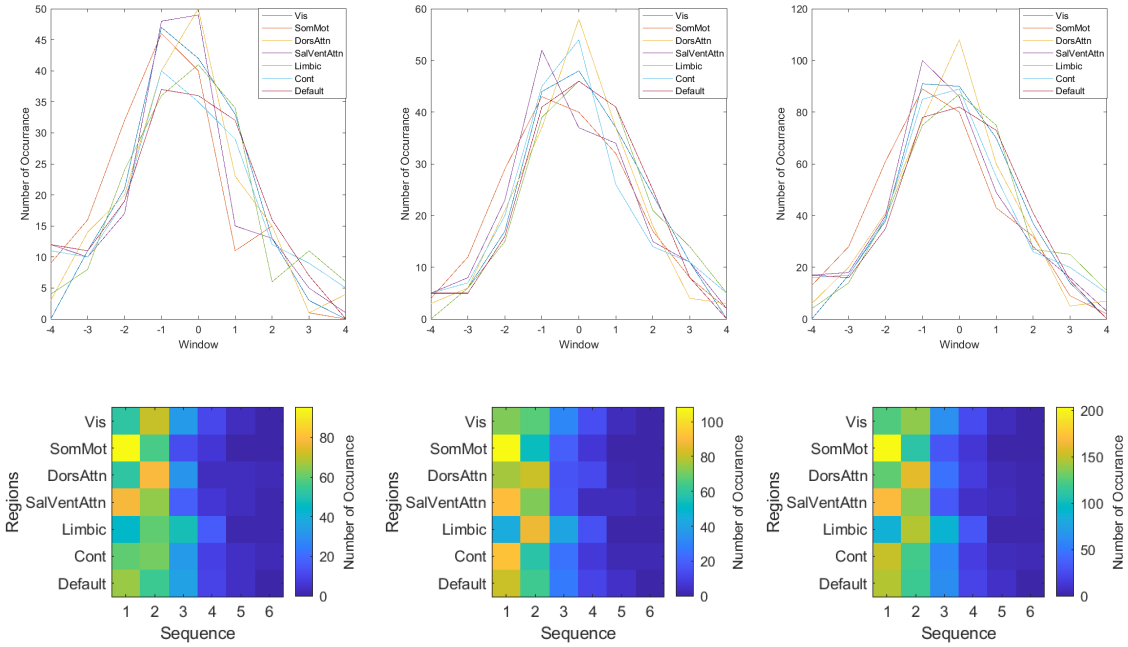

(a) Positive EC (b) Negative EC (c) All EC

Figure 5.5: The region timing sequence in EC peaks. (top) In all three cases (positive, negative, and combined EC components), the curves for all regions generally follow the IWBC avalanches curves. Several distinguished regions can be seen to have a clear sequence, such as the dorsal attention network (DAN), which shows a high probability of having an EC component peak at the same window as the IWBC peaks. (bottom) In a regional sequence manner, 60% of the EC components show that SMN and SVN reach their peak early compared to other regions, while the limbic network tends to reach its peak later 30% of the time.

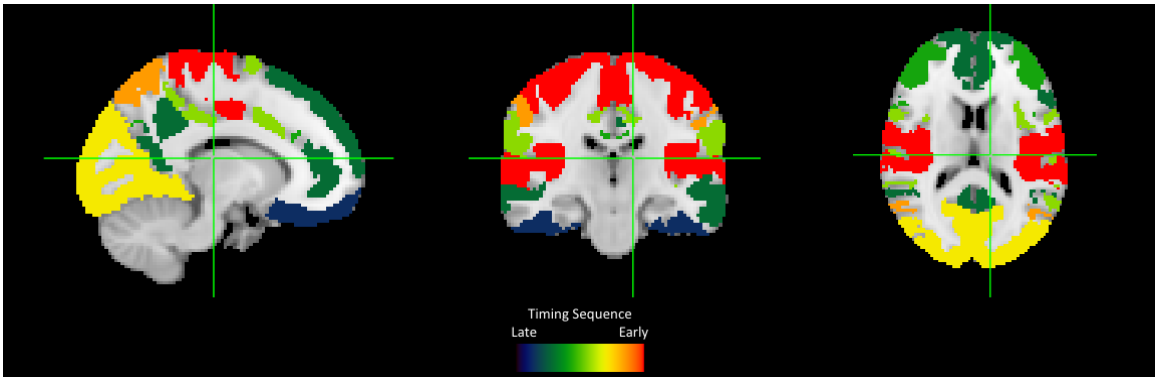

Figure 5.6: The timing sequence of each FCN based on the EC components. The somatomotor network typically strikes up first compared to other networks. The high β flows from the top of the brain to the visual network region and ends at the frontal lobe, where the dorsal attention and limbic networks are.

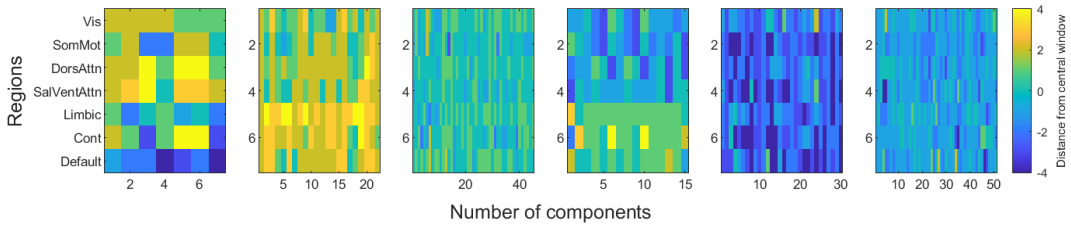

(a) Positive EC

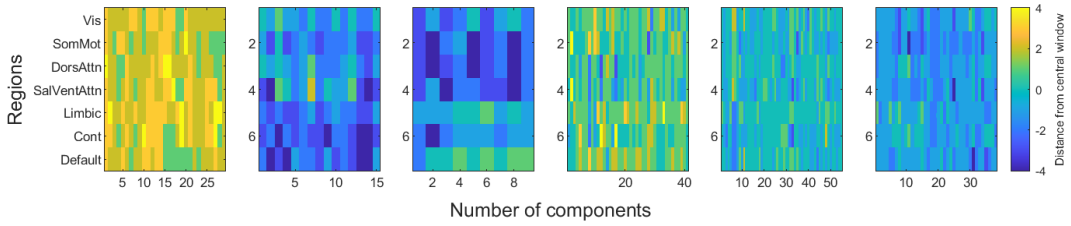

(b) Negative EC

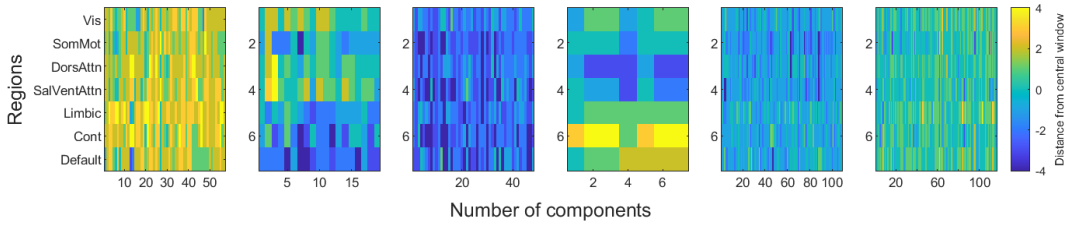

(c) All EC

Figure 5.7: The Extremal curves (EC) components clustered into six clusters according to the distance pattern from the central window 5 for (a) positive EC, (b) negative EC, and (c) combined positive and negative EC components. In all cases, the largest clusters appear to be the components that have EC peaks close to where the IWBC peaks are at the center, i.e., zero distance from window 5 (light green and light blue shades). The next large clusters are the groups of components where all regions reach the highest point a few windows earlier or later than the IWBC peak (dark blue and bright yellow shades). In a small number of cases, a small set of components show a distinct separation between the regions. For example, Visual, DAN, and SVN networks of the second cluster in (c) tend to reach the EC peaks later than the other four networks.

reach the EC peaks later than the other four networks. A minimal number of components, but more observable in the positive EC (Figure 5.7a), visual, SMN, DAN, and SVN networks typically reach their extreme points early compared to limbic, control, and DMN networks. Overall, about 12% of the EC components show later peaks, while another 12% show very early changes than the IWBC avalanches.

5.3.3 What About Other Patterns?

5.3.3.1 Converging (CV) and Diverging (DV) Coefficient Patterns

CV and DV patterns are observed when there is a significant single converging or diverging pattern within the 9 windows around an IWBC peak. On average, the DV components tend to diverge, either close to the center window (window 5) or when they leave the sliding windows. While in CV components, most converging behaviors happened as the IWBC peaks started to leave the windows, i.e., after window 5. Furthermore, both DV and CV β patterns have a significant median change around the peak when entering windows 5 and 6, showing that both divergence and convergence of β are primarily happening while the IWBC peaks are at the center of the window (Figure 5.8).

If we look into specific FCN regions, SMN and DAN networks show the largest β divergence around the IWBC peaks which happen right after the large avalanche peaks leave the windows (Figure 5.9a and 5.9c). The visual network shows large changes during the peak time, while the limbic network shows an early change, although they both have smaller changes than the other two networks. The other two networks, namely SVN and control networks, do not show much clear change in this propagation pattern.

In contrast, limbic has the largest change around the IWBC peaks in CV components (Figure 5.9b and 5.9d), particularly when the peaks are leaving the windows (window 6 to 7). While the control and SVN networks are not dominant in converging changes, DAN shows an early change, although not as large as the limbic network, followed by the SMN and DMN networks.

5.3.3.2 DC and CD Coefficient Patterns

The DC and CD component patterns are categorized when the network regions' coefficients diverge and converge within the 9 windows around the IWBC peak. As an example of mPCASW β results in a subject in Figure 5.2, components 10 and 14 can be classified as DC, while component 20 is classified as a CD component.

Across 652 IWBC avalanches' components that show a DC behavior, the largest change tends to happen during the divergence in the early windows, and lesser change happens during convergence as the avalanches left the 9-window set (Figure 5.10a and 5.10c). Most of the large β transitions happened as they jumped from windows 1 to 2 or the two subsequent windows, which means that the divergence happened before the

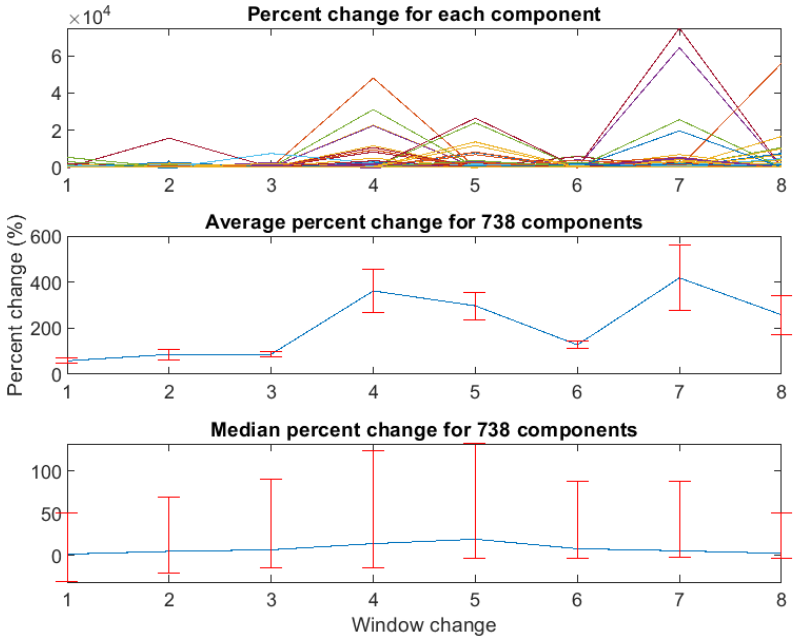

(a) Diverging Components

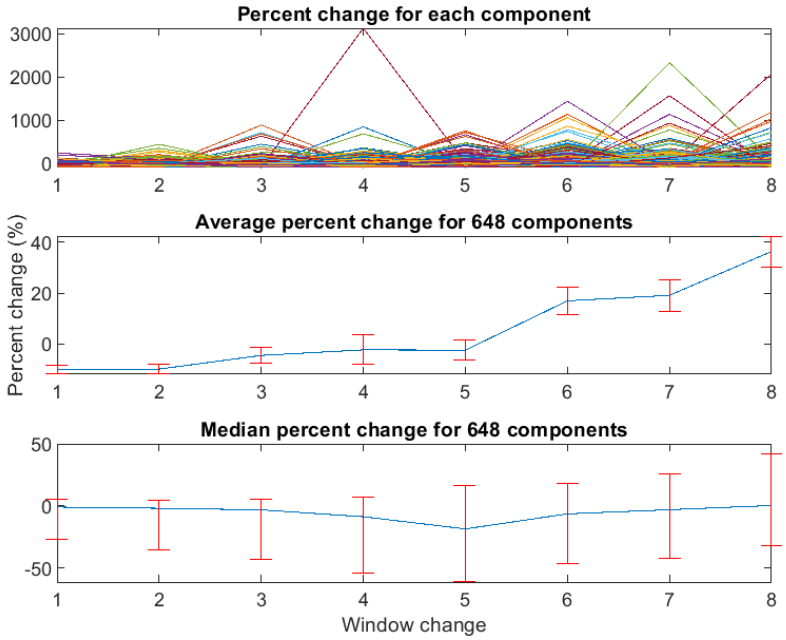

(b) Converging Components

Figure 5.8: The changes of β standard deviation in diverging (DV) and converging (CV) components across 9 windows around large IWBC peaks. The first plot of each pattern shows the individual component's percent change from the previous window, while the second and third plot the mean and median of the components' change with the error bars of the standard error (SE) and interquartile range (IQR), respectively. Some components show huge changes in several windows to more than 100%. However, the mean and median present the overall distribution across 738 and 648 DV and CV components, respectively.

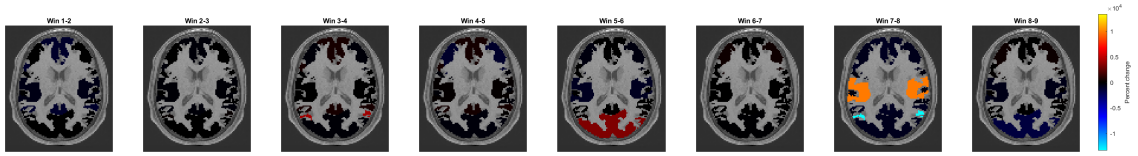

(a) Diverging Components

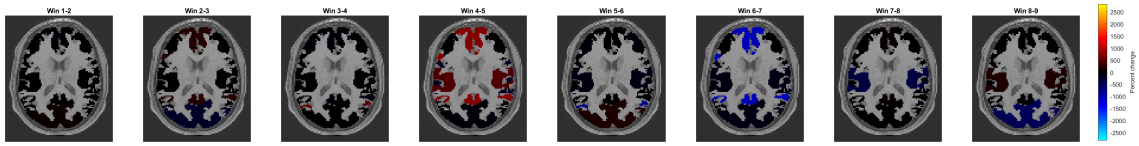

(b) Converging Components

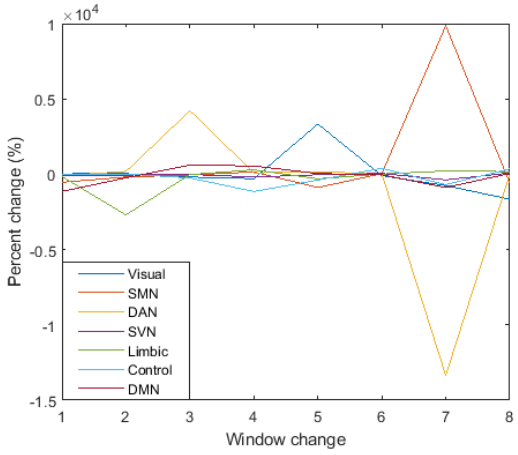

(c) Diverging Components

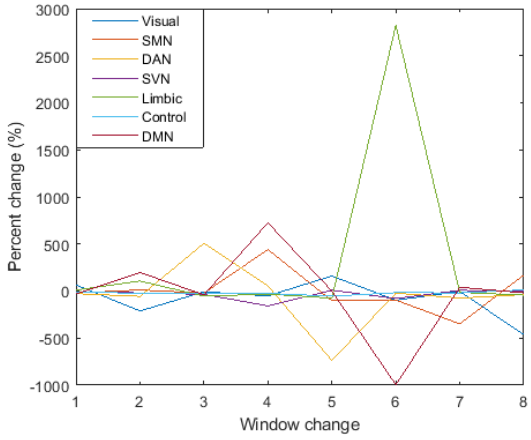

(d) Converging Components

Figure 5.9: The changes (in percentage) of the average β in each network region categorized as (a and c) diverging (DV) and (b and d) converging (CV) component patterns. In (a) and (c), SMN and DAN networks show the most noticeable change in DV as the IWBC peaks leave the sliding windows, while other networks show smaller changes earlier. In (b) and (d), the limbic network shows the largest change as the IWBC peaks leave the sliding windows. The other networks converge earlier, with some networks, including DAN, having two major timing changes in the CV components.

peaks' tips entered the sliding windows. This early change observation is possibly due to IWBC avalanches beginning to rise, affecting the β values and causing the divergence in these components at early windows. During convergence, the change is not as significant but still noticeable after the avalanches have left all the windows (windows 8 to 9). If we observe the specific regions, the most apparent changes can be seen in SMN, control, and SVN networks. Other network regions also show some changes; however, the visual network does not show significant changes in the percentage curve of DC components.

The CD components, on the other hand, are more spread out, with DAN making the most significant change while transitioning from windows 4 to 5. However, as in the other patterns we have seen earlier, the SMN changes earlier by one or two windows compared to other network regions. When diverging back after the IWBC peaks leave the windows, the control network dominates the changes among all other networks. While the SVN network shows an apparent change in the DC components, it does not show evident changes in the CD components as the other networks.

5.3.4 What Do These Signal Content Changes Mean?

These coefficient changes along the IWBC peaks reveal crucial information about how the fMRI signals propagate around the avalanches and across the brain regions. If we look at the size of change within a pattern (Figure 5.11), we have observed that DAN and SMN networks appear to have significant changes in all four diverging and converging patterns. In the DAN network, significant changes happen to almost all type of β patterns as it appears large early in EC components and in the other patterns. Control network changes appear to be prominent only in dwi-changing patterns, while limbic regions change enormously in CV components.

Despite looking into multiple patterns in the mPCASW components, we found no relationship on which component number is tied to which pattern (Figure 5.12). While the CD components have the least number of occurrence, the number of counts in each pattern are almost equally distributed throughout the components. However, most of the first components in each subspace of extended mPCASW, i.e., components 1, 6, 11, and 16, are more prominent in the EC pattern.

In reference to the introduction (Section 5.1), the patterns observed in this study have appeared in several earlier studies. For example, the second lag-thread in (Mitra et al., 2015a) can be observed in our EC component pattern as the somatomotor region appears early compared to other regions. Shine et al. (Shine et al., 2017) also have observed that one of the clusters (cluster 1) shows an evoke in the frontoparietal (FPN) region (or control in our description), giving a significant change to the salience network. As our case study is in the resting-state network, possible transitions are happening from the control to the SVN network, as observed in DC components.

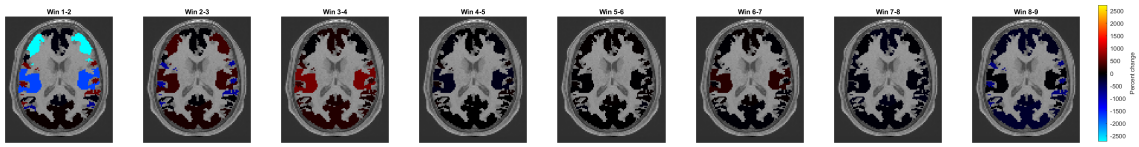

(a) DC Components

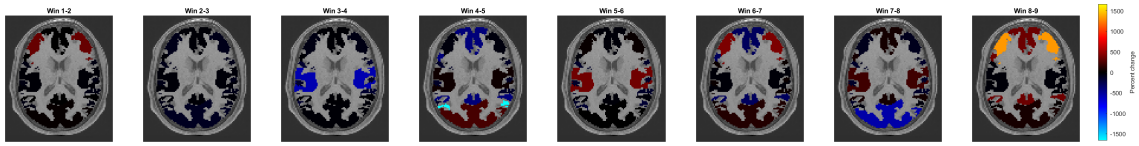

(b) CD Components

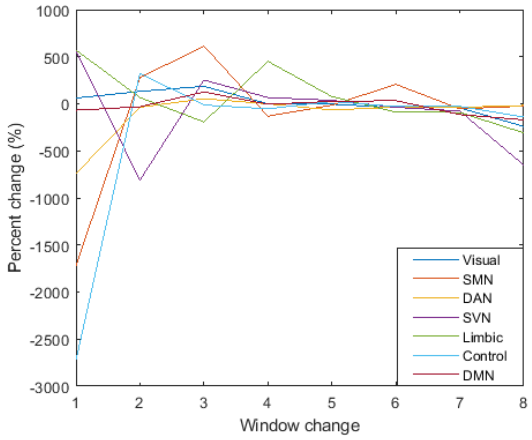

(c) DC Components

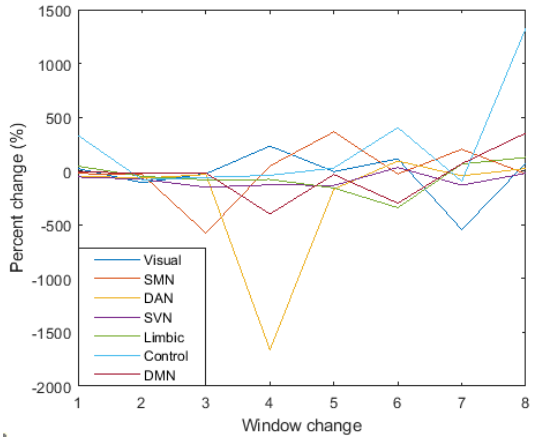

(d) CD Components

Figure 5.10: The changes (in percentage) of the average β in each network region are categorized as (a and c) DC and (b and d) CD component patterns. In (a) and (c), most DC components have large changes as they diverge, but smaller changes happened during the convergence at the end of the 9-window set. The divergence is likely to happen before the IWBC peaks reach the center of the window, i.e., at window 5. In (b) and (d), the CD components are more spread out, with DAN making the most significant change while transitioning from windows 4 to 5. While diverging back after the IWBC peaks leave the windows, the control network dominates the changes among all other networks.

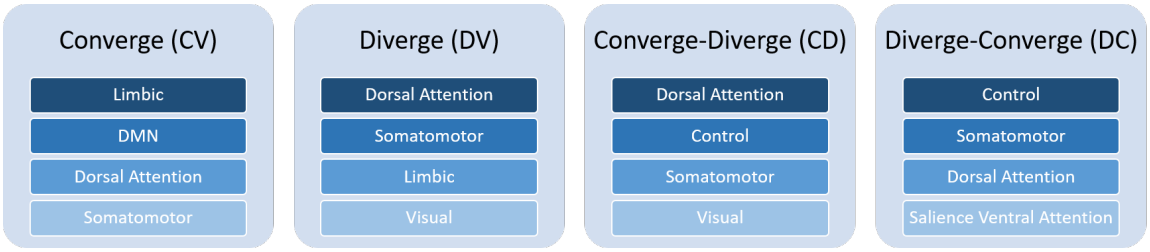

Figure 5.11: Sequence summary of each converging and diverging pattern in percent changes order from large to small. Dorsal attention (DAN) and somatomotor (SMN) networks present large changes in all patterns in the β values around the large IWBC peaks. Interestingly, the Default Mode Network (DMN) does not show large changes in resting-state networks fMRI through our mPCASW β values.

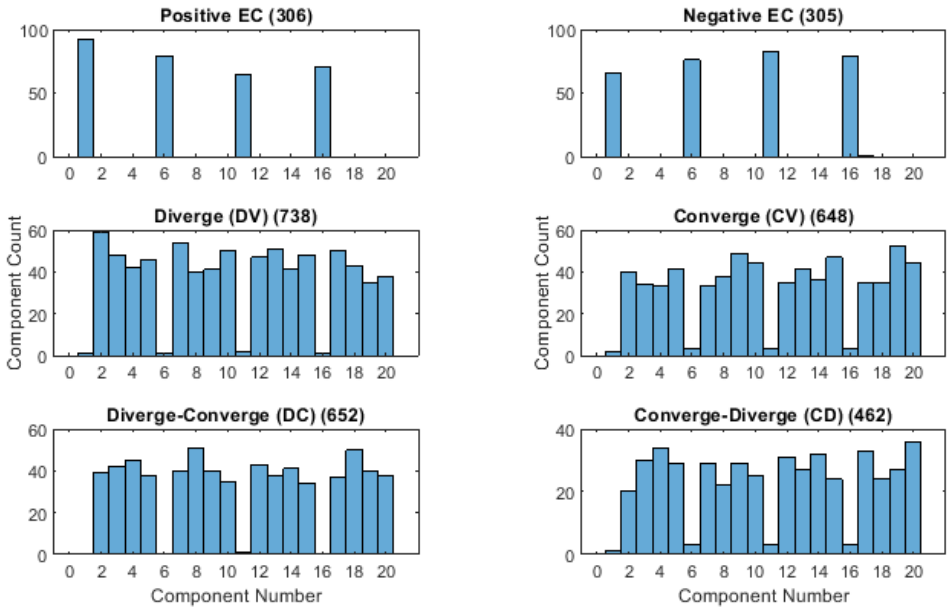

Figure 5.12: Histogram counts for each pattern with the number of components included in the count for each pattern stated in the parentheses. The EC patterns are dominated by components 1, 6, 11, and 16. There is no clear relationship between the component number with the other β patterns; however, the CD pattern appears less than other patterns as the maximum count of components in CD is less than 40.

Our mPCASW components extracted multiple behaviors and pathways of signal transition inside a single fMRI, and we believe this can help explore the unique information flow behavior in a human brain. We also used a 20-timepoint window with four timepoints overlapping two consecutive windows, which translates into 14.4 seconds window with 2.88 seconds overlap time. This reasonable time-window size with short overlapping time allows us to take a closer look at the connectivity of these windows and their behaviors temporally. Furthermore, as we look further into the regions, white matter regions also play a significant role that we should not ignore; thus, extracting the component coefficients in these regions will be crucial to understand further the signal propagation. Finally, we are interested in applying the same method to task-related fMRI as we foresee good observation of different information flowing into brain regions in various pathways.

5.4 Conclusion

We have shown that different signal patterns can be extracted from the mPCASW components around the fMRI IWBC avalanches, from time-sequential behavior to diverging and converging behaviors between the 7-network regions. Multiple regions also have shown substantial and early changes, including somatomotor and dorsal attention networks. While similar propagation patterns of signals have been observed in several earlier studies, we add more insights and a new approach to observe the signal behavior in the brain to support understanding the brain network structure through the decomposed mPCASW components.

CHAPTER 6

Summary and Future Works

As fMRI has become more prevalent in investigating brain functionality and aiding brain-related disease treatments, various research methods have been introduced to understand the complexity and dynamics of the human brain. In this work, we have defined a novel algorithm, the modified Principal Component Analysis for Sliding-Windows (mPCASW), its characteristics, and several findings as we processed the resting state fMRI data. In this summary, we highlighted the key takeaways from Chapters 3 to 5 and several promising possibilities for future works related to this study.

The mPCASW and Its Components in Resting-state fMRI

In Chapter 3, we introduced a modified PCA algorithm that can be applied to a spatiotemporal dataset in a sliding-window approach, or mPCASW. Chapter 4 extends the algorithm to provide more components comparable with other available decompositions methods. The main objective is ensuring connectivity between the temporal windows sliding across time and having a simple approach that is not computationally expensive. This algorithm also tries to reach the orthogonality, thus, the uncorrelatedness of the components' basis vectors like we generally have in the classical PCA.

In terms of visualization of the mPCASW components, we observed the behaviors of the basis vectors in fMRI in different sets of visualizations in both chapter 4 and 5. We have shown the signal content transitions using the standard deviation volume (SDV), transform coefficients, β, for each fMRI brain voxels projected from the mPCASW components, and clusters of the basis vectors to observe when the components are 'activated'. We also observed how the components' coefficients could be categorized based on their patterns around the avalanches into several patterns where we can learn some brain regions' timing propagations and the possibility of synchronization and desynchronization during the whole brain scan.

With these promising results, several suggestions for future works can be continued based on this study. First, as we observed the evidence of the detailed signal content transitions, as well as the timing propagations in the mPCASW components, we would like to extend this into other types of fMRI, such as sleep and disease-related fMRI scans. Many findings have stated the changes they observed through the scans, even in real-time (Gembris et al., 2000; Weiskopf et al., 2007), and we believe more in-depth findings can be observed into each of the mPCASW components' transform coefficients. Other studies also have found differences in several regions between healthy and brain-related disease patients (Ma et al., 2014; Rolls, 2021; Rolls et al., 2021; Jones et al., 2011); therefore, applying the mPCASW method could help explore the differences in

more detail through its decomposed components.

Secondly, within the same subjects we used in this work, another focus is looking further into the structural brain regions instead of the resting state network. In chapter 4, we observed the brain voxels' transform coefficients transitions as a whole, where it changes significantly around the avalanches but not so much or minor changes in the non-avalanche timezone. We also have seen an excerpt of a sleep fMRI transition in the insula and thalamus regions, where these regions have higher coefficient values in the first few components compared to the regular resting-state fMRI. Chapter 5 presented results based on Yeo's 7-network regions, and several networks, such as the somatomotor and dorsal attention network regions, were highlighted to be more stand-out than other regions. Extracting these β of each component into smaller-volume regions will help further understand the signal content flow within the brain networks as well as the possible differences between the left and right regions. Great atlases such as the Brodmann areas (Brodmann, 1909; Mai, 2017), the AAL3 (Rolls et al., 2020), and the SLANT (Huo et al., 2019) atlases can be used to extract the gray matter regions.

Lastly, which we separated from the second suggestion, is to further use this method in learning the signal content propagations within the white matter (WM) regions. Many important yet used to be controversial findings have been recorded related to the WM, such as the evidence of the WM activation in the fMRI signals (Gawryluk et al., 2011, 2014; Tae et al., 2014; Grajauskas et al., 2019), signal time delays in the WM regions relative to stimulus (Ding et al., 2018; Li et al., 2019), as well as the pathways connection with the gray matter regions (Wu et al., 2017; Wang et al., 2019). One hypothesis could be made is that some of the mPCASW components could reflect the signal content transitions of the WM regions, but this is left to be extracted and analyzed further.

Impact on fMRI Global Means to the Data Processing

As we have done different analyses on the resting-state fMRI (plus a small dataset of sleep fMRI), we compared two covariance matrices that use different types of mean and analyzed the effect of these covariance matrices in the mpCASW components, particularly in the rsfMRI data. Our results show that the mPCASW components do not show any differences in the transform coefficient patterns, although the components' basis vectors show slightly higher dot products when the global means are removed from the dataset before the covariance matrix is computed. More details of the results are described in Appendix C. Several findings have debated how the global means, or what most articles call the global signal (GS), could create anticorrelations between the brain regions (Nalci et al., 2017; Fox et al., 2009; Murphy et al., 2009; Saad et al., 2012). Another related topic to the covariance effect is that the covariance matrix calculation depends on the stationarity of the fMRI signals. For example, (Jones et al., 2012) highlighted his study based on the non-

stationarity of the brain signal, while the (Rubinov and Sporns, 2010) and many others preprocessed their data with signal stationarity assumption. Many fMRI analysis software products also remove the GS before computing the data's covariance matrix and further processing; thus, this affects many studies learning the functional connectivity of the brain.

With more complex explorations in this field, it is probably crucial to identify or at least provide a set of characteristics of fMRI signals for the researchers to decide the most proper method to process the fMRI data. Then, with the correct way of processing, more accurate statistical analysis and interpretations can be made from both scientific and neurological perspectives.

Vision of the Future For Better Healthcare

In summary, to better analyze fMRI, it is imperative to understand the structure and functionality of the brain. Humans have been creating ever-more complicated and complex computer systems for centuries. Be that as it may, the comparison of how intricate the human brain is yet to be fully discovered. Being the most complicated human organ, further research of the brain's intricacies should be done to the extent of understanding every inch of its abstract system. This study was set out to present novel tools in finding the connections between regions in the brain, subsequently visualize these connections in unique ways that have not been done in other fMRI researches. This work is hoped to provide better comprehension not only limited to healthy human brains, but essentially to increase the ability of the healthcare community to understand and make better diagnosis in needy patients and accordingly provide better treatment to them in the future.

Appendices

Appendix A

Maximum Number of Components in the Extended mPCASW

As mentioned in Chapter 4.2.1, the maximum number of components that we can obtain using the original mPCASW algorithm is $N_{hop}+1$. We will show here how we reached this restriction.

The first basis vector, $\underline{c}_1$ is obtained by the standard PCA algorithm. Thus, there are no orthogonality constraints on this vector. Here, consider one window extracted from $\underline{c}_1$, $\underline{c}_{1w}$,

$$\underline{c}_{1w} = \begin{bmatrix} \underline{p}_1 \\ \underline{v}_1 \end{bmatrix} \tag{A.1}$$

where $\underline{p}_1$ is the first $(N_{win} - N_{hop})$ $\underline{c}_1$ elements from the previous window and $\underline{v}_1$ contains the last N_{hop} elements of $\underline{c}_1$ in window w. We can then form the second basis vector in the same form, $\underline{c}_{2w}$.

$$\underline{c}_{2w} = \begin{bmatrix} \underline{p}_2 \\ \underline{v}_2 \end{bmatrix}. \tag{A.2}$$

This window w must satisfy the orthogonality constraint:

$$\underline{c}_{1w}\underline{c}_{2w} = 0 \tag{A.3}$$

which yields into

$$\underline{p}_1^T \underline{p}_2 + \underline{v}_1^T \underline{v}_2 = 0. \tag{A.4}$$

Therefore, we have one linear equation with N_{hop} unknowns to solve, i.e., the elements to of $\underline{v}_2$. We can find these values by solving this equation.

Next, consider the corresponding window from the third basis vector, $\underline{c}_{3w}$,

$$\underline{c}_{3w} = \begin{bmatrix} \underline{p}_3 \\ \underline{v}_3 \end{bmatrix}. \tag{A.5}$$

We now have this window to satisfy two more orthogonality constraints,

$$\underline{p}_1^T \underline{p}_3 + \underline{v}_1^T \underline{v}_3 = 0, \tag{A.6}$$

$$\underline{p}_2^T \underline{p}_3 + \underline{v}_2^T \underline{v}_3 = 0. \tag{A.7}$$

With three linear equations A.4, A.6, and A.7, and N_{hop} unknowns in the $\underline{v}_3$ elements, we can find the solutions for $\underline{v}_3$. We can continue searching for $\underline{v}_i$ up to $N_{hop}+1$ basis vectors. When we reach $N_{hop}+1$, we will have $N_{hop}+1$ linear equations and N_{hop} unknowns, which results in the linear system to be overdetermined and almost always have no solution. Therefore, in the mPCASW algorithm, we can only guarantee the orthogonality of the windows for $N_{hop}+1$ basis vectors.

Appendix B

Clusters of Components in the Extended mPCASW

This appendix presents figures of all clusters for two separate timepoints of the IWBC in Figure 4.1 of the manuscript as described in Chapter 4. Clusters that contain the highest and lowest mPCASW coefficients for both timepoints are highlighted in Figure 4.9.

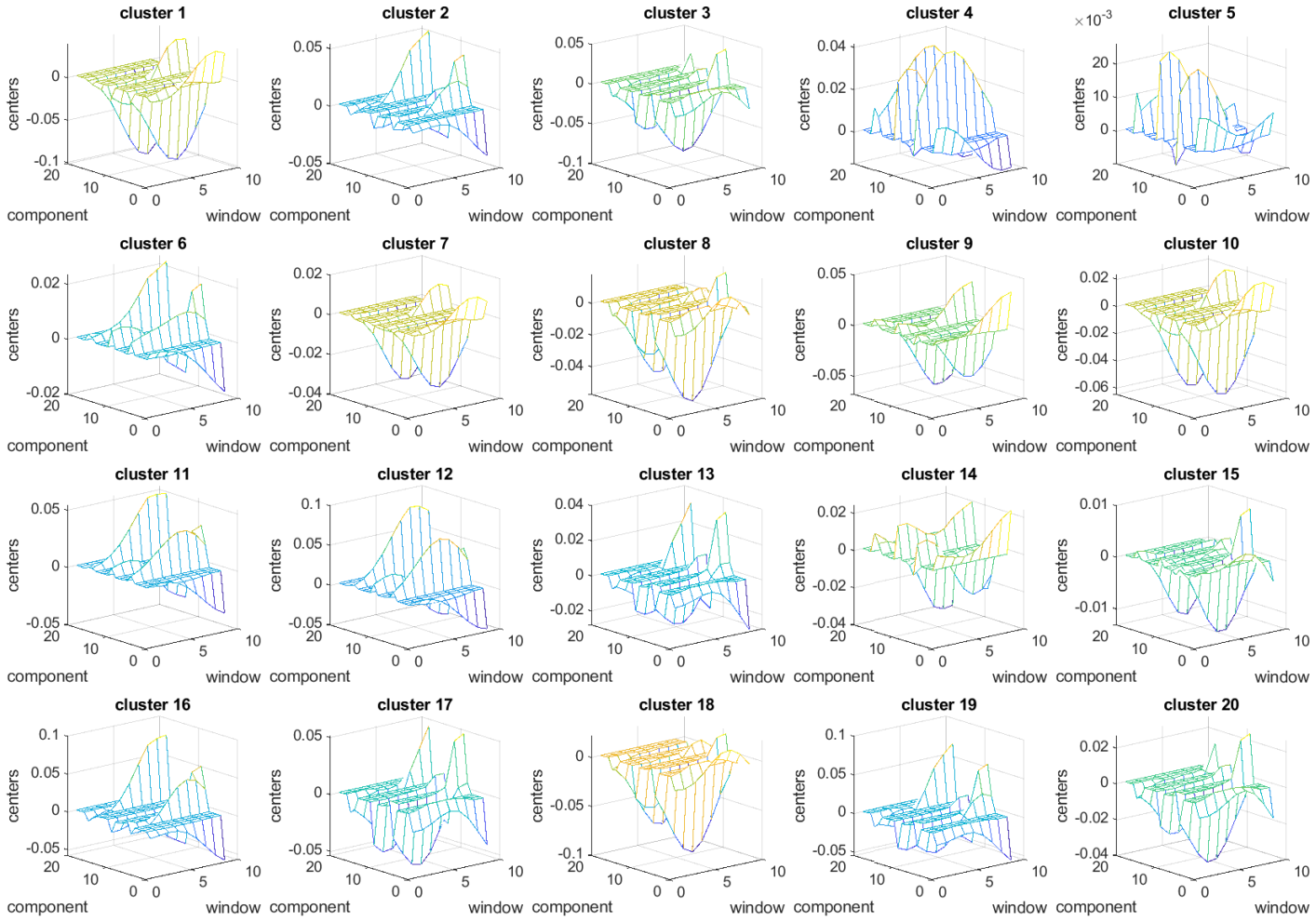

Figure B.1: Clusters in each component across 9 windows in a single subject. The highest IWBC timepoint (timepoint 777 at 559.44 seconds) in Figure 1 is in the middle of fifth window, and therefore this timepoint is sledded in window 3-7. As mentioned in Section 4.3.3, clusters 12 and 11 showed the components with highest coefficients, while clusters 1 and 10 contains the components with lowest coefficients.

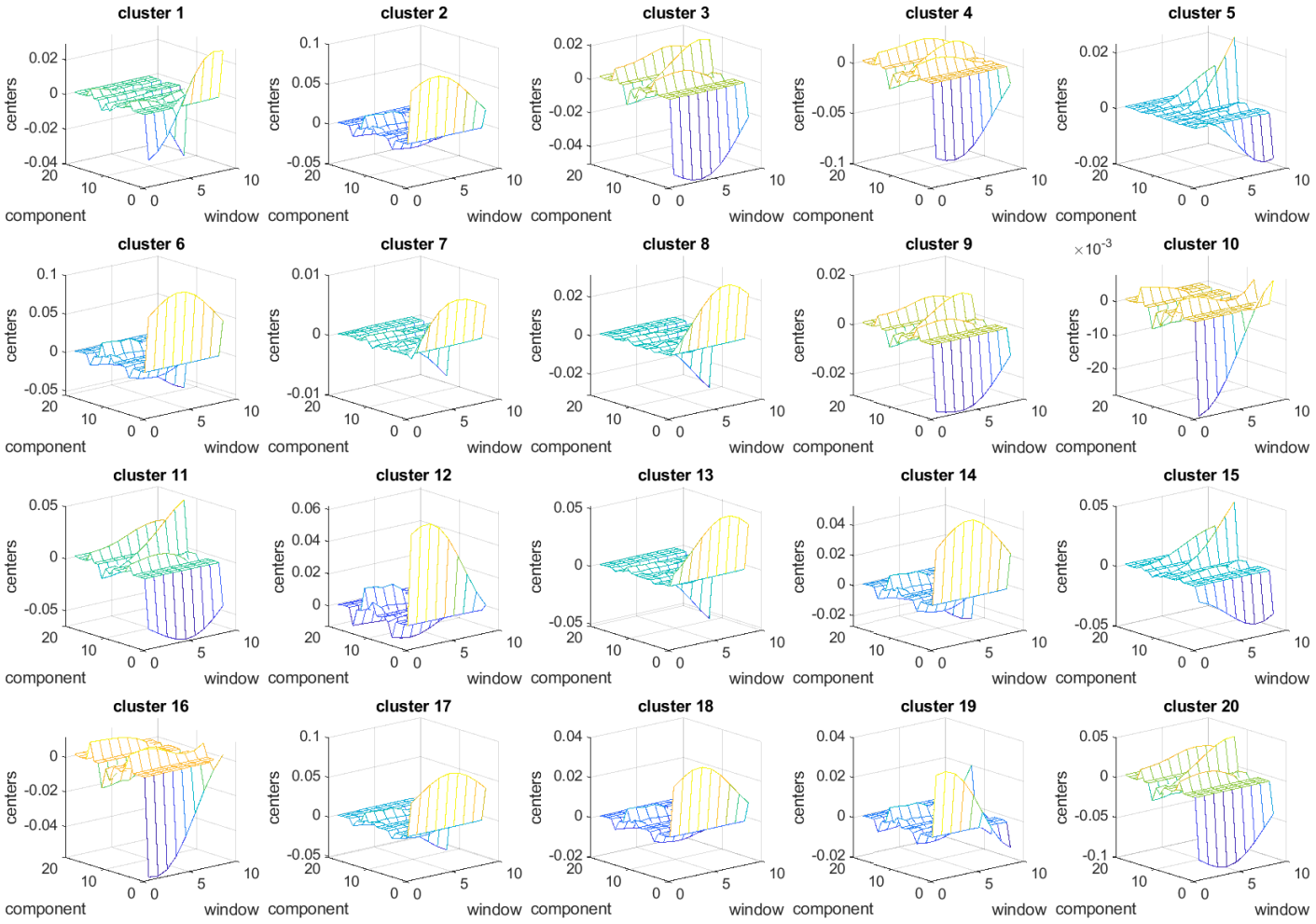

Figure B.2: Clusters in each component across 9 windows in a single subject. The timepoint 256 at 184.32 seconds in Figure 1 is in the middle of fifth window, and therefore this timepoint is sledded in window 3-7. As mentioned in Section 4.3.3, clusters 6 and 17 showed the components with highest coefficients, while clusters 20 and 11 contains the components with lowest coefficients.

Appendix C

Impact of different covariance matrices definition in fMRI data

Functional magnetic resonance imaging (fMRI) is often processed using available methods that produce reliable results where reasonable interpretations from a neurophysiological perspective can be made. However, calculating a covariance matrix, which is very popular in fMRI analysis, can be tricky as the calculations can differ depending on whether the dataset is stationary or not. Here, we compare two covariance matrix calculations to observe the effect on our modified Principal Component Analysis for sliding windows (mPCASW) components. The first method is based on the standard Principal Component Analysis (PCA), where the temporal mean, called the global means, is subtracted from the dataset before calculating the covariance matrix. The second method removes the mean of each voxel across the time, producing the covariance matrix that is still affected by the global means of the fMRI. We found that the mPCASW basis vectors retain their high orthogonality while one of the dot products went slightly higher than the other. The transform coefficients projected from the basis vectors also showed similar patterns in both methods. Therefore, we believe these two covariance matrices do not significantly impact our mPCASW components' basis vectors to analyze the signal content flow across the scans.

C.1 Analysis

While working on the fMRI datasets, we found two distinct methodologies during preprocessing. Principal component analysis (PCA) decomposes a dataset into a set of basis vectors that are orthogonal and uncorrelated to each other. The classic approach in PCA is to decompose the eigenvalues on the covariance matrix of the data of interest. A covariance matrix of a data X with the size of $N \times M$ can be defined as follows:

$$K_{xx} = \frac{1}{M-1} \sum_{i=1}^{M} \left(\underline{x}_i - \underline{\mu} \right) \left(\underline{x}_i - \underline{\mu} \right)^T \tag{C.1}$$

where the mean, μ, is defined as a vector of the sample mean of each column in the data (Equation C.2. In this manuscript, it is also similar to the global means of fMRI data as defined in Chapter 3:

$$\underline{\mu} = \frac{1}{M} \sum_{i=1}^{M} \underline{\mathbf{x}}_i \tag{C.2}$$

However, if we assume the fMRI data to be wide-sense stationary, we assume the voxels or columns in general to be stationary (Ibe, 2014), and thus present a set of means across the columns. The resulting covariance matrix using this approach becomes slightly different as we do not remove the global means, but

the column's means.

In fMRI studies, there are several studies, but not many, learning whether this type of data is stationary or not. One study investigated the stationarity of fMRI during motor tasking and found some non-stationarity signals in several brain areas (Muhei-aldin et al., 2014). They also stated that most of the current literature does not measure the stationarity of the signals prior to processing.

In this chapter, we take both approaches and compare the results of the mPCASW methods using both mean definitions. We process a a single subject dataset from fMRI data in Chapter 4 to observe the overall behavior that might be affecting our studies. The resulting basis vectors in both methods show small variances in their dot products while maintaining the average dot products across different window and sliding point sizes. We also observe the transform coefficients projected from mPCASW components, and both methods' behaviors around IWBC peaks stay similar.

C.1.1 Covariance Matrix Based on Standard PCA Definition

We defined the first method as the standard PCA method, where it requires zero mean across the columns of the dataset X. Based on the Equation C.2, we will have a set of mean of $N \times 1$, and the resulting covariance from Equation C.1 will have the size of $N \times N$.

C.1.2 Covariance Matrix Based on WSS Definition

Assuming the fMRI to be wide-sense stationary (WSS) or 'weakly stationary' used in (Muhei-aldin et al., 2014), we calculated the mean of the columns across the row producing a set of $1 \times M$, where each value is the mean for column M. To differentiate the symbols used, here we use m to represent the mean for this definition.

$$\underline{m_i} = \frac{1}{N} \sum_{n=0}^{N-1} \underline{\mathbf{x}_i} \tag{C.3}$$

Therefore, its covariance matrix, κ can be estimated as follows:

$$\kappa_{xx} \;=\; \frac{1}{M-1} \sum_{i=1}^{M} (\underline{x_i} - \; m_i) \, (\underline{x_i} - \; m_i)^T \tag{C.4}$$

C.1.3 mPCASW Application on fMRI Data

We applied the extended mPCASW method described in Chapter 4 on the covariance matrices individually from each subject and generated the components' basis vectors, C. In our mPCASW processing, we processed the 1000 timepoints of fMRI signals from each subject using a sliding window size of $N_{win} = 20$ with

overlapping time of $N_{hop} = 4$. For each subject, each method will generate a 246×20 as a result of 246 windows and 20 components.

We then compare the results of both methods based on three statistical representations:

- the dot products of the basis vectors, C of mPCASW,
- the average dot products of C across different window sizes and overlapping windows, and
- the transform coefficient projected from the components' basis vectors. Transform coefficients, β for each sliding window w is defined as

$$\beta_d[w] = c_d[w]^T X[w] \tag{C.5}$$

where c_d is the basis vectors from component d of C obtained from the mPCASW.

C.2 Results

The orthogonality of basis vectors is observed based on their dot products to ensure their uncorrelatedness, which is one of the core parts of PCA algorithm. In a single subject, we observed slightly higher dot products as we removed the global means before the mPCASW was applied compared to the method where the global means are not removed from the dataset (Figure C.1). However, the dot products remain low with 10^{-8} in a single subspace and 10^{-1} in the overall dot product across different subspaces.

As we vary the N_{win} and N_{hop}, the dot products pattern in a subject, as well as the average across all subjects, maintained to be similar between both covariance calculation methods (Figure C.2). As we have seen in the earlier chapter, smaller N_{win} showed us slightly unstable dot products across different N_{hop}, but the combinations are more stable from $N_{win} = 20$ and larger. Regardless of whether the input is demeaned temporally or spatially, the mPCASW method is robust to calculate its components' basis vectors.

We also compared the transform coefficients, β (Equation C.5) of a subject using both approaches. Despite the orthogonality of the basis vectors having changed slightly though they still maintain their low dot products, we still see similar patterns in the β around the IWBC avalanches (Figure C.3). The values in β for the components are different between both methods since the covariance matrices are not equal, and therefore, the components' β that are highly significant are different. However, in terms of looking at the components' pattern changes, subtracting the global means reflects little difference for our analysis.

In terms of components' basis analysis, these two methods provide similar with slight differences in terms of the orthogonality and the projected coefficient values. However, as mentioned in (Muhei-aldin et al., 2014),

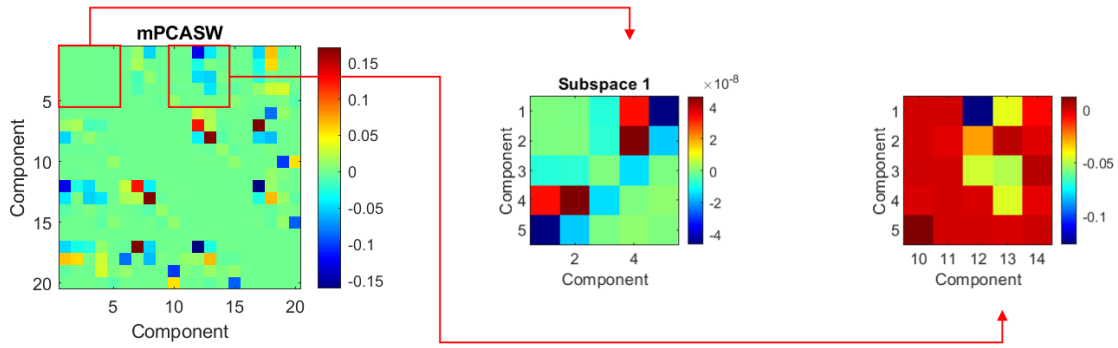

(a) Removed global means

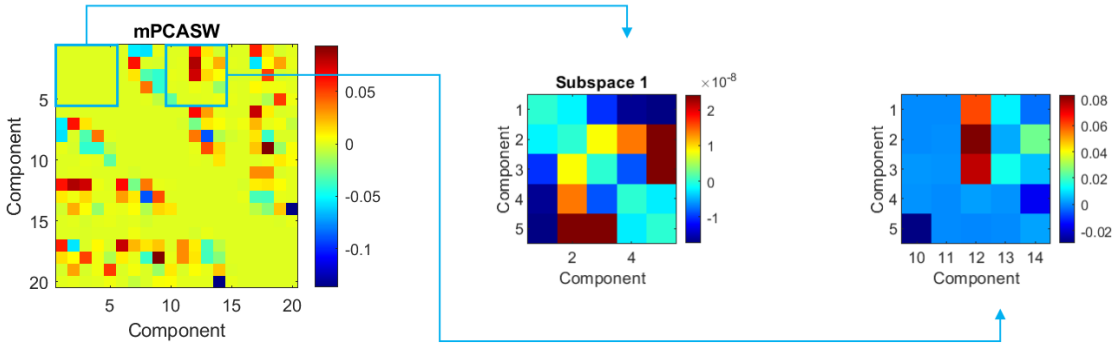

(b) With global means

Figure C.1: The dot products of the mPCASW basis vectors from a single subject with the window setting of $N_{win} = 20$ and $N_{hop} = 4$. The covariance matrices were calculated (a) with removing global means and (b) with global means before mPCASW algorithm is applied. In both cases, the dot products remain low especially in the first subspace (middle squares). It is notable that the removing global means in the covariance produce higher dot products as it could reach 10^{-1}, but it remains at the lower values.

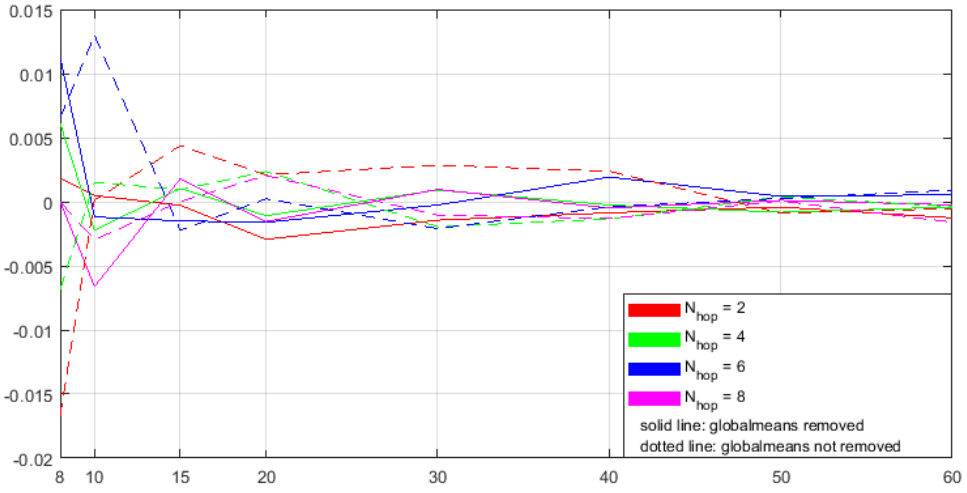

Figure C.2: The average dot products in a subject to represent the orthogonality of the mPCASW basis vectors across different N_{win} and N_{hop} with removing global means (solid lines) and with global means (dotted lines) in the covariance matrix before mPCASW algorithm is applied. There are huge variances in the dot products around smaller N_{win} across different N_{hop} especially when the window size reaches 8 and 10 timepoints. As the window size N_{win} becomes larger, the size of both N_{win} and N_{hop} do not affect much on the dot products, and thus, the mPCASW basis vectors reaches close to orthogonality as the average dot products converges to zero.

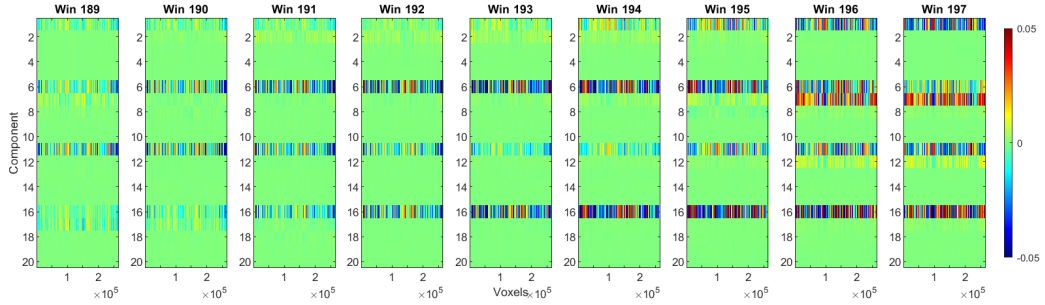

(a) Removed global means

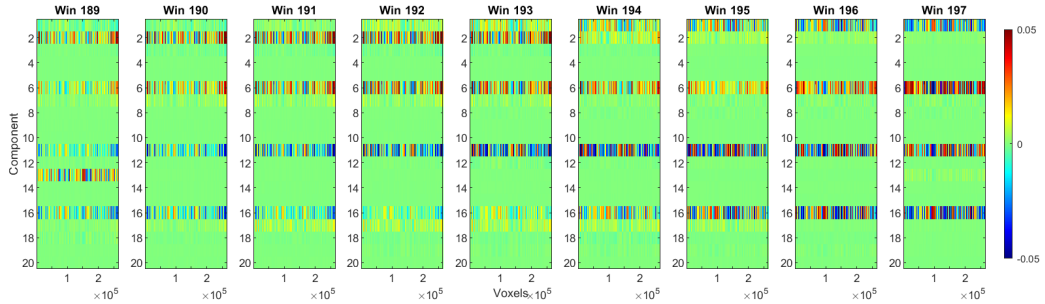

(b) With global means

Figure C.3: β of a subject calculated (a) with removing global means and (b) with global means in the covariance matrix before the mPCASW algorithm is applied. The observed pattern of β from the whole brain remain similar as the are groups of voxels that become deactivated or activated during the IWBC avalanches in each component.

it is crucial to further investigate the stationarity of the fMRI signal if the covariance matrices are being used in the fMRI analysis to provide more accurate results and interpretations in the future.

C.3 Summary

We have shown two ways to calculate the covariance matrix of the fMRI data. The first used the standard PCA definition, which removes the data globalmeans before calculating the covariance matrix. In contrast, the second keeps the globalmeans in effect to the dataset and only removes each voxel's mean across the scans. We compared the orthogonality of the mPCASW basis vectors when using both covariance matrices in a single setting, as well as the average across different sliding window sizes and overlapping times. We found slight changes with higher dot products in the standard PCA's covariance matrix but still maintained the low values for us to prove their orthogonality behavior. The resulting transform coefficient values in separate components are also similar in both ways, thus providing evidence that on either method, mPCASW can still produce similar results in its components in the fMRI data analysis.

References

Allen, E. A., Damaraju, E., Plis, S. M., Erhardt, E. B., Eichele, T., and Calhoun, V. D. (2014). Tracking whole-brain connectivity dynamics in the resting state. *Cerebral Cortex*, 24(3):663–676.

Ances, B. M. (2004). Coupling of changes in cerebral blood flow with neural activity: What must initially dip must come back up. *Journal of Cerebral Blood Flow & Metabolism*, 24(1):1–6. PMID: 14688611.

Andersen, A. H., Gash, D. M., and Avison, M. J. (1999). Principal component analysis of the dynamic response measured by fMRI: a generalized linear systems framework. *Magnetic Resonance Imaging*, 17(6):795–815.

Badeau, R., Richard, G., and David, B. (2004). Sliding window adaptive SVD algorithms. *IEEE Transactions on Signal Processing*, 52(1):1–10.

Beckmann, C. F., DeLuca, M., Devlin, J. T., and Smith, S. M. (2005). Investigations into resting-state connectivity using independent component analysis. *Philosophical transactions of the Royal Society of London. Series B, Biological sciences*, 360(1457):1001–13.

Beggs, J. M. and Plenz, D. (2003). Neuronal avalanches in neocortical circuits. *Journal of Neuroscience*, 23(35):11167–11177.

Beliveau, V., Svarer, C., Frokjaer, V. G., Knudsen, G. M., Greve, D. N., and Fisher, P. M. (2015). Functional connectivity of the dorsal and median raphe nuclei at rest. *NeuroImage*, 116:187–195.

Bell, A. J. and Sejnowski, T. J. (1995). An information-maximization approach to blind separation and blind deconvolution. *Neural Computation*, 7(6):1129–1159.

Bell, C. S. (2018). *Seed-based correlation analysis and instantaneous global correlation analysis for resting state fMRI*. PhD thesis, Vanderbilt University.

Bercovich, E. and Javitt, M. C. (2018). Medical Imaging: From Roentgen to the Digital Revolution, and Beyond. *Rambam Maimonides Medical Journal*, 9(4):e0034.

Blausen Medical, B. M. (2014). Brain Anatomy (Sagittal). Animation in the reference. [Online; retrieved on October 15, 2022] Available at https://commons.wikimedia.org/wiki/File:Brain_Anatomy_(Sagittal).png under Creative Common license (CC BY-SA 4.0) via Wikimedia Commons.

Bolt, T., Nomi, J. S., Bzdok, D., Salas, J. A., Chang, C., Thomas Yeo, B. T., Uddin, L. Q., and Keilholz, S. D. (2022). A parsimonious description of global functional brain organization in three spatiotemporal patterns. *Nature Neuroscience*, 25(8):1093–1103.

Brodmann, K. (1909). *Vergleichende Localisationslehre der Grosshirnrinde in ihren Prinzipien dargestellt auf Grund des Zellenbaues*. J. A. Barth, 1909.

Buckner, R. L., Andrews-Hanna, J. R., and Schacter, D. L. (2008). The Brain's Default Network: Anatomy, Function, and Relevance to Disease. *Annals of the New York Academy of Sciences*, 1124(1):1–38.

Bugli, C. and Lambert, P. (2007). Comparison between principal component analysis and independent component analysis in electroencephalograms modelling. *Biometrical Journal*, 49(2):312–327.

Cardoso, J.-F. (1997). Infomax and maximum likelihood for blind source separation. *IEEE Signal Processing Letters*, 4(4):112–114.

Cardoso, J. F. and Souloumiac, A. (1993). Blind beamforming for non-gaussian signals. *IEE Proceedings F - Radar and Signal Processing*, 140(6):362–370.

Cauda, F., D'agata, F., Sacco, K., Duca, S., Geminiani, G., and Vercelli, A. (2011). Functional connectivity of the insula in the resting brain. *NeuroImage*, 55(1):8–23.

Chang, C. and Glover, G. H. (2010). Time-frequency dynamics of resting-state brain connectivity measured with fMRI. *NeuroImage*, 50(1):81–98.

Chavhan, G. B., Babyn, P. S., Thomas, B., Shroff, M. M., and Haacke, E. M. (2009). Principles, techniques, and applications of T2*-based MR imaging and its special applications. *Radiographics : a review publication of the Radiological Society of North America, Inc*, 29(5):1433–49.

Clement, S., Bellizzi, S., Cochelin, B., and Ricciardi, G. (2014). Sliding window proper orthogonal decomposition: Application to linear and nonlinear modal identification. *Journal of Sound and Vibration*, 333(21):5312 – 5323.

Collins, D. L., Holmes, C. J., Peters, T. M., and Evans, A. C. (1995). Automatic 3-D model-based neuroanatomical segmentation. *Human Brain Mapping*, 3(3):190–208.

Daubechies, I., Roussos, E., Takerkart, S., Benharrosh, M., Golden, C., D'Ardenne, K., Richter, W., Cohen, J. D., and Haxby, J. (2009). Independent component analysis for brain fMRI does not select for independence. *Proceedings of the National Academy of Sciences of the United States of America*, 106(26):10415–10422.

de Andrés, I., Garzón, M., and Reinoso-Suárez, F. (2011). Functional anatomy of non-REM sleep. *Frontiers in Neurology*, 2:70.

de Pasquale, F., Della Penna, S., Snyder, A. Z., Marzetti, L., Pizzella, V., Romani, G. L., and Corbetta, M. (2012). A Cortical Core for Dynamic Integration of Functional Networks in the Resting Human Brain. *Neuron*, 74(4):753–764.

Ding, Z., Huang, Y., Bailey, S. K., Gao, Y., Cutting, L. E., Rogers, B. P., Newton, A. T., and Gore, J. C. (2018). Detection of synchronous brain activity in white matter tracts at rest and under functional loading. *Proceedings of the National Academy of Sciences of the United States of America*, 115(3):595–600.

Doucet, G., Naveau, M., Petit, L., Delcroix, N., Zago, L., Crivello, F., Jobard, G., Tzourio-Mazoyer, N., Mazoyer, B., Mellet, E., et al. (2011). Brain activity at rest: a multiscale hierarchical functional organization. *Journal of neurophysiology*, 105(6):2753–2763.

Doucet, G. E., Lee, W. H., and Frangou, S. (2019). Evaluation of the spatial variability in the major resting-state networks across human brain functional atlases. *Human brain mapping*, 40(15):4577—4587.

Doucet, G. E., Rasgon, N., McEwen, B. S., Micali, N., and Frangou, S. (2018). Elevated body mass index is associated with increased integration and reduced cohesion of sensory-driven and internally guided resting-state functional brain networks. *Cerebral Cortex*, 28(3):988–997.

Dubuc, B. (2012). The brain from top to bottom. mcgill university.

Fox, M. D., Zhang, D., Snyder, A. Z., and Raichle, M. E. (2009). The global signal and observed anticorrelated resting state brain networks. *Journal of Neurophysiology*, 101(6):3270–3283.

Friston, K. J. (2011). Functional and effective connectivity: A Review. *Brain Connectivity*, 1(1):13–36.

Friston, K. J., Frith, C. D., Liddle, P. F., and Frackowiak, R. S. (1993). Functional connectivity: the principal-component analysis of large (PET) data sets. *Journal of cerebral blood flow and metabolism : official journal of the International Society of Cerebral Blood Flow and Metabolism*, 13(1):5–14.

Gawryluk, J. R., Mazerolle, E. L., Beyea, S. D., and D'Arcy, R. C. (2014). Functional MRI activation in white matter during the Symbol Digit Modalities test. *Frontiers in Human Neuroscience*, 8(AUG):589.

Gawryluk, J. R., Mazerolle, E. L., Brewer, K. D., Beyea, S. D., and D'Arcy, R. C. (2011). Investigation of fMRI activation in the internal capsule. *BMC Neuroscience*, 12(1):56.

Gembris, D., Taylor, J. G., Schor, S., Frings, W., Suter, D., and Posse, S. (2000). Functional magnetic resonance imaging in real time (FIRE): Sliding- window correlation analysis and reference-vector optimization. *Magnetic Resonance in Medicine*, 43(2):259–268.

Glasser, M. F., Sotiropoulos, S. N., Wilson, J. A., Coalson, T. S., Fischl, B., Andersson, J. L., Xu, J., Jbabdi, S., Webster, M., Polimeni, J. R., Essen, D. C. V., and Jenkinson, M. (2013). The minimal preprocessing pipelines for the Human Connectome Project. *NeuroImage*, 80:105 – 124. Mapping the Connectome.

Gonzalez-Castillo, J., Fernandez, I. S., Handwerker, D. A., and Bandettini, P. A. (2022). Ultra-slow fmri fluctuations in the fourth ventricle as a marker of drowsiness. *NeuroImage*, 259:119424.

Goodale, S. E., Ahmed, N., Zhao, C., de Zwart, J. A., Özbay, P. S., Picchioni, D., Duyn, J., Englot, D. J., Morgan, V. L., and Chang, C. (2021). fMRI-based detection of alertness predicts behavioral response variability. *eLife*, 10:e62376.

Gordon, E. M., Laumann, T. O., Adeyemo, B., Huckins, J. F., Kelley, W. M., and Petersen, S. E. (2016). Generation and evaluation of a cortical area parcellation from resting-state correlations. *Cerebral cortex*, 26(1):288–303.

Grajauskas, L. A., Frizzell, T., Song, X., and D'Arcy, R. C. (2019). White Matter fMRI Activation Cannot Be Treated as a Nuisance Regressor: Overcoming a Historical Blind Spot. *Frontiers in Neuroscience*, 13:1024.

Greicius, M. D., Krasnow, B., Reiss, A. L., and Menon, V. (2003). Functional connectivity in the resting brain: a network analysis of the default mode hypothesis. *Proceedings of the National Academy of Sciences*, 100(1):253–258.

Heine, L., Soddu, A., Gomez, F., Vanhaudenhuyse, A., Tshibanda, L., Thonnard, M., Charland-Verville, V., Kirsch, M., Laureys, S., and Demertzi, A. (2012). Resting state networks and consciousness. *Frontiers in Psychology*, 3:295.

Hindriks, R., Adhikari, M. H., Murayama, Y., Ganzetti, M., Mantini, D., Logothetis, N. K., and Deco, G. (2016). Can sliding-window correlations reveal dynamic functional connectivity in resting-state fMRI? *NeuroImage*, 127:242–256.

Holtz, J. (2010). *Applied Clinical Neuropsychology: An Introduction*. Springer Publishing Company.

Huettel, S., Song, A., and McCarthy, G. (2014). *Functional Magnetic Resonance Imaging, Third Edition*. Sinauer Associates, Inc.

Huo, Y., Xu, Z., Xiong, Y., Aboud, K., Parvathaneni, P., Bao, S., Bermudez, C., Resnick, S. M., Cutting, L. E., and Landman, B. A. (2019). 3D whole brain segmentation using spatially localized atlas network tiles. *NeuroImage*, 194:105–119.

Hutchison, R. M., Womelsdorf, T., Allen, E. a., Bandettini, P. a., Calhoun, V. D., Corbetta, M., Della Penna, S., Duyn, J. H., Glover, G. H., Gonzalez-Castillo, J., Handwerker, D. a., Keilholz, S., Kiviniemi, V., Leopold, D. a., de Pasquale, F., Sporns, O., Walter, M., and Chang, C. (2013a). Dynamic functional connectivity: Promise, issues, and interpretations. *NeuroImage*, 80:360–378.

Hutchison, R. M., Womelsdorf, T., Gati, J. S., Everling, S., and Menon, R. S. (2013b). Resting-state networks show dynamic functional connectivity in awake humans and anesthetized macaques. *Human Brain Mapping*, 34(9):2154–2177.

Hyvärinen, A. (1999). Fast and robust fixed-point algorithms for independent component analysis. *IEEE Transactions on Neural Networks*, 10(3):626–634.

Hyvärinen, A., Karhunen, J., and Oja, E. (2002). *ICA by Maximization of Nongaussianity*, chapter 8, pages 165–202. John Wiley & Sons, Ltd.

Hyvärinen, A. and Oja, E. (2000). Independent component analysis: Algorithms and applications. *Neural Netw.*, 13(4-5):411–430.

Ibe, O. C. (2014). Chapter 12 - Special Random Processes. In Ibe, O. C., editor, *Fundamentals of Applied Probability and Random Processes (Second Edition)*, pages 369–425. Academic Press, Boston, second edi edition.

Jenkinson, M., Beckmann, C. F., Behrens, T. E., Woolrich, M. W., and Smith, S. M. (2012). FSL. *NeuroImage*, 62(2):782–790. 20 YEARS OF fMRI.

Jones, D. T., MacHulda, M. M., Vemuri, P., McDade, E. M., Zeng, G., Senjem, M. L., Gunter, J. L., Przybelski, S. A., Avula, R. T., Knopman, D. S., Boeve, B. F., Petersen, R. C., and Jack, C. R. (2011). Age-related changes in the default mode network are more advanced in Alzheimer disease. *Neurology*, 77(16):1524–1531.

Jones, D. T., Vemuri, P., Murphy, M. C., Gunter, J. L., Senjem, M. L., Machulda, M. M., Przybelski, S. A., Gregg, B. E., Kantarci, K., Knopman, D. S., Boeve, B. F., Petersen, R. C., and Jack, C. R. (2012). Non-stationarity in the "resting brain's" modular architecture. *PLoS ONE*, 7(6).

Kaku, M. (2014). *The future of the mind: the scientific quest to understand, enhance, and empower the mind*. New York : Doubleday, 1 edition.

Karvanen, J. and Theis, F. J. (2004). Spatial ICA of fMRI data in time windows. *Proc. {MaxEnt} 2004*, 735(November):312–319.

Kiviniemi, V., Vire, T., Remes, J., Elseoud, A. A., Starck, T., Tervonen, O., and Nikkinen, J. (2011). A sliding time-window ICA reveals spatial variability of the default mode network in time. *Brain Connectivity*, 1(4):339–347. PMID: 22432423.

Kucyi, A. and Davis, K. D. (2014). Dynamic functional connectivity of the default mode network tracks daydreaming. *NeuroImage*, 100:471–480.

Lee, L., Harrison, L. M., and Mechelli, A. (2003). A report of the functional connectivity workshop, Dusseldorf 2002. *NeuroImage*, 19(2):457–465.

Lee, T.-W., Girolami, M., and Sejnowski, T. J. (1999). Independent component analysis using an extended infomax algorithm for mixed subgaussian and supergaussian sources. *Neural computation*, 11(2):417–441.

Leonardi, N., Richiardi, J., Gschwind, M., Simioni, S., Annoni, J. M., Schluep, M., Vuilleumier, P., and Van De Ville, D. (2013). Principal components of functional connectivity: A new approach to study dynamic brain connectivity during rest. *NeuroImage*, 83:937–950.

Li, M., Newton, A. T., Anderson, A. W., Ding, Z., and Gore, J. C. (2019). Characterization of the hemodynamic response function in white matter tracts for event-related fMRI. *Nature Communications*, 10(1):1–11.

Li, X. and Adali, T. (2010). Blind spatiotemporal separation of second and/or higher-order correlated sources by entropy rate minimization. In *2010 IEEE International Conference on Acoustics, Speech and Signal Processing*, pages 1934–1937.

Li, Kaiming; Guo, Lei; Nie, Jingxin; Gang, Li; Liu, T. (2009). Review of methods for functional brain connectivity detection using fMRI. *Computerized Medical Imaging and Graphics*, 33(2):131–139.

Liu, X., Chen, X., Zheng, W., Xia, M., Han, Y., Song, H., Li, K., He, Y., and Wang, Z. (2018). Altered functional connectivity of insular subregions in Alzheimer's disease. *Frontiers in Aging Neuroscience*, 10:107.

Liu, Y. and Zhang, N. (2019). Propagations of spontaneous brain activity in awake rats. *NeuroImage*, 202:116176.

Ma, S., Calhoun, V. D., Phlypo, R., and Adalı, T. (2014). Dynamic changes of spatial functional network connectivity in healthy individuals and schizophrenia patients using independent vector analysis. *NeuroImage*, 90:196–206.

Mai, J. K. (2017). *Human brain in standard MNI space : structure and function : a comprehensive pocket atlas / Jürgen K. Mai, Milan Majtanik.* Academic Press, London.

Majeed, W., Magnuson, M., Hasenkamp, W., Schwarb, H., Schumacher, E. H., Barsalou, L., and Keilholz, S. D. (2011). Spatiotemporal dynamics of low frequency BOLD fluctuations in rats and humans. *NeuroImage*, 54(2):1140–1150.

Mak-Mccully, R. A., Rolland, M., Sargsyan, A., Gonzalez, C., Magnin, M., Chauvel, P., Rey, M., Bastuji, H., and Halgren, E. (2017). Coordination of cortical and thalamic activity during non-REM sleep in humans. *Nature Communications*, 8(1):1–11.

Makeig, S., Enghoff, S., ping Jung, T., and Sejnowski, T. J. (2000). Moving-window ICA decomposition of EEG data reveals event-related changes in oscillatory brain activity. In *in Proc. 2nd Int. Workshop on Independent Component Analysis and Blind Source Separation (ICA'2000*, pages 627–632.

Matsui, T., Murakami, T., and Ohki, K. (2016). Transient neuronal coactivations embedded in globally propagating waves underlie resting-state functional connectivity. *Proceedings of the National Academy of Sciences of the United States of America*, 113(23):6556–6561.

Mayer, A., Ling, J., Allen, E. A., Klimaj, S., Yeo, R., and Hanlon, F. M. (2014). Static and dynamic intrinsic connectivity following mild traumatic brain injury. *Journal of neurotrauma*, 1055:1–50.

Mijalkov, M., Volpe, G., and Pereira, J. B. (2022). Directed Brain Connectivity Identifies Widespread Functional Network Abnormalities in Parkinson's Disease. *Cerebral cortex (New York, N.Y. : 1991)*, 32(3):593–607.

Mitra, A., Kraft, A., Wright, P., Acland, B., Snyder, A. Z., Rosenthal, Z., Czerniewski, L., Bauer, A., Snyder, L., Culver, J., Lee, J. M., and Raichle, M. E. (2018). Spontaneous Infra-slow Brain Activity Has Unique Spatiotemporal Dynamics and Laminar Structure. *Neuron*, 98(2):297–305.e6.

Mitra, A. and Raichle, M. E. (2016). How networks communicate: Propagation patterns in spontaneous brain activity.

Mitra, A., Snyder, A. Z., Blazey, T., Raichle, M. E., Buzsáki, G., Sporns, O., Victor, J. D., and Yuste, R. (2015a). Lag threads organize the brain's intrinsic activity. *Proceedings of the National Academy of Sciences of the United States of America*, 112(17):E2235–E2244.

Mitra, A., Snyder, A. Z., Constantino, J. N., and Raichle, M. E. (2017). The Lag Structure of Intrinsic Activity is Focally Altered in High Functioning Adults with Autism. *Cerebral cortex (New York, N.Y. : 1991)*, 27(2):1083–1093.

Mitra, A., Snyder, A. Z., Tagliazucchi, E., Laufs, H., and Raichle, M. E. (2015b). Propagated infra-slow intrinsic brain activity reorganizes across wake and slow wave sleep. *eLife*, 4(NOVEMBER2015).

Mohd Khairi, N., Wilkes, D. M., and Ding, Z. (2019). Modified Principal Component Analysis in sliding windowed fMRI data. In *SoutheastCon 2019*.

Mokhtari, F., Akhlaghi, M. I., Simpson, S. L., Wu, G., and Laurienti, P. J. (2019). Sliding window correlation analysis: Modulating window shape for dynamic brain connectivity in resting state. *NeuroImage*, 189:655 – 666.

Muhei-aldin, O., VanSwearingen, J., Karim, H., Huppert, T., Sparto, P. J., Erickson, K. I., and Sejdić, E. (2014). An investigation of fMRI time series stationarity during motor sequence learning foot tapping tasks. *Journal of Neuroscience Methods*, 227:75–82.

Murphy, K., Birn, R. M., Handwerker, D. A., Jones, T. B., and Bandettini, P. A. (2009). The impact of global signal regression on resting state correlations: Are anti-correlated networks introduced? *NeuroImage*, 44(3):893–905.

Murphy, W., Black, J., and Hastings, G. (2016). *Handbook of Biomaterial Properties*. Springer New York.

Nalci, A., Rao, B. D., and Liu, T. T. (2017). Global signal regression acts as a temporal downweighting process in resting-state fMRI. *NeuroImage*, 152:602–618.

Newton, A. T., Morgan, V. L., and Gore, J. C. (2007). Task demand modulation of steady-state functional connectivity to primary motor cortex. *Human Brain Mapping*, 28(7):663–672.

Niazy, R. K., Xie, J., Miller, K., Beckmann, C. F., and Smith, S. M. (2011). Chapter 17 - spectral characteristics of resting state networks. In Someren, E. J. V., Werf, Y. D. V. D., Roelfsema, P. R., Mansvelder, H. D., and Silva, F. H. L. D., editors, *Slow Brain Oscillations of Sleep, Resting State and Vigilance*, volume 193 of *Progress in Brain Research*, pages 259 – 276. Elsevier.

Ogawa, S. and Lee, T. (1990). Brain magnetic resonance imaging with contrast dependent on blood oxygenation. *Proceedings of the . . .*, 87(24):9868–72.

Park, J. K., Kim, S. K., Cho, I. H., and Kong, E. J. (2014). Measurement of SUVs-maximum for normal region using voi in PET/MRI and PET/CT. *The Scientific World Journal*, 2014.

Philippi, N., Noblet, V., Hamdaoui, M., Soulier, D., Botzung, A., Ehrhard, E., Cretin, B., Blanc, F., Martin-Hunyadi, C., Demuynck, C., Anthony, P., Mutter, C., Kemp, J., Monjoint, L., Albasser, T., Rauch, S., Phillipps, C., Rauch, L., and study group, A. (2020). The insula, a grey matter of tastes: a volumetric MRI study in dementia with Lewy bodies. *Alzheimer's Research & Therapy*, 12(1):79.

Ponce-Alvarez, A., Deco, G., Hagmann, P., Romani, G. L., Mantini, D., and Corbetta, M. (2015). Resting-State Temporal Synchronization Networks Emerge from Connectivity Topology and Heterogeneity. *PLoS Computational Biology*, 11(2).

Power, J. D., Cohen, A. L., Nelson, S. M., Wig, G. S., Barnes, K. A., Church, J. A., Vogel, A. C., Laumann, T. O., Miezin, F. M., Schlaggar, B. L., and Petersen, S. E. (2011). Functional Network Organization of the Human Brain. *Neuron*, 72(4):665–678.

Rachakonda, S., Egolf, E., Correa, N., and Calhoun, V. (2007). Group ICA of fMRI toolbox (GIFT) manual. *Dostupnéz http://www.nitrc.org/docman/view.php/55/295/v1.3d_GIFTManual.pdf [cit. 2011-11-5]*.

Raut, R. V., Mitra, A., Marek, S., Ortega, M., Snyder, A. Z., Tanenbaum, A., Laumann, T. O., Dosenbach, N. U., and Raichle, M. E. (2020). Organization of Propagated Intrinsic Brain Activity in Individual Humans. *Cerebral Cortex (New York, NY)*, 30(3):1716.

Raut, R. V., Mitra, A., Snyder, A. Z., and Raichle, M. E. (2019). On time delay estimation and sampling error in resting-state fMRI. *NeuroImage*, 194:211–227.

Rogers, B. P., Morgan, V. L., Newton, A. T., and Gore, J. C. (2007). Assessing functional connectivity in the human brain by fMRI. *Magnetic resonance imaging*, 25(10):1347–57.

Rolls, E. T. (2021). Attractor cortical neurodynamics, schizophrenia, and depression. *Translational psychiatry*, 11(1).

Rolls, E. T., Cheng, W., and Feng, J. (2021). Brain dynamics: the temporal variability of connectivity, and differences in schizophrenia and ADHD. *Translational Psychiatry 2021 11:1*, 11(1):1–11.

Rolls, E. T., Huang, C.-C., Lin, C.-P., Feng, J., and Joliot, M. (2020). Automated anatomical labelling atlas 3. *NeuroImage*, 206:116189.

Rubinov, M. and Sporns, O. (2010). Complex network measures of brain connectivity: uses and interpretations. *NeuroImage*, 52(3):1059–1069.

Saad, Z. S., Gotts, S. J., Murphy, K., Chen, G., Jo, H. J., Martin, A., and Cox, R. W. (2012). Trouble at Rest: How Correlation Patterns and Group Differences Become Distorted After Global Signal Regression. *Brain Connectivity*, 2(1):25–32.

Sadeghi-Tarakameh, A., DelaBarre, L., Lagore, R. L., Torrado-Carvajal, A., Wu, X., Grant, A., Adriany, G., Metzger, G. J., Van de Moortele, P. F., Ugurbil, K., Atalar, E., and Eryaman, Y. (2020). In vivo human head MRI at 10.5T: A radiofrequency safety study and preliminary imaging results. *Magnetic Resonance in Medicine*, 84(1):484–496.

Sakoglu, U., Pearlson, G. D., Kiehl, K. A., Wang, Y. M., Michael, A. M., and Calhoun, V. D. (2010). A method for evaluating dynamic functional network connectivity and task-modulation: Application to schizophrenia. *Magnetic Resonance Materials in Physics, Biology and Medicine*, 23(5-6):351–366.

Scheef, L. and Boecker, H. (2012). *Functional and Structural MRI: Theoretical Background and Practical Aspects in Boecker H., Hillman C., Scheef L., Strüder, H. (eds) Functional Neuroimaging in Exercise and Sport Sciences*, pages 269–317. Springer New York, New York, NY.

Shakil, S., Keilholz, S. D., and Lee, C.-H. (2015). On frequency dependencies of sliding window correlation. In *Proceedings - 2015 IEEE International Conference on Bioinformatics and Biomedicine, BIBM 2015*, pages 363–368. Institute of Electrical and Electronics Engineers Inc.

Shakil, S., Lee, C.-H., and Keilholz, S. D. (2016). Evaluation of sliding window correlation performance for characterizing dynamic functional connectivity and brain states. *NeuroImage*, 133:111 – 128.

Shine, J. M., Kucyi, A., Foster, B. L., Bickel, S., Wang, D., Liu, H., Poldrack, R. A., Hsieh, L. T., Hsiang, J. C., and Parvizi, J. (2017). Distinct Patterns of Temporal and Directional Connectivity among Intrinsic Networks in the Human Brain. *Journal of Neuroscience*, 37(40):9667–9674.

Smith, S. M., Miller, K. L., Moeller, S., Xu, J., Auerbach, E. J., Woolrich, M. W., Beckmann, C. F., Jenkinson, M., Andersson, J. L. R., Glasser, M. F., Van Essen, D. C., Feinberg, D. A., Yacoub, E. S., and Ugurbil, K. (2012). Temporally-independent functional modes of spontaneous brain activity. *Proceedings of the National Academy of Sciences of the United States of America*, 109(8):3131–6.

Soldati, N., Calhoun, V. D., Bruzzone, L., and Jovicich, J. (2013). ICA analysis of fMRI with real-time constraints: an evaluation of fast detection performance as function of algorithms, parameters and a priori conditions. *Frontiers in human neuroscience*, 7(February):19.

Staff, B. (2014). Medical gallery of Blausen Medical 2014. *WikiJournal of Medicine*, 1(2).

Tae, W. S., Yakunina, N., Kim, T. S., Kim, S. S., and Nam, E. C. (2014). Activation of auditory white matter tracts as revealed by functional magnetic resonance imaging. *Neuroradiology*, 56(7):597–605.

Tagliazucchi, E., Balenzuela, P., Fraiman, D., and Chialvo, D. (2012a). Criticality in large-scale brain fmri dynamics unveiled by a novel point process analysis. *Frontiers in Physiology*, 3:15.

Tagliazucchi, E., Balenzuela, P., Fraiman, D., and Chialvo, D. (2012b). Criticality in large-scale brain fMRI dynamics unveiled by a novel point process analysis. *Frontiers in Physiology*, 3:15.

Tagliazucchi, E., Siniatchkin, M., Laufs, H., and Chialvo, D. R. (2016). The Voxel-Wise Functional Connectome Can Be Efficiently Derived from Co-activations in a Sparse Spatio-Temporal Point-Process. *Frontiers in Neuroscience*, 10:381.

Takeda, Y., Hiroe, N., and Yamashita, O. (2021). Whole-brain propagating patterns in human resting-state brain activities. *NeuroImage*, 245:118711.

Veit, M. J., Kucyi, A., Hu, W., Zhang, C., Zhao, B., Guo, Z., Yang, B., Sava-Segal, C., Perry, C., Zhang, J., Zhang, K., and Parvizi, J. (2021). Temporal order of signal propagation within and across intrinsic brain networks. *Proceedings of the National Academy of Sciences of the United States of America*, 118(48).

Vergun, S., Gaggl, W., Nair, V. A., Suhonen, J. I., Birn, R. M., Ahmed, A. S., Meyerand, M. E., Reuss, J., DeYoe, E. A., and Prabhakaran, V. (2016). Classification and extraction of resting state networks using healthy and epilepsy fMRI data. *Frontiers in neuroscience*, 10:440.

Viviani, R., Grön, G., and Spitzer, M. (2005). Functional principal component analysis of fMRI data. *Human brain mapping*, 24(2):109–29.

Wang, X., Seguin, C., Zalesky, A., Wong, W. W., Chu, W. C. W., and Tong, R. K. Y. (2019). Synchronization lag in post stroke: Relation to motor function and structural connectivity. *Network Neuroscience*, 3(4):1121–1140.

Wang, Y., Sun, K., Yuan, X., Cao, Y., Li, L., and Koivo, H. N. (2018). A Novel Sliding Window PCA-IPF Based Steady-State Detection Framework and Its Industrial Application. *IEEE Access*, 6:20995–21004.

Weiskopf, N., Sitaram, R., Josephs, O., Veit, R., Scharnowski, F., Goebel, R., Birbaumer, N., Deichmann, R., and Mathiak, K. (2007). Real-time functional magnetic resonance imaging: methods and applications. *Magnetic Resonance Imaging*, 25(6):989–1003.

Wold, S., Esbensen, K., and Geladi, P. (1987). Principal component analysis. *Chemometrics and Intelligent Laboratory Systems*, 2(1-3):37–52.

Wu, X., Yang, Z., Bailey, S. K., Zhou, J., Cutting, L. E., Gore, J. C., and Ding, Z. (2017). Functional connectivity and activity of white matter in somatosensory pathways under tactile stimulations. *NeuroImage*, 152:371–380.

Wu, X., Yu, X., Yao, L., and Li, R. (2014). Bayesian network analysis revealed the connectivity difference of the default mode network from the resting-state to task-state. *Frontiers in Computational Neuroscience*, 8:118.

Yacoub, E., Grier, M. D., Auerbach, E. J., Lagore, R. L., Harel, N., Adriany, G., Zilverstand, A., Hayden, B. Y., Heilbronner, S. R., Uğurbil, K., and Zimmermann, J. (2020). Ultra-high field (10.5 T) resting state fMRI in the macaque. *NeuroImage*, 223:117349.

Yeo, B., Krienen, F., Sepulcre, J., Sabuncu, M., Lashkari, D., Hollinshead, M., et al. (2011). 1031 the organization of the human cerebral cortex estimated by intrinsic functional connectivity. *Journal of*, 1032:1125–1165.

Zhan, X. and Yu, R. (2015). A window into the brain: Advances in psychiatric fMRI. In *BioMed research international*.

Zhou, Y., Yu, F., and Duong, T. (2014). Multiparametric MRI characterization and prediction in autism spectrum disorder using graph theory and machine learning. *PloS one*, 9(6):e90405.

Zilverstand, A., Sorger, B., Zimmermann, J., Kaas, A., and Goebel, R. (2014). Windowed correlation: A suitable tool for providing dynamic fMRI-based functional connectivity neurofeedback on task difficulty. *PLoS ONE*, 9(1):e85929.